

Sparse chaos in cortical circuits

Rainer Engelken^{1,2,3,4,*}, Michael Monteforte⁴, and Fred Wolf^{3,4,5,6,7}

Department of Neuroscience, Zuckerman Institute,

Columbia University, New York, NY, United States of America¹,

Kavli Institute of Brain Science, Columbia University, New York, NY, United States of America²,

Göttingen Campus Institute for Dynamics of Biological Networks, Göttingen, Germany³,

Max Planck Institute for Dynamics and Self-Organization, Göttingen, Germany⁴,

Faculty of Physics, Georg-August-Universität Göttingen, Göttingen, Germany⁵,

Cluster of Excellence "Multiscale Bioimaging: from Molecular Machines to Networks

of Excitable Cells" (MBExC), University of Göttingen, Göttingen, Germany⁶,

Bernstein Center for Computational Neuroscience, Göttingen, Germany⁷

Nerve impulses, the currency of information flow in the brain, are generated by an instability of the neuronal membrane potential dynamics. Neuronal circuits exhibit collective chaos that appears essential for learning, memory, sensory processing, and motor control. However, the factors controlling the nature and intensity of collective chaos in neuronal circuits are not well understood. Here we use computational ergodic theory to demonstrate that basic features of nerve impulse generation profoundly affect collective chaos in neuronal circuits. Numerically exact calculations of Lyapunov spectra, Kolmogorov-Sinai-entropy, and upper and lower bounds on attractor dimension show that changes in nerve impulse generation in individual neurons moderately impact information encoding rates but qualitatively transform phase space structure. Specifically, we find a drastic reduction in the number of unstable manifolds, Kolmogorov-Sinai entropy, and attractor dimension. Beyond a critical point, marked by the simultaneous breakdown of the diffusion approximation, a peak in the largest Lyapunov exponent, and a localization transition of the leading covariant Lyapunov vector, networks exhibit *sparse chaos*: prolonged periods of near stable dynamics interrupted by short bursts of intense chaos. Analysis of large, more realistically structured networks supports the generality of these findings. In cortical circuits, biophysical properties appear tuned to this regime of *sparse chaos*. Our results reveal a close link between fundamental aspects of single-neuron biophysics and the collective dynamics of cortical circuits, suggesting that nerve impulse generation mechanisms are adapted to enhance circuit controllability and information flow.

Information is processed in the brain by the spatiotemporal activity of large spiking neural circuits. Only the information that is encoded in spike trains can be utilized by local networks, subsequent processing stages, and ultimately to guide behavior. The spiking output of a cortical neuron contains twenty- to hundred-fold less information about synaptic input than its membrane potential does [1], making spike initiation a critical bottleneck for neural information transmission. Experiments have revealed that neocortical neurons possess a surprisingly broad encoding bandwidth, reliably encoding high-frequency stimulus components in outgoing spike trains [2, 46–48]. As predicted theoretically and observed experimentally, small changes in spike onset rapidness can have a great impact on information encoding bandwidth in feedforward architectures [6, 7, 10, 11, 18, 19, 48]. Here, spike onset rapidness refers to the steepness of the membrane potential change at the initiation of an action potential [19]. However, the influence of spike onset rapidness on recurrent network dynamics has not been systematically studied.

One might expect that collective dynamics are insensitive to cellular details, as the effect of single-cell properties can often become negligible at the macroscopic circuit level. For example, asynchronous irregular activity in idealized cortex models emerges robustly in inhibition-dominated circuits and can be described by mean-field

theory, which is largely independent of the neuron model, such as the specific spike initiation mechanism [1, 6]. Instead, collective dynamics are expected to be primarily shaped by the wiring diagram, or connectome, with most biological and artificial learning algorithms operating at this level [14, 15]. Rate networks provide an example in which single-element input-output functions determine critical properties of collective dynamics [16]. These analytical approaches have recently been extended to heterogeneous networks, networks with bistable units, and spiking networks with slow synaptic dynamics [17, 18].

Here, we show that, surprisingly, spike onset rapidness fundamentally reshapes the nature of chaos in large-scale spiking networks, such as the canonical balanced network model where excitatory currents are dynamically balanced by fast and strong recurrent inhibition [1, 6]. Leveraging concepts from ergodic theory, we demonstrate that increasing the onset rapidness drives a transition from a *dense* chaotic state—where chaotic fluctuations are continuously fueled by many neurons—to a *sparse* chaos regime characterized by intermittent, highly localized instability events. At the heart of this transition is the breakdown of the diffusion approximation, a standard assumption that treats synaptic input as Gaussian-like noise (see Supplementary Information for details). In the high-rapidness regime, shot noise effects dominate, invalidating diffusion-based descriptions and revealing a

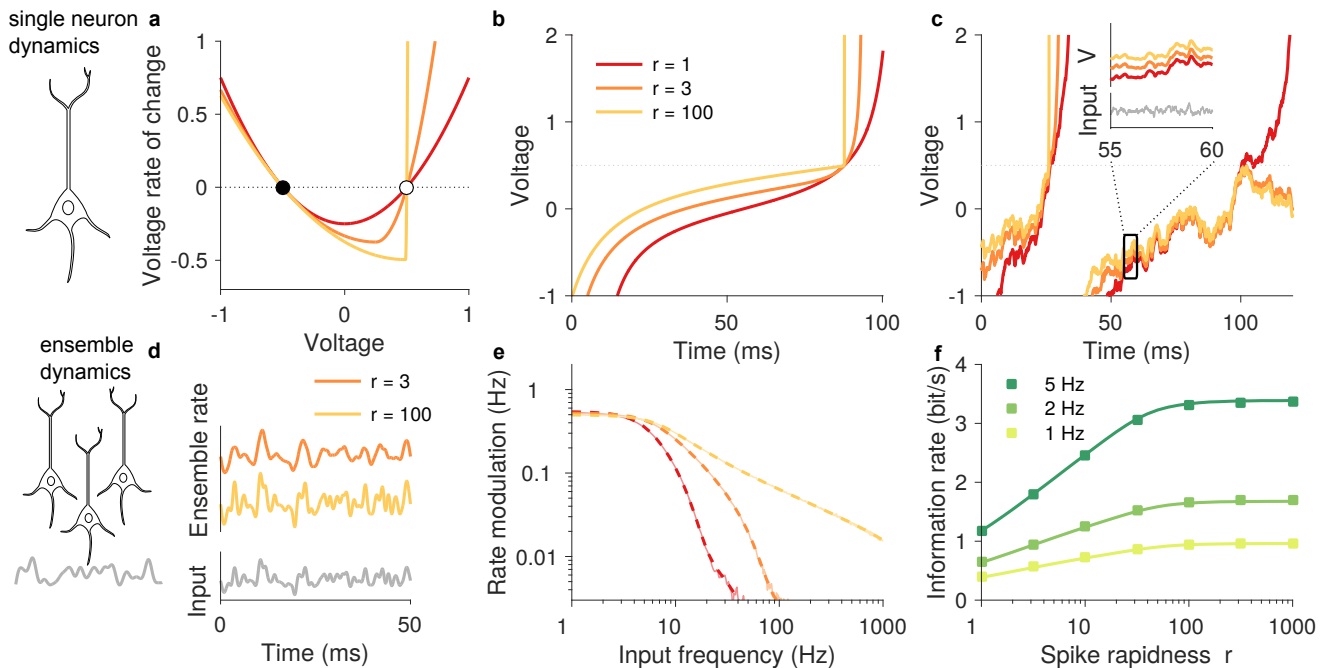


Figure 1. High spike onset rapidness r increases population encoding bandwidth. **a** Single neuron dynamics have two fixed points: a stable fixed point (filled circle, resting potential) and an unstable fixed point (white circle, spike threshold). The slope at resting potential is $-1/\tau_m$, and the slope at the spike threshold r/τ_m . **b** Voltage traces of the neuron model with constant input currents for varying rapidness r . **c** Same as in panel b, but with fluctuating input currents. Note that the spike waveform and initiation depend strongly on r , while the subthreshold dynamics are insensitive to r . The inset shows a magnified window of the voltage traces and the corresponding fluctuating input (gray). **d** Firing rates of an ensemble of rapid theta neurons with low and high rapidness for fluctuating input currents. Note that high rapidness enables the ensemble to accurately track the high-frequency components of the input. **e** Linear firing rate response for different values of rapidness, with direct numerical simulations (shaded lines) and Fokker Planck solutions (dashed lines) superimposed. ($\nu_0 = 1$ Hz). **f** Mutual information rate in the Gaussian channel approximation based on spectral coherence, comparing Fokker Planck solutions (solid lines) and direct numerical simulations (squares) for different mean ensemble firing rates ($\nu_0 = 1, 2, 5$ Hz) (parameters: $\tau_m = 10$ ms).

new dynamical regime. This transition, which occurs at a critical rapidness $r_{breakdown}$ that we first analyze in a feedforward setting, is driven by two opposing effects of spike onset rapidness. While faster onset increases single-neuron instability, it also reduces the time window during which a neuron is highly sensitive to input. Like a camera shutter that's open for a fraction of a second, the neuron only captures a few 'photons' of synaptic input during this window of instability. In this regime, the discrete nature of these inputs (shot noise) becomes prominent, and the central limit theorem underlying the diffusion approximation no longer applies, invalidating the diffusion approximation. As rapidness increases, the latter effect surprisingly dominates, shifting the network from *dense* to *sparse chaos*. These findings establish a direct link between single-neuron spike initiation properties and the global chaotic dynamics of recurrent circuits. Beyond clarifying the fundamental biophysical origins of cortical chaos, our results suggest that neurons' spike onset rapidness may be tuned to operate in this regime. Such tuning could enhance the controllability of network states and optimize information transmission across cortical layers, revealing a mechanism by which biophysical details shape large-scale brain function.

In the following, we will first introduce a novel, analytically solvable neuron model with an adjustable spike onset rapidness. We will then investigate how rapidness affects information transmission in a feedforward setting, identifying a critical rapidness value, $r_{breakdown}$, where the diffusion approximation breaks down. Subsequently, we will analyze the full Lyapunov spectrum of recurrent networks of these neurons to characterize their dynamical stability and attractor properties. We will show that increasing rapidness leads to a transition from dense to sparse chaos and significantly reduces the attractor dimension. Finally, we will demonstrate that these findings are robust in more realistic cortical circuit models.

Neuron model with tunable spike onset

To study the impact of spike onset rapidness on the collective network dynamics, we constructed a novel, analytically solvable neuron model with an adjustable spike onset rapidness r , as shown in Figure 1a (see Methods for equations). The model, which we call the rapid theta model, is a modification of the theta neuron [12, 38, 39], a canonical model of neuronal excitability, and allows us to tune the rapidness of spike initiation while keeping other properties, such as the resting potential and subthreshold

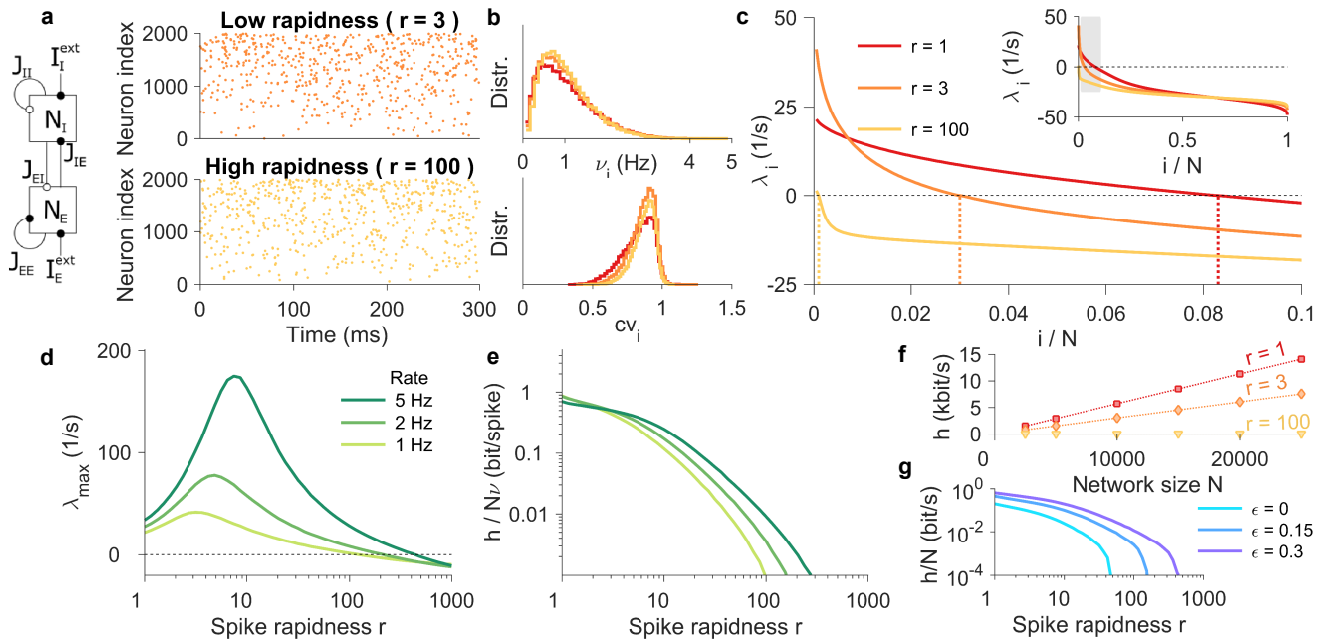


Figure 2. **High spike onset rapidness spike r dramatically reduces chaos and dynamical entropy rate.** **a** Spike trains of 50 random neurons for low (upper panel) and high (lower panel) rapidness. **b** Distribution of firing rates (upper panel) and coefficients of variation (lower panel) for different values of rapidness (ordered by time-averaged single neuron firing rate) **c** Lyapunov spectra reorganize with increasing rapidness (inset: full Lyapunov spectra) **d** Largest Lyapunov exponent and **e** entropy rate h as a function of rapidness for different mean firing rates ($\bar{\nu} = 1, 2, 5$ Hz), **f** Entropy rate h for different network sizes (upper panel) and **g** different strengths of the scaling ϵ of the excitatory couplings (parameters: $N_I = 2000$, $N_E = 8000$, $K = 100$, $\bar{\nu} = 1$ Hz, $J_0 = 1$, $\tau_m = 10$ ms).

dynamics, largely unchanged. The model’s membrane potential dynamics exhibit two fixed points: a stable fixed point representing the resting potential and an unstable fixed point corresponding to the spike threshold. The slope of the membrane potential dynamics, while at the spike threshold, it is r/τ_m . Increasing r decreases the time constant at the unstable fixed point V_U , resulting in greater instability and sharper spike initiation (Fig. 1b,c). Thus, neurons with high r spend less time in the upswing towards an action potential but are more susceptible to input. Unlike many neuron models, including the exponential integrate-and-fire model [6], our model can be solved exactly between spikes—a crucial prerequisite for precise and efficient calculation of the Lyapunov spectrum, which quantifies the sensitivity of the system to initial conditions.

Rapid Spikes Enhance Information Transmission

Before investigating the effects of spike onset rapidness in recurrent networks, we first examined its impact on information transmission in a feedforward setting. This allows us to isolate the effects of rapidness on single-neuron encoding from the complexities of recurrent dynamics. As illustrated in Figures 1d and e, high rapidness enables neurons to transmit high-frequency components of a time-varying input current in their ensemble-averaged firing rate, whereas low rapidness limits transmission to low and mid-range frequencies. These results are con-

sistent with previous studies [6, 7, 10, 11, 18, 19, 48], which have established that rapidness is a determining factor in a neuron’s ability to transmit information about presynaptic signals embedded in noise. We quantified the information transmission using the Gaussian channel approximation of the mutual information based on the spectral coherence between the input and output signals (see Supplementary Information). We found that the mutual information rate grows approximately logarithmically with rapidness (Fig. 1f and Supplementary Information for analytical results). This logarithmic relationship arises because rapidness determines the cutoff frequency beyond which spectral coherence scales as f^{-1} .

Diffusion Approximation fails for Rapid Spike Onset

Importantly, at high rapidness, we observed qualitative deviations from the predictions of the commonly used diffusion approximation. The diffusion approximation assumes that a high rate of weak synaptic input can be treated as Gaussian white noise. However, we observe a qualitative change in the high-frequency response when rapidness exceeds $r_{\text{breakdown}} \propto \sqrt{K\nu_0\tau_m/J_0}$, which indicates a breakdown of the diffusion approximation, different from previously observed shot noise effects [15, 95, 97] (see Supplementary Information for analytical derivation). This breakdown is associated with a qualitatively different dynamical regime of the network dynamics, as

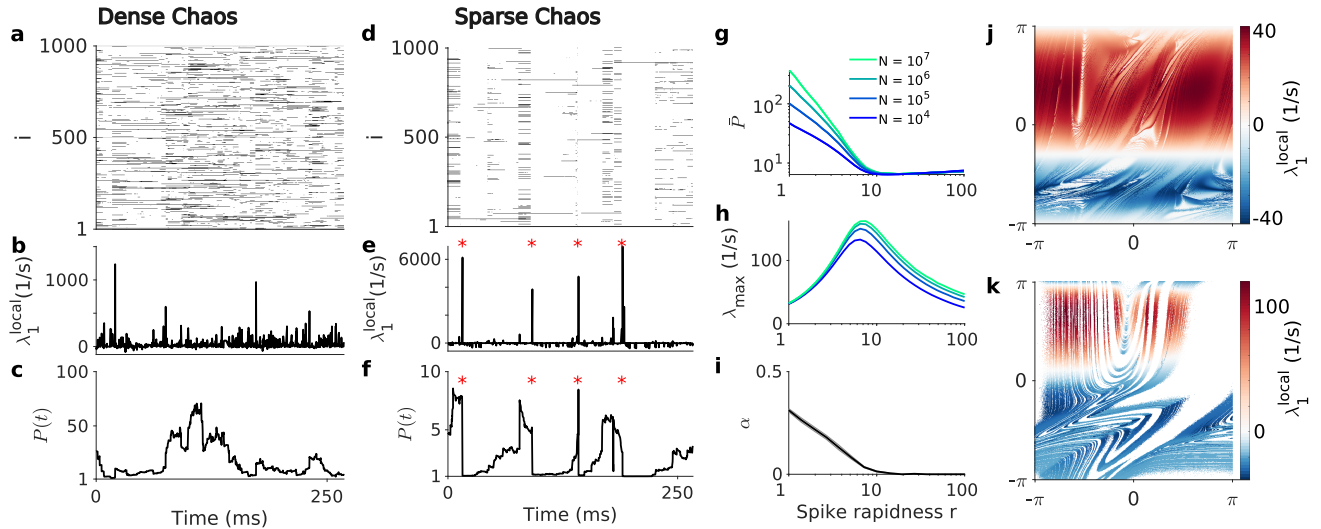


Figure 3. **Localization of Lyapunov vectors for high spike onset rapidness r reveals two types of network chaos.** **a** First Lyapunov vector (marked black if $|\delta\phi_i(t)| > 1/\sqrt{N}$) **b** First local Lyapunov exponent $\lambda_1^{\text{local}}(t)$ and **c** participation ratio $P(t)$ of the first Lyapunov vector as a function of time for $r \approx 1.33$. **d**, **e**, **f** Same as **a**, **b**, **c** for $r \approx 31.6$. Note that large local Lyapunov exponents are followed by low participation ratio (red stars). **g** Average participation ratio \bar{P} and **h** largest Lyapunov exponent vs. spike rapidness r for different network size N , **i** Power-law scaling exponent α from $\bar{P} \sim N^\alpha$ decreases approximately logarithmically as a function of r and shows localization above peak rapidness r_{peak} . **j** Poincaré section of the phases of neurons 2 and 3 whenever neuron 1 spikes for $r = 1$. The first local Lyapunov exponent (LLE) at each point is color-coded, red colors indicate local instability, blue indicates local stability **k** same as **j** for $r = 4$ (parameters: $N_I = 1000$, $K = 100$, $\bar{\nu} = 3$ Hz, $J_0 = 1$, $\tau_m = 10$ ms).

we will discuss in subsequent sections.

Unlike many neuron models, including the exponential integrate-and-fire model [16, 50], our model can be solved exactly between spikes—a crucial prerequisite for precise and efficient calculation of the Lyapunov spectrum. To analyze the impact of spike initiation on dynamical stability, we calculate the full Lyapunov spectrum of a spiking network of rapid theta neurons. Lyapunov exponents measure the rate of exponential divergence and convergence of nearby trajectories. The Lyapunov spectrum provides a good estimate of the attractor dimension, according to the Kaplan-Yorke conjecture, including exact upper and lower bounds [23–25]. In an N -dimensional dissipative chaotic system, trajectories do not cover the entire phase space. Instead, after a transient period, they relax onto a strange attractor, which has a dimensionality $D \leq N$. The Kaplan Yorke attractor dimension is given by the number of Lyapunov exponents whose cumulative sum interpolates to zero. One can think of it as the largest-dimensional infinitesimal hypersphere, whose volume does not shrink by the dissipative system dynamics. A lower bound on the attractor dimension is given by the number of positive Lyapunov exponents. The dynamical entropy rate, another canonical measure in dynamical systems, is bounded above by the sum of positive Lyapunov exponents. This bound is exact for smooth densities of the physical measure along unstable directions, as given by Pesin’s identity [26]. We analytically calculate the Jacobian of the flow, which determines how infinitesimal perturbations of the network

state evolve from one spike time to just after the next. We evaluate these Jacobians in numerically exact, event-based simulations. The product of the Jacobians gives the long-term Jacobian, which yields the spectrum of all Lyapunov exponents based on Oseledets’ multiplicative ergodic theorem [4].

Impact on Dynamical Entropy Rate

We find that rapidness strongly influences the dynamical stability of recurrent networks in the balanced state (Fig. 2). We first discuss results from inhibitory random (Erdős–Rényi) networks, followed by mixed excitatory-inhibitory random networks and more structured network topologies. One might expect that increasing rapidness r would intensify the collective chaos since individual neurons become more unstable. This is indeed the case for low rapidness: We find that the largest Lyapunov exponent grows approximately linearly with rapidness (Fig. 2d) until reaching a peak value. However, for high rapidness, the largest Lyapunov exponent decreases proportionally to $1/r$ (Fig. 2d). Numerical simulations reveal that the peak rapidness scales as $r_{\text{peak}} \propto \sqrt{K\nu_0\tau_m/J_0}$. Above this peak, we observe a localization of the first covariant Lyapunov vector (Fig. 3), which follows the same scaling as the peak rapidness r_{peak} (Supplementary Section XI). At lower values of rapidness r , the largest Lyapunov exponent remains independent of the connectivity K . Furthermore, an analytical calculation reveals that the breakdown of the diffusion approximation follows the same scaling as the peak rapidness

r_{peak} . This alignment suggests a deep connection between the breakdown of the diffusion approximation, the peak in the largest Lyapunov exponent, and the localization of the first covariant Lyapunov vector. At a critical rapidness that scales with $r_{\text{crit}} \propto N^{0.5} K^{0.5} \bar{\nu}^{0.8} \tau_m^{0.8} J_0^{-0.7}$, the largest Lyapunov exponent reaches zero, and the network activity becomes dynamically stable. However, for any finite network size N , the largest Lyapunov exponent can be reduced arbitrarily by choosing a sufficiently large r (Supplementary Section X). The dynamical entropy rate decreases monotonically with rapidness, reaching zero at r_{crit} (Fig. 2e). The full spectrum reveals that the monotonic reduction is due to a drastic reduction in the number of positive Lyapunov exponents, which overcompensates the increase of the first few Lyapunov exponents (Fig. 2c). Despite such a drastic change in the collective dynamics, the statistics of the spike trains remain essentially unaffected (Fig. 2a, b). This is surprising since, in many other systems, a transition from chaos to stability is strongly reflected in the autocorrelations and pairwise cross-correlations of the activity [16].

The scaling of the entropy rate with network size N reveals that the network chaos is extensive: for sufficiently large N , the entropy rate grows linearly with N (Fig. 2f). Convergence of the Lyapunov spectra is demonstrated in Supplementary Section VIII. Using random matrix theory, we calculate the mean Lyapunov exponent analytically (see Supplementary Section IX).

The transition from chaos to stability with increasing rapidness also occurs for random networks with both excitatory and inhibitory coupling. To isolate the effect of excitation, we parameterized the coupling matrix such that the input variance to each population remains unchanged for different scaling values ϵ of the excitatory couplings (see Supplementary Information for the definition of ϵ .) As the scaling ϵ of the excitatory couplings increases, the dynamical entropy rate also increases. If the excitation is strong enough, r_{crit} diverges, and these networks remain chaotic for any r .

Interestingly, while the dynamical stability changes drastically for different values of r , the spike train statistics remain almost unchanged. Both the distribution of firing rates and the coefficients of variation are insensitive to changes in r (Fig. 2b). The mean pairwise Pearson correlation $\bar{\rho}$ of the spike counts is weak and approaches zero for large networks, scaling as $\bar{\rho} \propto 1/N$, while the standard deviation $\bar{\sigma}$ of the pairwise correlations decreases as $\bar{\sigma} \propto 1/\sqrt{N}$ (Fig. 4e, f, g). This confirms theoretical predictions of broadly distributed, but weak pairwise correlations in the balanced state [6].

Transition from *Dense* to *Sparse Chaos* with Increasing Spike Onset Rapidness

To further characterize the effect of spike-onset rapidness r on network dynamics, we compare two networks with different values of rapidness but similar largest Lyapunov

exponent: one at low rapidness ($r = 1.33$) representing *dense chaos*, and one at high rapidness ($r = 31.6$) representing *sparse chaos* (Fig. 3).

At higher values of spike onset rapidness r , we observe a transition in the nature of chaos within the network, revealing two distinct regimes: *dense chaos* and *sparse chaos*, characterized by a peak in the largest Lyapunov exponent and the localization of the first covariant Lyapunov vector (Fig. 3). In the *dense chaos regime* at low rapidness (Fig. 3a-c), neurons launch into action potentials gradually and spend a considerable time in the unstable voltage range. This extended duration increases the probability that postsynaptic neurons are in the unstable voltage range when they receive input spikes, leading to an increased probability of postsynaptic neurons contributing to the chaotic dynamics at any given moment. The participation ratio $P(t)$, which quantifies the number of neurons actively contributing to the first Lyapunov vector, increases with network size N in the *dense chaos* regime (Fig. 3g). The first local Lyapunov exponent $\lambda_1^{\text{local}}(t)$ exhibits temporal fluctuations with frequent small, positive peaks (Fig. 3b), reflecting that instability is widespread across the network and frequent in time.

As r increases, neurons initiate action potentials more rapidly, spending less time in the unstable voltage range. This reduction leads to fewer synaptic inputs during the critical upswing phase. Therefore, the central limit theorem underlying the diffusion approximation no longer applies, resulting in the breakdown of the diffusion approximation. This breakdown coincides with the peak of the largest Lyapunov exponent at r_{peak} (Fig. 3h) and triggers the localization of the first covariant Lyapunov vector, marking the transition from *dense* to *sparse chaos* (Fig. 3d-f). In the *sparse chaos* regime, the time a neuron spends in the unstable upswing toward the action potential becomes so brief that it is unlikely for a postsynaptic neuron to receive an input spike during this period. Consequently, the chaotic dynamics become *sparse* both temporally and across the neuronal population: instability occurs infrequently and is concentrated in brief events when a neuron in the upstroke phase receives an input spike. During these instability events, the local Lyapunov exponent $\lambda_1^{\text{local}}(t)$ exhibits large peaks (Fig. 3e), and the participation ratio $P(t)$ drops sharply, approaching values close to 1 (Fig. 3f). This indicates that only a few neurons dominate the tangent space dynamics during those moments. The average participation ratio \bar{P} becomes independent of network size N in the *sparse chaos* regime, providing clear evidence of the localization of the first covariant Lyapunov vector (Fig. 3g). This qualitative change in network dynamics occurs concurrently with the peak of the largest Lyapunov exponent and the breakdown of the diffusion approximation at high r . As neurons spend less time in the unstable voltage range, the average number of synaptic inputs received during

the critical upswing phase decreases. When this number becomes very low, individual synaptic events (shot noise) become significant, and the central limit theorem underlying the diffusion approximation no longer applies. Analytical calculations of the frequency response reveal a different frequency response at large r , confirming the breakdown of the diffusion approximation (see Supplementary Information).

Interestingly, the rapidness r at which this breakdown occurs scales similarly to r_{peak} , suggesting a deeper connection between the localization of the Lyapunov vector, the peak in the largest Lyapunov exponent, and the breakdown of the diffusion approximation.

A visualization of the local Lyapunov exponents further illustrates the effect of increasing rapidness r . At low r , a larger portion of the Poincaré section displays slightly unstable dynamics, indicating that instability is broadly distributed across the phase space (Fig. 3j). In contrast, at high r , the unstable regions of the Poincaré section become smaller but exhibit much higher local instability, as quantified by the local Lyapunov exponent (Fig. 3k). This indicates that instability is concentrated in specific regions of the neural state space at high r .

In summary, increasing the spike onset rapidness r beyond r_{peak} leads to a transition from *dense* to *sparse chaos*, coinciding with the breakdown of the diffusion approximation. This transition is marked by the peak in the largest Lyapunov exponent and the localization of the first covariant Lyapunov vector, highlighting the profound impact of single-neuron properties on collective network dynamics.

Attractor dimensionality

How is the drastic change in collective dynamics reflected in the attractor dimension and the structure of pairwise correlations? We find that increasing spike onset rapidness reduces the attractor dimension, including both its upper and lower bounds by orders of magnitude (Fig. 4a). We find that this reduction is independent of network size and also occurs in mixed excitatory-inhibitory networks (Fig. 4b, c). The dimensionality of neural activity is often measured by the number of principal components required to explain a fixed fraction of the variance [28–31]. In this case, a dimensionality estimate based on pairwise statistics vastly overestimates the attractor dimension (dotted lines in 4a and c). This implies that network dynamics exhibit strongly ‘entangled’ statistics, which are obscured when inspecting only pairwise correlations (Fig. 4e, f, g). Thus, the twisted, low-dimensional strange attractor is interlaced in a high-dimensional phase space [32]. In the extreme case of very high rapidness beyond the critical rapidness r_{crit} the network dynamics become stable, and the basins of attraction can be visualized by random cross sections of the phase space along two random N -dimensional vectors (Fig. 3d, h). Adjacent initial conditions that converge to

the same trajectory are assigned the same color. As r approaches r_{crit} from above, the basins of attraction become smaller and more curved, and at r_{crit} they vanish (see Supplementary Information).

Cortical circuit models

In the previous sections, we studied the dynamics of random (Erdős–Rényi) balanced networks, which serve as canonical, idealized models of neocortical networks. Since cortical tissue has a distinct architecture with a non-random microscopic motif structure and a layered organization where each layer has different wiring probabilities and distinct thalamic inputs, we next investigate whether the previous findings are robust under a more realistic microscopic and macroscopic structure. To analyze the effect of a multilayered topology, we took experimental data of wiring probability and synapse count from [7] to build a full cortical column with 77,169 neurons, approximately 285 million synapses, and four layers, each containing excitatory and inhibitory neuron populations. This model produced spiking dynamics with layer-specific firing rates (Fig. 5a, b). We calculated Lyapunov spectra in large, more realistic networks using an efficient, massively parallelized implementation (Fig. 5e). We also constructed large mixed excitatory-inhibitory circuits that incorporate experimentally measured motif frequencies (Fig. 5f) [8].

In these more realistic network structures, our findings from idealized random cortex models were confirmed (Fig. 5). In the multilayered network, the largest Lyapunov exponent behaves similarly to that in the random network. It initially increases with rapidness before decreasing (Fig. 5c). The entropy rate declines as rapidness increases (Fig. 5d). When comparing a random topology to a network with experimentally measured motif frequencies, we observe a similarly strong reduction in dynamical entropy rate with increasing spike onset rapidness (Fig. 5g). Thus, the drastic reduction in chaos and dynamical entropy rate due to high spike onset rapidness is independent of network structure. This finding justifies analyzing more idealized random networks.

Conclusion and summary

Recent theoretical and experimental studies have shown that cortical neurons possess a surprisingly broad encoding bandwidth, which depends on details of the spike initiation mechanism. Here, we investigated the effect of this on the collective recurrent dynamics of neocortical spiking circuits. We found that canonical measures of the collective dynamics are not universal and insensitive to single-cell properties; rather, they show a strong dependence on spike onset rapidness. Here, we show that increasing spike onset rapidness transforms the network’s chaos from a *dense* regime, in which instability is continuously fueled by many neurons, to a *sparse* regime, characterized by sporadic, sharply localized instability events. This transition defies the intuitive expectation

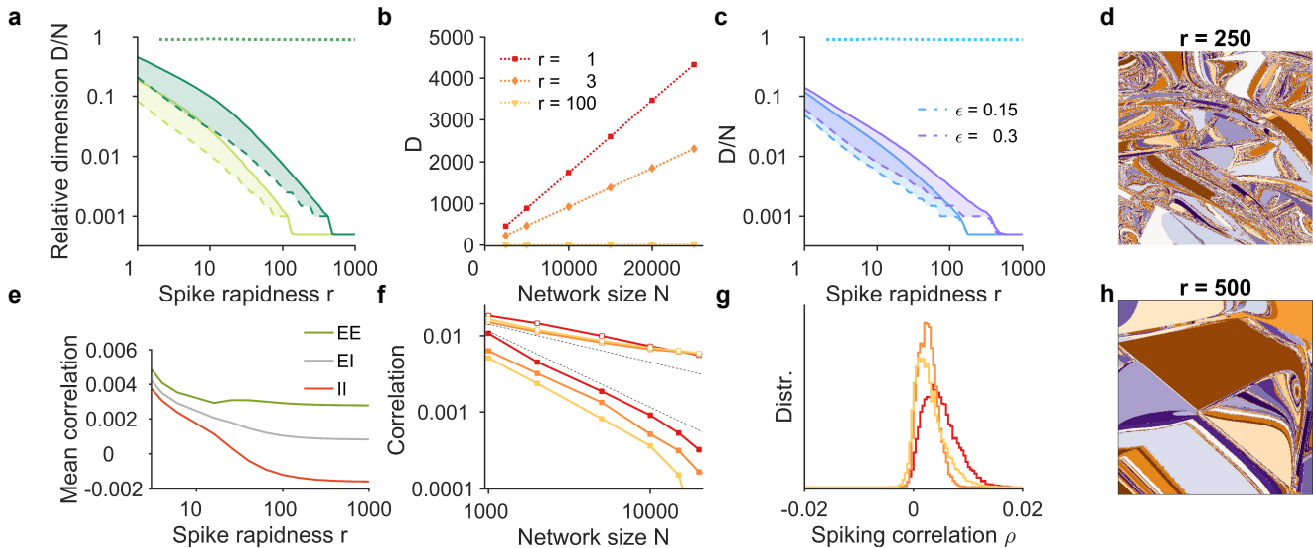


Figure 4. **Reduction of attractor dimensionality in the asynchronous state despite low pairwise spike count correlations.** **a** Attractor dimension for different mean firing rates and varying spike rapidness r , dotted line: dimensionality estimate based on principal components of pairwise spike count correlations matrix (Supplementary Information), solid line: Kaplan-Yorke (KY) attractor dimension, dashed line: lower bound on attractor dimension (fraction of positive exponents) **b** KY Attractor dimension grows linearly with network size N **c** same as **a** for different scaling ϵ of the excitatory couplings **d, h** cross sections of basis on attraction in a plane perpendicular to the trajectory for $r = 250, 500$. Colors indicate basins of attraction of different trajectories ($N = 200, K = 100, r_c \approx 203$) **e** Mean pairwise spike count correlations for different values of rapidness r between excitatory (E) and inhibitory (I) neurons, excitatory-excitatory pairs (EE) in green, inhibitory-inhibitory pairs (II) in red, mixed pairs in yellow **f** Mean pairwise spike count correlations decay $\propto 1/N$, their standard deviations decays $\propto 1/\sqrt{N}$, (color code as in **b**) **g** histograms of spike count correlations for different rapidness r (EE-pairs)(color code as in **b**)(parameters as in Fig. 2, spike count window 20 ms)

that higher single-cell instability would simply amplify chaos. Instead, it reduces the overall chaotic intensity and complexity of the collective state. This also holds in more realistic network structures, including multilayered and second-order motif networks. The effect of spike onset on chaotic entropy rate is orders of magnitude greater than its effect on information encoding bandwidth. The importance of single cell dynamics limiting the encoding bandwidth in a feedforward architecture is thus not washed out by the collective network dynamics.

The dimensionality of collective states in neural circuits is a fundamental measure. Different dimensionality metrics may be necessary to characterize the complex dynamics. Using concepts from ergodic theory, we show that attractor dimension decreases drastically with increasing spike onset rapidness, a change hidden from conventional dimensionality estimates based on activity correlations. This implies that neuron states have strong statistical dependencies. How such dependencies might be leveraged for computations in neocortical circuits is a question for future research.

Since the spike threshold acts as an unstable fixed point for single-cell dynamics, one might expect that high single-cell instability (i.e., high spike onset rapidness r) would increase network chaos. Surprisingly, we find the opposite: large single-cell instability stabilizes collective dynamics. Chaotic dynamics may be useful in computa-

tion for amplifying small differences in initial conditions. If such a mechanism is used by cortical circuits, spike onset rapidness would be an important parameter to regulate this. Certainly, the dynamical entropy rate contributes to noise entropy and can therefore impair coding capacity.

The cortex relies on intricate communication between layered circuits. Given that controlling highly chaotic networks with spike trains is likely difficult, we conjecture that high spike onset rapidness facilitates state control and thus enhances information transmission between circuits.

The ability of one circuit's spike train to control dynamics in subsequent circuit is key for encoding information. Controlling highly chaotic networks with input spike trains is presumably more challenging. We therefore conjecture that high spike onset rapidness facilitates network state control and enhances information transmission.

The use of ergodic theory to understand neural computation is only just beginning. By applying these concepts to large-scale neural circuits, we have laid the foundations for further investigation. Until now, computational ergodic theory of spiking networks has been the only approach to measure information-theoretic quantities in large recurrent circuits. An important challenge is to extend this approach to other quantities, such as

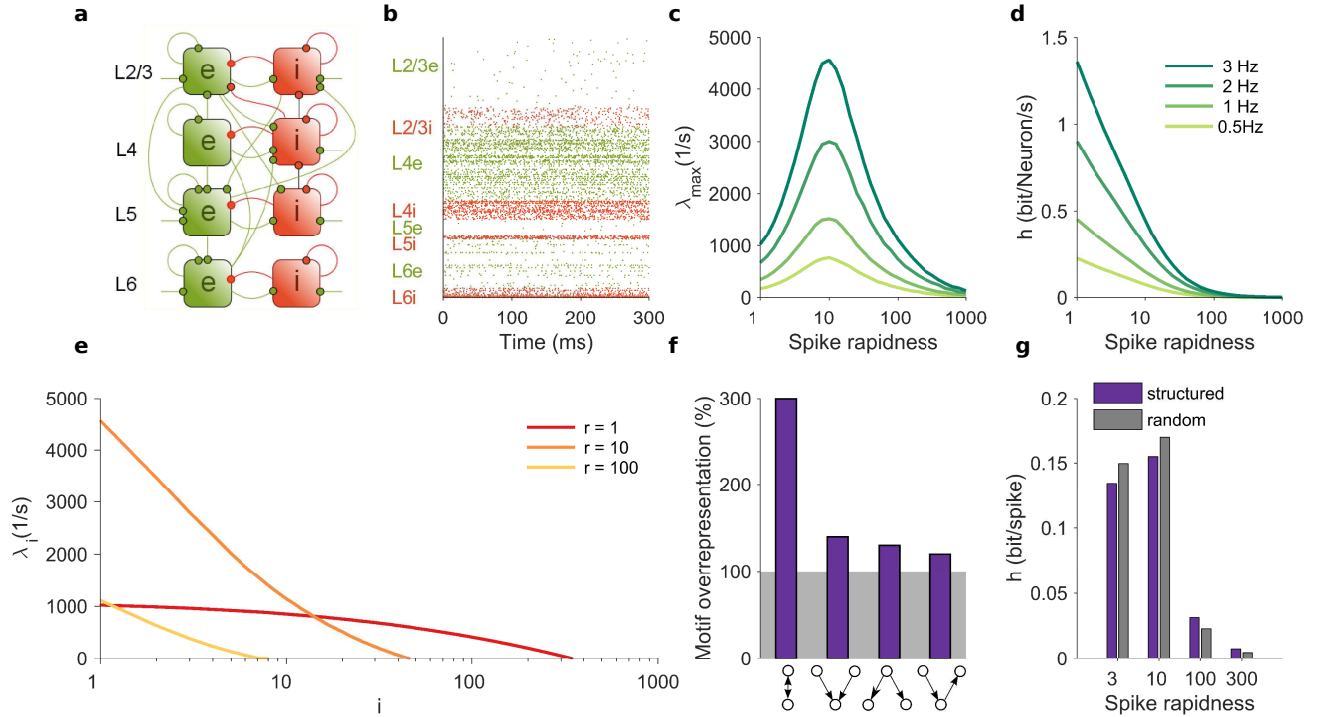


Figure 5. **High spike onset rapidness r reduces chaos and entropy rate in cortical circuit models:** **a** Multilayered cortical column network model with layer- and cell type specific connection probabilities, 77,169 neurons, ~ 285 Million synapses **b** spike raster illustrating layer-specific firing rates **c** largest Lyapunov exponent vs. spike onset rapidness **d** entropy rate h vs. spike onset rapidness r , the gray area indicate a physiologically plausible regime of spike onset rapidness r , **e** positive Lyapunov exponents of multilayered model. **f** Second order network motif overrepresentation estimated from experiments **g** dynamical entropy rate for random and realistic second order motif structure at different values of spike onset rapidness r .

transfer entropy and mutual information rate.

Methods

The governing piecewise differential equation for the single-neuron dynamics is

$$\tau_m \dot{V}_i = \begin{cases} a_U (V_i - V_G)^2 + I_i(t), & V > V_G \\ a_S (V_i - V_G)^2 + I_i(t), & V \leq V_G \end{cases} \quad (1)$$

where τ_m is the membrane time constant, $V_G = \frac{1}{2} \frac{r-1}{r+1}$ is the glue point, $a_S = \frac{r+1}{2r}$ and $a_U = r^2 a_S$ are the curvatures, and the synaptic input current is

$$I_i(t) = -I_T + I_{ext} + \tau_m \sum_{j \in \text{pre}(i)} J \delta(t - t_j^{(s)}) \quad (2)$$

with $I_T = \frac{1}{2} \frac{r}{r+1}$, $J = J_0 / \sqrt{K}$. I_{ext} is adapted to achieve the desired target firing rate $\bar{\nu}$. The elements of the Jacobian of the flow of the dynamics are

$$D_{ij}(t_s) = \begin{cases} 1 + Z'(\phi_{i^*}(t_{s+1}^-)), & \text{for } i = j \in \text{post}(j^*) \\ -\frac{\omega_{i^*}}{\omega_{j^*}} Z'(\phi_{i^*}(t_{s+1}^-)), & \text{for } i \in \text{post}(j^*) \text{ and } j = j^* \\ \delta_{ij} & \text{otherwise} \end{cases} \quad (3)$$

where Z is the phase response curve, $\omega = \frac{2}{\tau_m} \sqrt{I_{ext}/a_S}$ is the phase velocity, and stars indicate the neuron spiking at t_{s+1} . The Kaplan-Yorke attractor dimension is calculated from the interpolated number of Lyapunov exponents that sum to zero:

$$D = k + \frac{\sum_{i=1}^k \lambda_i}{\lambda_{k+1}} \quad \text{where } k = \max_n \left\{ \sum_{i=1}^n \lambda_i \geq 0 \right\}.$$

Acknowledgements

We thank L.F. Abbott, F. Farkhooi, S. Goedeke, D. Hansel, G. Lajoie, L. Logiaco, R.-M. Memmesheimer, A. Neef, A. Palmigiano, M. Puelma Touzel, A. Renart, M. Schottdorf and C. v. Vreeswijk for fruitful discussions. This work was supported by the Deutsche Forschungsgemeinschaft (DFG, German Research Foundation) 436260547 in relation to NeuroNex (National Science Foundation 2015276) & under Germany's Excellence Strategy - EXC 2067/1- 390729940; by the DFG - Project-ID 317475864 - SFB 1286; by the DFG as part of the SPP 2205 - Project-ID 430156276. This work was

further supported by the Leibniz Association (project K265/2019); and by the Niedersächsisches Vorab of the VolkswagenStiftung through the Göttingen Campus Institute for Dynamics of Biological Networks and by the Kavli Foundation and by the Gatsby Charitable Foundation (GAT3708). RE is a Kavli Fellow.

* re2365@columbia.edu

- [1] Polavieja, G. G. de, Harsch, A., Kleppe, I., Robinson, H. P. C. & Juusola, M. Stimulus History Reliably Shapes Action Potential Waveforms of Cortical Neurons. *J. Neurosci.* **25**, 5657–5665 (2005).
- [2] Köndgen, H. et al. The Dynamical Response Properties of Neocortical Neurons to Temporally Modulated Noisy Inputs In Vitro. *Cereb. Cortex* **18**, 2086–2097 (2008).
- [3] Higgs, M. H. & Spain, W. J. Conditional Bursting Enhances Resonant Firing in Neocortical Layer 2–3 Pyramidal Neurons. *J. Neurosci.* **29**, 1285–1299 (2009).
- [4] Tchumatchenko, T., Malyshev, A., Wolf, F. & Volgushev, M. Ultrafast Population Encoding by Cortical Neurons. *The Journal of Neuroscience* **31**, 12171–12179 (2011).
- [5] Ilin, V., Malyshev, A., Wolf, F. & Volgushev, M. Fast Computations in Cortical Ensembles Require Rapid Initiation of Action Potentials. *J. Neurosci.* **33**, 2281–2292 (2013).
- [6] Fourcaud-Trocmé, N., Hansel, D., van Vreeswijk, C. & Brunel, N. How Spike Generation Mechanisms Determine the Neuronal Response to Fluctuating Inputs. *J. Neurosci.* **23**, 11628–11640 (2003).
- [7] Fourcaud-Trocmé, N. & Brunel, N. Dynamics of the Instantaneous Firing Rate in Response to Changes in Input Statistics. *J. Comput. Neurosci.* **18**, 311–321 (2005).
- [8] Naundorf, B., Geisel, T. & Wolf, F. Action Potential Onset Dynamics and the Response Speed of Neuronal Populations. *J. Comput. Neurosci.* **18**, 297–309 (2005).
- [9] Naundorf, B., Wolf, F. & Volgushev, M. Unique features of action potential initiation in cortical neurons. *Nature* **440**, 1060–1063 (2006).
- [10] Naundorf, B., Wolf, F. & Volgushev, M. Neurophysiology: Hodgkin and Huxley model — still standing? (Reply). *Nature* **445**, E2–E3 (2007).
- [11] Wei, W. & Wolf, F. Spike Onset Dynamics and Response Speed in Neuronal Populations. *Phys. Rev. Lett.* **106**, 088102 (2011).
- [12] van Vreeswijk, C. & Sompolinsky, H. Chaos in Neuronal Networks with Balanced Excitatory and Inhibitory Activity. *Science* **274**, 1724–1726 (1996); van Vreeswijk, C. & Sompolinsky, H. Chaotic Balanced State in a Model of Cortical Circuits. *Neural Computation* **10**, 1321–1371 (1998).
- [13] Renart, A. et al. The Asynchronous State in Cortical Circuits. *Science* **327**, 587–590 (2010).
- [14] Bienenstock, E. L., Cooper, L. N. & Munro, P. W. Theory for the development of neuron selectivity: orientation specificity and binocular interaction in visual cortex. *J. Neurosci.* **2**, 32–48 (1982).
- [15] Sussillo, D. & Abbott, L. F. Generating Coherent Patterns of Activity from Chaotic Neural Networks. *Neuron* **63**, 544–557 (2009).
- [16] Sompolinsky, H., Crisanti, A. & Sommers, H. J. Chaos in Random Neural Networks. *Phys. Rev. Lett.* **61**, 259–262 (1988).
- [17] Stern, M., Sompolinsky, H. & Abbott, L. F. Dynamics of random neural networks with bistable units. *Phys. Rev. E* **90**, 062710 (2014).
- [18] Aljadeff, J., Stern, M. & Sharpee, T. Transition to Chaos in Random Networks with Cell-Type-Specific Connectivity. *Phys. Rev. Lett.* **114**, 088101 (2015).
- [19] Harish, O. & Hansel, D. Asynchronous Rate Chaos in Spiking Neuronal Circuits. *PLoS Comput Biol* **11**, e1004266 (2015).
- [20] Kadmon, J. & Sompolinsky, H. Transition to Chaos in Random Neuronal Networks. *Phys. Rev. X* **5**, 041030 (2015).
- [21] Lajoie, G., Thivierge, J.-P. & Shea-Brown, E. Structured chaos shapes spike-response noise entropy in balanced neural networks. *Front. Comput. Neurosci.* **8**, 123 (2014).
- [22] Bernardi, D. & Lindner, B. A frequency-resolved mutual information rate and its application to neural systems. *Journal of Neurophysiology* **113**, 1342–1357 (2015).
- [23] Frederickson, P., Kaplan, J. L., Yorke, E. D. & Yorke, J. A. The Liapunov dimension of strange attractors. *Journal of differential equations* **49**, 185–207 (1983).
- [24] Ledrappier, F. Some relations between dimension and Lyapounov exponents. *Commun. Math. Phys.* **81**, 229–238 (1981).
- [25] Eckmann, J.-P. & Ruelle, D. Ergodic theory of chaos and strange attractors. *Rev. Mod. Phys.* **57**, 617–656 (1985).
- [26] Ledrappier, F. & Young, L.-S. The Metric Entropy of Diffeomorphisms: Part I: Characterization of Measures Satisfying Pesin’s Entropy Formula. *Annals of Mathematics* **122**, 509–539 (1985).
- [27] Benettin, G., Galgani, L., Giorgilli, A. & Strelcyn, J.-M. Lyapunov characteristic exponents for smooth dynamical systems and for Hamiltonian systems - A method for computing all of them. I - Theory. II - Numerical application. *Meccanica* **15**, 9–30 (1980).
- [28] Mazor, O. & Laurent, G. Transient Dynamics versus Fixed Points in Odor Representations by Locust Antennal Lobe Projection Neurons. *Neuron* **48**, 661–673 (2005).
- [29] Machens, C. K., Romo, R. & Brody, C. D. Functional, But Not Anatomical, Separation of ‘What’ and ‘When’ in Prefrontal Cortex. *J. Neurosci.* **30**, 350–360 (2010).
- [30] Mante, V., Sussillo, D., Shenoy, K. V. & Newsome, W. T. Context-dependent computation by recurrent dynamics in prefrontal cortex. *Nature* **503**, 78–84 (2013).
- [31] Gao, P. & Ganguli, S. On simplicity and complexity in the brave new world of large-scale neuroscience. *Current Opinion in Neurobiology* **32**, 148–155 (2015).
- [32] Schneidman, E., Berry, M. J., Segev, R. & Bialek, W. Weak pairwise correlations imply strongly correlated network states in a neural population. *Nature* **440**, 1007–1012 (2006).
- [33] Potjans, T. C. & Diesmann, M. The Cell-Type Specific Cortical Microcircuit: Relating Structure and Activity in a Full-Scale Spiking Network Model. *Cereb. Cortex* **24**, 785–806 (2014).
- [34] Song, S., Sjöström, P. J., Reigl, M., Nelson, S. & Chklovskii, D. B. Highly Nonrandom Features of Synaptic Connectivity in Local Cortical Circuits. *PLoS Biol* **3**, e68 (2005).

- [35] Zhao, L., II, B. B., Netoff, T. & Nykamp, D. Q. Synchronization from second order network connectivity statistics. *Front. Comput. Neurosci.* **5**, 28 (2011).
- [36] R. Zillmer, R. Livi, A. Politi, and A. Torcini, *Phys. Rev. E* **74**, 036203 (2006); S. Jahnke, R. M. Memmesheimer, and M. Timme, *Phys. Rev. Lett.* **100**, 048102 (2008); R. Zillmer, N. Brunel and D. Hansel, *Phys. Rev. E* **79**, 031909 (2009).
- [37] I. Politi, A., Livi, R., Oppo, G.-L. & Kapral, R. Unpredictable Behaviour in Stable Systems. *EPL* **22**, 571 (1993).
- [38] P. E. Latham et al., *J. Neurophysiol.* **83**, 808 (2000); R. Osan and B. Ermentrout, *Neurocomputing* **38**, 789 (2001); D. Hansel and G. Mato, *Neural Comput.* **15**, 1 (2003); B. S. Gutkin, J. Jost and H. C. Tuckwell, *Europhys. Lett.* **81**, 20005 (2008).
- [39] G. B. Ermentrout and N. Kopell, *SIAM J. Appl. Math.* **46**, 233 (1986); B. S. Gutkin and G. B. Ermentrout, *Neural Comput.* **10**, 1047 (1998); J. C. Brumberg and B. S. Gutkin, *Brain Res.* **1171**, 122 (2007)
- [40] Ruelle, D. Large volume limit of the distribution of characteristic exponents in turbulence. *Commun. Math. Phys.* **87**, 287–302 (1982).
- [41] Takeuchi, K. A., Ginelli, F. & Chaté, H. Lyapunov Analysis Captures the Collective Dynamics of Large Chaotic Systems. *Phys. Rev. Lett.* **103**, 154103 (2009).
- [42] London, M., Roth, A., Beeren, L., Häusser, M. & Latham, P. E. Sensitivity to perturbations in vivo implies high noise and suggests rate coding in cortex. *Nature* **466**, 123–127 (2010).
- [43] Monteforte, M. & Wolf, F. Dynamical Entropy Production in Spiking Neuron Networks in the Balanced State. *Phys. Rev. Lett.* **105**, 268104 (2010).
- [44] Monteforte, M. & Wolf, F. Dynamic Flux Tubes Form Reservoirs of Stability in Neuronal Circuits. *Phys. Rev. X* **2**, 041007 (2012).
- [45] Richardson, M. J. E. & Swarbrick, R. Firing-rate response of a neuron receiving excitatory and inhibitory synaptic shot noise. *Phys. Rev. Lett.* **105**, 178102 (2010).
- [46] Richardson, M. J. E. Spike shape and synaptic-amplitude distribution interact to set the high-frequency firing-rate response of neuronal populations. *Phys. Rev. E* **98**, 042405 (2018).
- [47] Richardson, M. J. E. Linear and nonlinear integrate-and-fire neurons driven by synaptic shot noise with reversal potentials. *Phys. Rev. E* **109**, 024407 (2024).

CONTENTS

Neuron model with tunable spike onset	2
Rapid Spikes Enhance Information Transmission	3
Diffusion Approximation fails for Rapid Spike Onset	3
Impact on Dynamical Entropy Rate	4
Transition from <i>Dense</i> to <i>Sparse Chaos</i> with Increasing Spike Onset Rapidness	5
Attractor dimensionality	6
Cortical circuit models	6
Conclusion and summary	6
Methods	8
Acknowledgements	8
References	9
I. The rapid theta neuron model	12
II. Stationary firing rate of the rapid theta neuron	13
III. Stationary characterization of rapid theta neurons driven by inhibitory shot noise	14
IV. Linear response of an ensemble of rapid theta neurons	16
V. High-frequency behavior of rapid theta neurons with inhibitory shot noise	19
VI. Mutual information rate and action potential onset rapidness	24
VII. Phase representation of the rapid theta neuron	30
VIII. Single spike Jacobian of the rapid theta neuron network	32
IX. Setup of network and event-based simulation	34
X. Convergence of the Lyapunov spectra	37
XI. Random matrix theory of the mean Lyapunov exponent	38
XII. Scaling of the largest Lyapunov exponent with network parameters	40
XIII. Participation ratio and localization of chaos	41
XIV. Cellular dynamics propel network chaos at instability events	43
XV. Pairwise correlations in rapid theta networks	44
XVI. Attractor dimension and “entangled” statistics	48
XVII. Network synchrony	49
XVIII. Flux-tube structure of phase space, stable chaos and single-spike perturbations	50
XIX. Poincaré maps of chaotic networks	51
XX. Local Lyapunov exponents reveal stable and unstable phase space regions	52
XXI. Chaos and dynamical entropy rate in structured network topologies	53
XXII. Experimentally measured action potential (AP) onset rapidness in cortical circuits	57

XXIII. Minimal example for Julia	59
XXIV. Scale invariances of the theta model	60
A. Scaling J_0 and ν_w by factor $\alpha > 0$	60
B. Scaling τ_m and J_0 by a Factor $\beta > 0$	60
C. Scaling τ_m and ν_w by a Factor $\gamma > 0$ and $\frac{1}{\gamma}$	61
D. Scale invariances of the rapid theta model	61
References	62

I. THE RAPID THETA NEURON MODEL

To examine the impact of the action potential (AP) onset rapidness on the collective dynamics of cortical networks, we constructed a new neuron model with variable AP onset rapidness, called the rapid theta neuron model (see **Fig. 1** in the main paper). This model is similar to the exponential integrate-and-fire neuron (see Section XXII), but it is much more tractable for high-precision calculations. The rapid theta neuron model combines the advantages of the theta neuron model for the analytical derivation of the phase-response curve with a modifiable AP onset rapidness, denoted as r . For $r = 1$, the rapid theta neuron model is equivalent to the standard theta neuron model [2]. Increasing r decreases the time constant at the unstable fixed point V_U (voltage threshold), leading to greater instability and *sharper* AP initiation. The membrane time constant τ_m , which is the time constant at the stable fixed point V_S (resting potential), remains unchanged. This is achieved by smoothly joining two parabolas at V_G . In the dimensionless voltage representation, the resulting rapid theta neuron model is described by the following piecewise ordinary differential equation:

$$\tau_m \frac{dV}{dt} = \begin{cases} a_S(V - V_G)^2 - I_T + I(t) & \text{for } V \leq V_G \\ a_U(V - V_G)^2 - I_T + I(t) & \text{for } V > V_G. \end{cases} \quad (4)$$

In this equation, I_T denotes the rheobase current, and $I(t)$ is the synaptic input current. The curvatures $a_{U,S}$ depend on the AP onset rapidness r and, together with V_G and I_T , define the positions of the two branches of the parabolas. The glue point, denoted V_G , where the two branches are continuously and smoothly joined, divides the single-neuron phase space into two parts: $V \leq V_G$ and $V > V_G$. At the stable fixed point V_S , the slope of the subthreshold parabola is set to $-1/\tau_m$, and at the unstable fixed point V_U , the slope is r/τ_m . This leads to the following expressions

$$\begin{aligned} \frac{\partial \dot{V}(V_S)}{\partial V} &= -1 = 2a_S(V_S - V_G) \\ a_S &= \frac{1}{2} \frac{1}{(V_G - V_S)} \\ \frac{\partial \dot{V}(V_U)}{\partial V} &= r = 2a_U(V_U - V_G) \\ a_U &= \frac{r}{2} \frac{1}{(V_U - V_G)}. \end{aligned}$$

The derivative of the voltage vanishes at the two fixed points for zero synaptic inputs ($I(t) \equiv 0$). This defines the glueing point V_G and the rheobase current I_T :

$$\begin{aligned} \dot{V}(V_S) = 0 &= a_S(V_S - V_G)^2 - I_T \\ I_T &= \frac{V_G - V_S}{2} \\ \dot{V}(V_U) = 0 &= a_U(V_U - V_G)^2 - I_T \\ &= \frac{rV_U - V_G(r+1) + V_S}{2} \\ V_G &= \frac{rV_U + V_S}{r+1}. \end{aligned}$$

Without loss of generality, we set the stable and unstable fixed points to $V_S = -0.5$ and $V_U = +0.5$, respectively,

yielding:

$$V_G = \frac{1}{2} \frac{r-1}{r+1} \quad (5)$$

$$I_T = \frac{1}{2} \frac{r}{r+1} \quad (6)$$

$$a_S = \frac{r+1}{2r} \quad (7)$$

$$a_U = \frac{r(r+1)}{2} = r^2 a_S. \quad (8)$$

With Eq. (5)-(8) the governing equation of the rapid theta neuron model (4) becomes

$$\tau_m \frac{dV}{dt} = \begin{cases} \frac{r+1}{2r} \left(V - \frac{1}{2} \frac{r-1}{r+1} \right)^2 - I_T + I(t) & V \leq \frac{1}{2} \frac{r-1}{r+1} \\ \frac{r(r+1)}{2} \left(V - \frac{1}{2} \frac{r-1}{r+1} \right)^2 - I_T + I(t) & V > \frac{1}{2} \frac{r-1}{r+1}. \end{cases} \quad (9)$$

II. STATIONARY FIRING RATE OF THE RAPID THETA NEURON

The stationary firing rate of the rapid theta neuron with constant input current follows directly from solving equation 9. The firing rate is determined by the inverse of the time taken for the membrane potential to move from reset ($V = -\infty$) to threshold ($V = \infty$):

$$\nu(I^{\text{ext}}) = \frac{\sqrt{I^{\text{ext}}}}{\pi \tau_m} \sqrt{\frac{2r}{r+1}} \quad (10)$$

where the rheobase current I_T is absorbed in the constant $I^{\text{ext}} = I + I_T$. Cortical neurons are driven by a dense stream of input spikes. The resulting compound spike train can be modeled as a Poisson process, if the input spike trains are uncorrelated and random. However, the superposition of many uncorrelated, non-Poissonian spike trains generally deviates from a Poisson process [24, 25][24, 25]. When many weak and uncorrelated spikes arrive at a neuron, treating the random component of the synaptic currents as Gaussian white noise is justified [26, 27]. Using this diffusion approximation, we obtained the mean firing rate by solving the stationary Fokker-Planck equation with additive Gaussian white noise input current. We start by writing a piecewise Langevin equation for the rapid theta model:

$$\tau_m \frac{dV}{dt} = \begin{cases} a_S(V - V_G)^2 + \mu(t) + \sigma \sqrt{2\tau_m} \xi(t) & V \leq V_G \\ a_U(V - V_G)^2 + \mu(t) + \sigma \sqrt{2\tau_m} \xi(t) & V > V_G \end{cases} \quad (11)$$

where $\xi(t)$ is Gaussian white noise with unit variance, $\sigma \sqrt{2\tau_m}$ is the noise intensity of the input and μ is a constant input comprising the constant external input, the rheobase current and the mean recurrent input. This results in a piecewise Fokker-Planck equation:

$$\frac{\partial P(V, t)}{\partial t} = \begin{cases} \frac{\sigma^2}{\tau_m} \frac{\partial^2 P}{\partial V^2} + \frac{\partial}{\partial V} \left(\frac{-\mu(t) - a_S(V - V_G)^2}{\tau_m} P \right) & V \leq V_G \\ \frac{\sigma^2}{\tau_m} \frac{\partial^2 P}{\partial V^2} + \frac{\partial}{\partial V} \left(\frac{-\mu(t) - a_U(V - V_G)^2}{\tau_m} P \right) & V > V_G \end{cases} \quad (12)$$

where $P(V, t)$ is the time-dependent probability density of finding a neuron at voltage V at time t . The stationary (time-independent) Fokker-Planck equation can be solved numerically using the efficient threshold integration method proposed in [14]. Briefly, the Fokker-Planck equation is set to zero and rewritten as two first-order equations for probability flux and probability density in V :

$$\tau_m \frac{\partial J_0}{\partial V} = \nu_0 \delta(V - V_{\text{th}}) - \nu_0 \delta(V - V_{\text{re}}) \quad (13)$$

$$-\frac{\partial P_0}{\partial V} = \begin{cases} \frac{\tau_m}{\sigma_0^2} \left(\frac{-\mu_0 - a_S(V - V_G)^2}{\tau_m} P_0 + J_0 \right) & V \leq V_G \\ \frac{\tau_m}{\sigma_0^2} \left(\frac{-\mu_0 - a_U(V - V_G)^2}{\tau_m} P_0 + J_0 \right) & V > V_G. \end{cases} \quad (14)$$

Here $P_0(V)$ is the stationary probability distribution of membrane potentials and $J_0(V)$ is the probability flux. As we know the boundary conditions $\lim_{V \rightarrow \infty} P_0(V) = 0$ and $\lim_{V \rightarrow \infty} J_0(V) = \nu_0$, we can simultaneously integrate P_0 and J_0 from threshold to some lower bound V_{lb} . The rate ν_0 is initially unknown but can be scaled out as $p_0 = P_0/\nu_0$. The normalization $\int_{V_{\text{lb}}}^{V_{\text{th}}} P_0 dV = 1$ then yields the firing rate

$$\nu_0 = \left(\int_{V_{\text{lb}}}^{V_{\text{th}}} p_0 dV \right)^{-1} \quad (15)$$

Convergence of the numerical integration of the Fokker-Planck solution: **Fig. 7c** and **d** displays the steady-state firing rate of the stationary solution of the Fokker-Planck approach. As the rapid theta model has neither finite threshold nor finite reset in the voltage representation, the threshold, reset and lower bound of the numerical threshold integration scheme have to be chosen sufficiently far away from zero such that the results do not change (**Fig. 7c**). The integration step size ΔV has to be chosen sufficiently small (**Fig. 7f**). For higher rapidness, smaller step sizes are necessary to get the same precision. This is because there is a drastic change of the dynamics at V_G therefore close to V_G the voltage integration steps have to be small. To increase the numerical accuracy at high rapidness, we chose ΔV , such that both V_{re} and V_G fall on a lattice point of the integration scheme. Code for Julia and MATLAB[®]/Octave is available upon request. We found that setting $V_{\text{th}} = 1000$ and $\Delta V = 10^{-3}$ is sufficient for a relative precision of the firing rate, $\frac{\Delta \nu_0}{\nu_0} < 10^{-2}$.

Diffusion approximation and shot noise: The Fokker-Planck approach approximates the synaptic input as Gaussian white noise. This is justified in the limit of uncorrelated input and large rate of infinitesimally strong received postsynaptic currents per neurons. To investigate the impact of finite postsynaptic potentials, we replaced the Gaussian white noise with inhibitory Poisson pulses of rate $\nu_p = \nu_0 K$ and strength $J_p = -J_0/\sqrt{K}$, keeping the variance $\sigma_p^2 = \nu_p J_p^2 = \nu_0 J_0^2$ fixed and varied K . The mean firing rate ν_0 was kept constant for different values of rapidness r and K by adapting the constant input current μ . For large K , the diffusion approximation is valid, whereas for small K , the shot noise nature of the Poisson input becomes relevant (**Fig. 6c+f**). This effect is particularly strong for large rapidness r . For small K , the density just below V_G obtained from direct numerical simulation is larger than the probability density obtained from the Fokker-Planck solution. The numerical density for small K drops at V_G (**Fig. 6e**). This will help later in understanding the dependence of the largest Lyapunov exponent on K and r . In the next paragraph, we provide additional analysis of the shot noise regime.

III. STATIONARY CHARACTERIZATION OF RAPID THETA NEURONS DRIVEN BY INHIBITORY SHOT NOISE

We start by writing a piecewise stochastic differential equation for the rapid theta model:

$$F(V) = \tau_m \frac{dV}{dt} = \begin{cases} a_S(V - V_G)^2 + I_{\text{ext}} + s(t) & V \leq V_G \\ a_U(V - V_G)^2 + I_{\text{ext}} + s(t) & V > V_G \end{cases} \quad (16)$$

where $s(t)$ represents inhibitory input spikes arriving at rate R with amplitude $\frac{-J_0}{\sqrt{K}}$. The inhibitory input $s(t)$ can be represented as a sum of inhibitory spikes: $s(t) = \sum_k \frac{-J_0}{\sqrt{K}} \delta(t - t_k)$ where t_k are the Poisson-distributed spike arrival times with rate $R = K\nu$. Each input spike causes a decrement of $\frac{-J_0}{\sqrt{K}}$ in the membrane potential. Thus, the neuron's stochastic differential equation (SDE) is:

$$dV(t) = F(V)dt + ds(t)$$

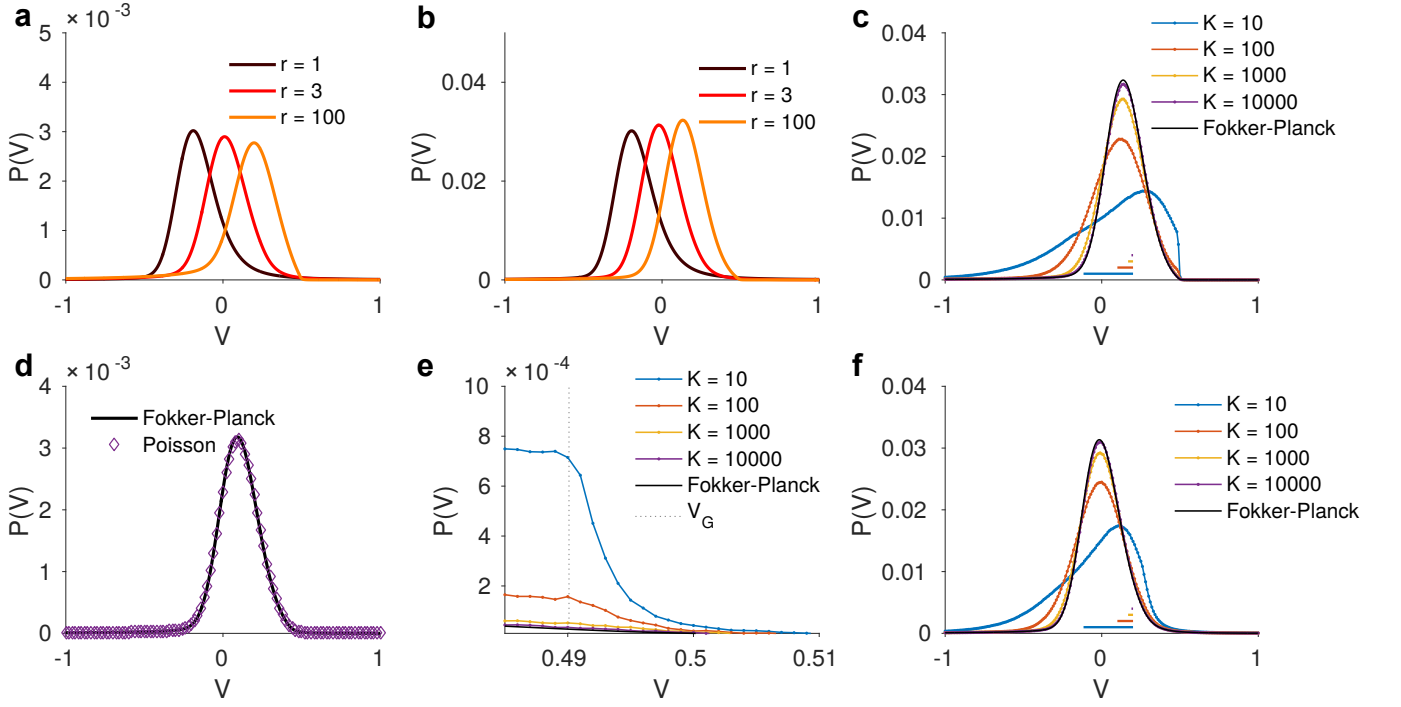


Figure 6. **Action potential onset rapidness r shapes stationary voltage distribution.** **a)** Voltage distribution for different rapidness for fixed external input obtained from the solution of the stationary Fokker Planck equation Eq. 13 and Eq. 14 **b)** same as **a**, but for fixed mean firing rate. **c)** Voltage distribution obtained with inhibitory Poisson input spikes trains. For small K , the shot noise nature of the Poisson input becomes important. ($r = 100$) **d)** Comparison of Poisson input and Fokker Planck solution for $K = 10000$ and $r = 10$. **e)** same as **c)** zoomed in for $r = 10$. The probability density drops at V_G . **f)** same as **c)** for $r = 3$ (parameters: $\nu_0 = 1$ Hz, $J_0 = 1$, $\tau_m = 10$ ms).

or explicitly including the jumps:

$$dV(t) = F(V)dt - J dN(t)$$

where $N(t)$ is a Poisson process with rate R , and $dN(t)$ represents the number of spikes in the interval $[t, t + dt)$. We consider a population of neurons described by the probability density $P(V, t)$ of the membrane potential V at time t . The continuity equation for $P(V, t)$ is:

$$\frac{\partial P(V, t)}{\partial t} + \frac{\partial J(V, t)}{\partial V} = 0$$

where $J(V, t)$ is the probability flux. The total flux $J(V, t)$ consists of two components: The drift flux $J_{\text{drift}}(V, t)$, due to the deterministic dynamics $f(V)$ and the jump flux $J_{\text{jump}}(V, t)$ due to the inhibitory Poisson input.

$$J(V, t) = J_{\text{drift}}(V, t) + J_{\text{jump}}(V, t).$$

We next describe $\frac{dV}{dt} = F(v) + s(v, t)$. with driving force

$$F(v) = \begin{cases} \frac{1}{\tau} (a_S (V - V_G)^2 + \mu) & V \leq V_G \\ \frac{1}{\tau} (a_U (V - V_G)^2 + \mu) & V > V_G \end{cases}.$$

The voltage trajectories of a population of neurons, each obeying the voltage dynamics with an uncorrelated but statistically identical realization of the stochastic drive in can be described by a probability density $P(V, t)$. The stochastic single neuronal dynamics allow for the construction of a master equation that describes the deterministic dynamics of the ensemble at the population level. As well as the probability density, it is convenient to consider the probability flux $J(V, t)$. This describes the flow-rate of trajectories passing a particular voltage. Note that the flux at threshold $J(V_{th})$ is equal to the instantaneous spike-rate $\nu(t)$ of the population with the flow then reinserted at the

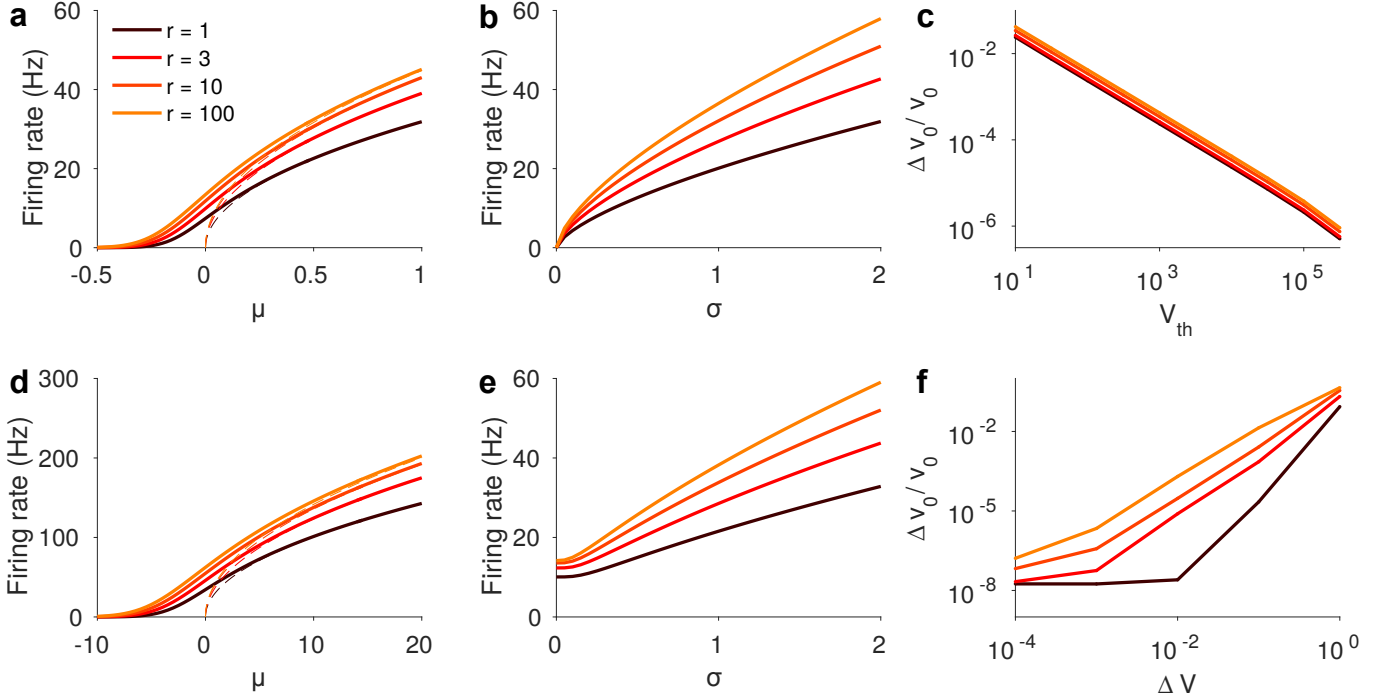


Figure 7. **Spike onset rapidness r mildly affects steady-state firing rate.** **a)** Firing rate as a function of constant input μ for different values of rapidness obtained from stationary Fokker-Planck solution for weak noise ($\sigma = \sqrt{0.05}$). Dashed line is analytical noise-free result (Eq. 10). **b)** same as **a)** for varying noise strength σ at $\mu = I_T$. **c)** rate deviation for different threshold levels of numerical integration scheme. **d)** same as **a)** for strong noise ($\sigma = \sqrt{0.5}$) **e)** same as **b)** for strong constant input $\mu = 0.1 + I_T$ **f)** rate deviation for different integration step sizes in the numerical integration scheme (parameters: $\tau_m = 10$ ms, $V_{re} = -V_{th}$, $\Delta V = 10^{-3}$, $V_{th} = 10^3$).

reset V_{re} . These quantities are connected by a continuity equation

$$\frac{\partial P}{\partial t} + \frac{\partial J}{\partial V} = \nu(t) (\delta(V - V_{re}) - \delta(V - V_{th}))$$

The stationary continuity equation that takes the form of a delay differential equations (DDE) [84]:

$$\frac{d}{dV} [P(V)F(V)] = \bar{\nu} [P(V - C) - h(V)P(V)] + \rho [\delta(V - V_{re}) - \delta(V - V_{th})]$$

with the average firing rate $\bar{\nu}$. We solve this delay differential equations by the method of steps using higher-order solvers with high accuracy by setting up a threshold integration analogously to the established threshold-integration method proposed in [14] as proposed for the DDE in [84]. Again, the unknown rate $\bar{\nu}$ can be scaled out as $\bar{p} = \bar{P}/\bar{\nu}$. The normalization $\int_{V_{lb}}^{V_{th}} \bar{P} dV = 1$ then yields the $\bar{\nu} = \left(\int_{V_{lb}}^{V_{th}} \bar{p} dV \right)^{-1}$ with the initial condition $\bar{p}(V_{th}) = 1/F(V_{th})$. We find excellent agreement between the voltage distribution obtained by solving the delay differential equations with network simulations in Figure 8, where we usually use bisectioning to adapt the external input current to achieve a target firing rate $\bar{\nu}$. We note that for large rapidness r , we find systematic deviations of $P(V)$ from the Fokker-Planck approach close to the unstable fixed point V_U , that are captured well by the DDE. As expected, for large values of K . We further note that there exist deviations for finite network size N even for the DDE solution, that probably stem from the fact that the DDE approach ignores pairwise correlations and population fluctuations.

IV. LINEAR RESPONSE OF AN ENSEMBLE OF RAPID THETA NEURONS

Figure 1 e of main paper. We calculated the linear response of ensembles of rapid theta neurons using three different approaches: first, by solving the time-dependent Fokker-Planck-equation; second, by direct numerical simulation

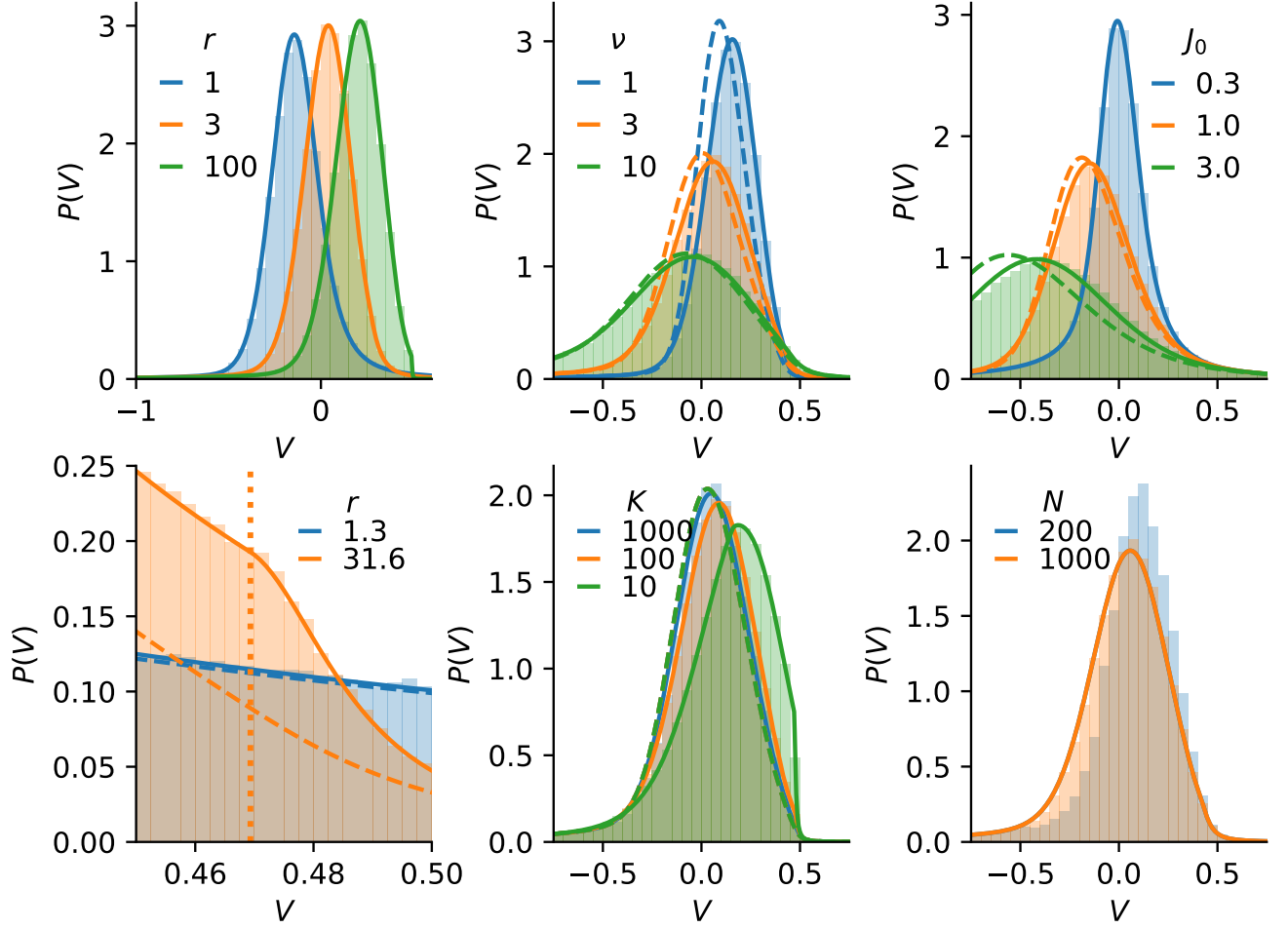


Figure 8. **Shot noise affects stationary voltage distribution.** a) Voltage distribution for different rapidness for fixed external input obtained analytically from solving continuity equation with shot noise, transparent histogram shows network simulation b) same as a) for different firing rates μ , dashed lines is solution to Fokker-Planck equation. c) Voltage distribution obtained with inhibitory Poisson input spikes trains. For small K , the shot noise nature of the Poisson input becomes important. ($r = 100$) d) Comparison of Poisson input and Fokker Planck solution for $K = 10000$ and $r = 10$. e) same as c) zoomed in for $r = 10$. The probability density drops at V_G . f) same as c) for $r = 3$ (parameters: $\nu_0 = 1$ Hz, $J_0 = 1$, $\tau_m = 10$ ms).

using Poisson input; and third, by direct numerical simulations using band-limited white noise. The same efficient numerical threshold integration method used for the stationary response can be adapted to obtain the linear response to a sinusoidal modulation of the input current. A modulation of the mean input current, $\mu(t) = \mu_0 + \mu_1 e^{i\omega t}$, results in a firing rate modulation, which in linear response is $\nu(t) = \nu_0 + \hat{\nu}_\mu e^{i\omega t}$. The absolute value $|\hat{\nu}_\mu(\omega)|$ represents the rate modulation strength, and the phase of $\hat{\nu}_\mu(\omega)$ gives the phase lag between input and output modulation. The expansion of the flux in first order therefore satisfies:

$$\tau_m \frac{\partial \hat{J}_\mu}{\partial V} = i\omega \hat{P}_\mu + \hat{\nu}_\mu \delta(V - V_{th}) - \hat{\nu}_\mu \delta(V - V_{re}) \quad (17)$$

$$-\frac{\partial \hat{P}_\mu}{\partial V} = \begin{cases} \frac{\tau_m}{\sigma_0^2} \left(\frac{-\mu_0 - a_S(V - V_G)^2}{\tau_m} \hat{P}_\mu + \hat{J}_\mu + F_\mu \right) & V \leq V_G \\ \frac{\tau_m}{\sigma_0^2} \left(\frac{-\mu_0 - a_U(V - V_G)^2}{\tau_m} \hat{P}_\mu + \hat{J}_\mu + F_\mu \right) & V > V_G. \end{cases} \quad (18)$$

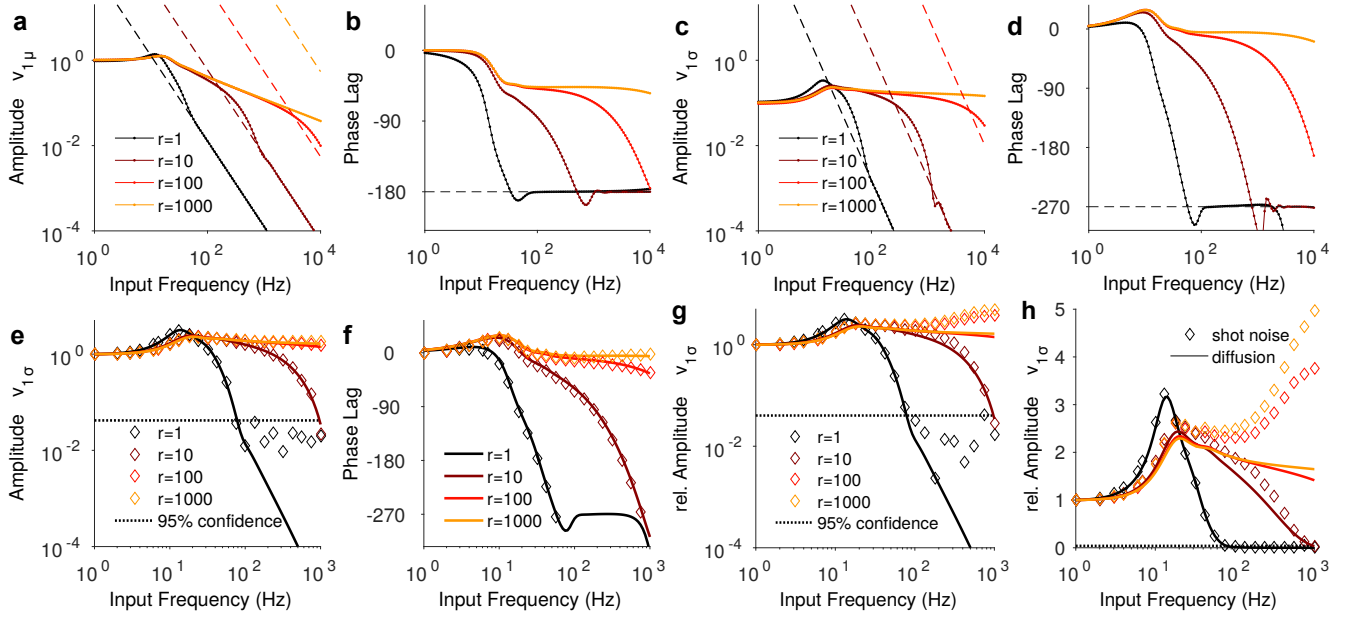


Figure 9. **Action potential onset rapidness r drastically shapes linear firing rate response: Fokker-Planck approach (FPA) vs. direct numerical simulations (DNS) vs. high-frequency analytical solution (HFA)** **a)** Linear response for mean modulation of input current. Increasing rapidness leads to a higher cutoff frequency. Full lines are FPA, dashed lines correspond to HFA (Eq. 23). **b)** Phase lag for different input frequencies. **c)** and **d)** the same as **a)**+**b)** for modulation of variance of the input current. **e)** Comparison of DNS (diamonds) and FPA (full line) for variance modulation with $K = 1000$. Dashed line indicates 95% significance threshold for DNS. **f)** Same as **e)** for $K = 30$. For large values rapidness and large input frequencies, the shot noise becomes noticeable. **g)** Impact of shot noise: Same as **e)** for $K = 1000$. **h)** Same as **g)** with linear amplitude axis (parameters: $\nu_0 = 10$ Hz, $K = 1000$, $\tau_m = 10$ ms.)

F_μ describes the inhomogeneous term given by $F_\mu = -\frac{\partial J}{\partial \mu} P_0 = -\frac{\mu_1 P_0}{\tau_m}$. The boundary conditions are $\lim_{V \rightarrow \infty} \hat{P}_\mu(V) = 0$ and $\lim_{V \rightarrow \infty} \hat{J}_\mu(V) = \hat{\nu}_\mu$. The solution can be separated into two parts, one proportional to $\hat{\nu}_\mu$ and a second proportional to μ_1 .

$$\hat{P}_\mu = \hat{\nu}_\mu \hat{p}_\nu + \mu_1 \hat{p}_\mu \text{ and } \hat{J}_\mu = \hat{\nu}_\mu \hat{j}_\nu + \mu_1 \hat{j}_\mu \quad (19)$$

The resulting pair of equations can be numerically integrated yielding the linear response rate amplitude and phase lag.

Similarly, for variance modulations of the input current, the expansion of the flux satisfies in first order:

$$\tau_m \frac{\partial \hat{J}_{\sigma^2}}{\partial V} = i\omega \hat{P}_{\sigma^2} + \hat{\nu}_{\sigma^2} \delta(V - V_{th}) - \hat{\nu}_{\sigma^2} \delta(V - V_{re}) \quad (20)$$

$$-\frac{\partial \hat{P}_{\sigma^2}}{\partial V} = \begin{cases} \frac{\tau_m}{\sigma_0^2} \left(\frac{-\mu_0 - a_S (V - V_G)^2}{\tau_m} \hat{P}_{\sigma^2} + \hat{J}_{\sigma^2} + F_{\sigma^2} \right) & V \leq V_G \\ \frac{\tau_m}{\sigma_0^2} \left(\frac{-\mu_0 - a_U (V - V_G)^2}{\tau_m} \hat{P}_{\sigma^2} + \hat{J}_{\sigma^2} + F_{\sigma^2} \right) & V > V_G. \end{cases} \quad (21)$$

The inhomogeneous term F_{σ^2} is defined by $F_{\sigma^2} = -\frac{\partial J}{\partial \sigma^2} P_0$. It is given by

$$F_{\sigma^2} = \begin{cases} \frac{\sigma_1^2}{\sigma_0^2} (-\mu - a_S (V - V_G)^2 - V_T) & V \leq V_G \\ \frac{\sigma_1^2}{\sigma_0^2} (-\mu - a_U (V - V_G)^2 - V_T) & V > V_G. \end{cases} \quad (22)$$

The linear response of the Fokker Planck ansatz (FPA) is obtained with the same threshold integration scheme as above. We solve the linear response for the delay differential equation (DDE) similarly as above by the method of steps

using higher-order solvers with high accuracy by setting up a threshold integration analogously to the established threshold-integration method proposed in [14], extending the previous DDE approach in [84] from the stationary case to the time-dependent case. A more detailed account of this method will be given elsewhere. We find excellent agreement between the DDE approach and direct numerical simulations using forward Euler in **Fig. 11**. We note as described in the main text and in more detail below, that we observe a mismatch between the predictions of the FPA and direct numerical simulations especially for large r , and large J_0 in a regime of intermediate to high frequencies, which we explain by a breakdown of the diffusion approximation. This breakdown of the diffusion approximation is related but different from the breakdown of the diffusion approximation described previously [95]. As we are concerned about the inhibition-dominated balanced regime on recurrent spiking networks, we focus here on the effect of inhibitory shot-noise, in contrast to [95] that focused on excitatory shot noise in EIF neurons with exponentially distributed synaptic weights and also found an effect of shot noise for small δ_T/a_s , corresponding to large rapidness or large synaptic amplitude. A more recent paper extended that to conductance-based integrate-and-fire neurons and considered both excitation and inhibition, but did not report the breakdown of the diffusion approximation for large rapidness r discussed here [97]. We finally note that the Fokker-Planck ansatz has the identical asymptotic limit for large frequencies, but that shot noise effects become relevant in an intermediate frequency range when r and the synaptic amplitude are large. This is also different from the previously described excitatory shot-noise effect that changes also the asymptotic exponent of the frequency-response, due to the model choice (EIF) and the choice of an exponential synaptic weight distribution [95].

High-frequency limit: The high-frequency response is obtained by expanding $\hat{P}(t)$ in terms of $\frac{1}{\omega}$, similarly to [14, 16]. The response to modulations of the mean is:

$$\hat{\nu}_\mu(\omega) = \nu_0 \mu_1 r(r+1) \frac{1}{(i\omega\tau_m)^2} \quad (23)$$

The high-frequency response for modulations of the variance is:

$$\hat{\nu}_\sigma(\omega) = 3\nu_0 \sigma_1^2 r^2 (r+1)^2 \frac{1}{(i\omega\tau_m)^3} \quad (24)$$

The excellent agreement between analytical high-frequency response and the Fokker-Planck approach is shown in **Fig. 9**. Building on previous work, the functional form of the voltage dependence of the activation variable of fast sodium currents determines how well the spiking of a fluctuation-driven neuron can reflect high frequency input [16–20]. High spike onset rapidness allows neurons to precisely position their spikes in time. Neurons with low spike onset rapidness are susceptible to input fluctuations after crossing the unstable fixed point V_U . High-frequency components in the input are then washed out and only weakly reflected in the spiking. Therefore, in the presence of noise, the spikes of neurons with high action potential onset rapidness can convey more information about high-frequency input currents. To support this claim quantitatively, we calculated a lower bound on the mutual information rate between input current and spike trains (Section VI).

Analytical high-frequency response for high rapidness limit: The high-frequency response in the limit of large rapidness is also obtained by expanding $\hat{P}(t)$ in $\frac{1}{\omega}$ for $r = \infty$. In this case $V_G = V_U$ acts as a hard threshold and neurons crossing it spike instantaneously. The high-frequency response to modulations of the mean is similar to that of the leaky integrate-and-fire neuron:

$$\hat{\nu}_\mu = \frac{\nu_0 \mu_1}{\sqrt{i\omega\tau_m}} \quad (25)$$

V. HIGH-FREQUENCY BEHAVIOR OF RAPID THETA NEURONS WITH INHIBITORY SHOT NOISE

The rapid theta neuron model in rescaled variables is given by

$$F(V) := \frac{dV}{dt} = \begin{cases} (I + a_s V^2)/\tau & V < 0 \\ (I + a_u V^2)/\tau & V \geq 0 \end{cases} \quad (26)$$

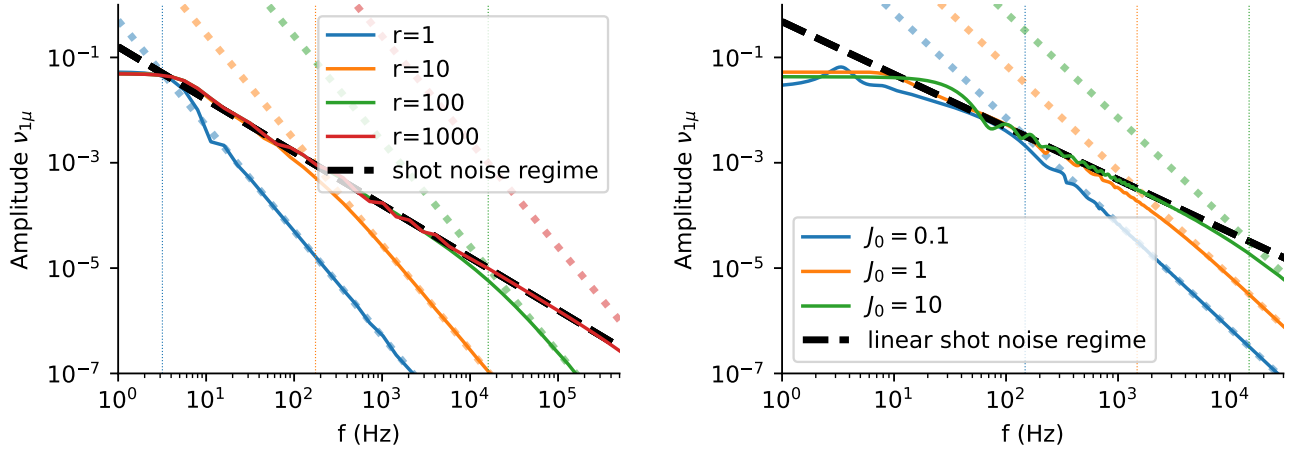


Figure 10. **Qualitative change in population response of shot-noise-driven rapid theta neurons to synaptic rate modulations:** **a)** Linear response for mean modulation of synaptic input rate for varying spike onset rapidness r . Dotted lines represent the high-frequency asymptotics (Eq. 28), while the black dashed line corresponds to the linear shot-noise limit (Eq. 29). For smaller r , the frequency response transitions to a decay proportional to $\frac{1}{f^2}$ at much lower frequencies compared to larger values of r . **b)** Same as **a)** for varying coupling strength J_0 . Weak coupling ($J_0 = 0.1$) begins to fall off proportional to $\frac{1}{f^2}$ at lower frequencies compared to larger values of r ($J_0 = 10$). (parameters: $\nu_0 = 1$ Hz, $K = 100$, $\tau_m = 10$ ms.)

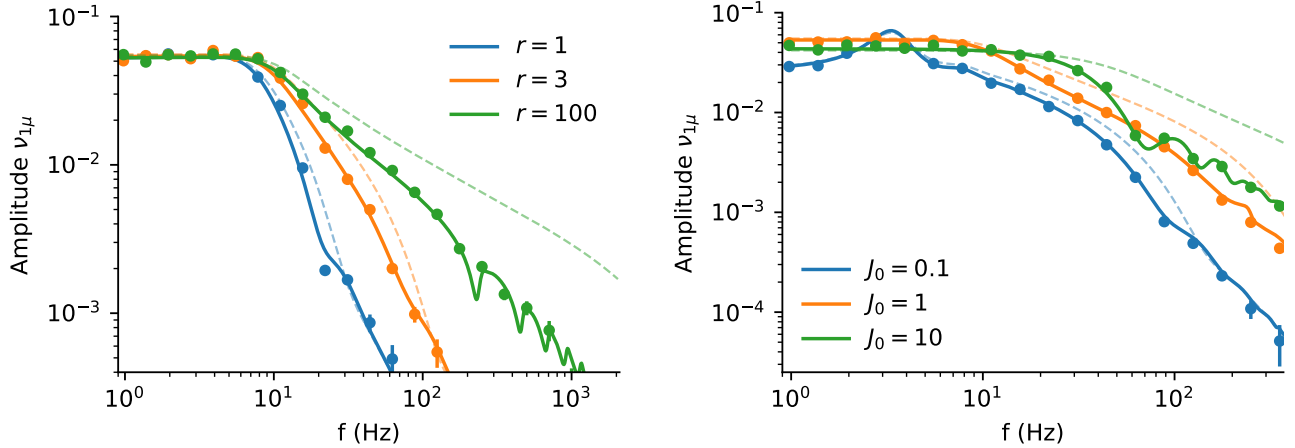


Figure 11. **Frequency response of rapid theta neurons driven by inhibitory shot-noise, described by Fokker-Planck ansatz:** **a)** Linear response for mean modulation of synaptic input rate for varying spike onset rapidness r . Full lines are the shot-noise theory, dashed lines are the Fokker-Planck theory dots are direct numerical simulations using Forward Euler. Note that for large rapidness, the direct numerical simulations are not well-captured by the Fokker-Planck theory but agree well with the predictions by the shot-noise theory. This confirms that the diffusion approximation inherent to the Fokker-Planck ansatz breaks down for large r . **b)** Same as **a)** for varying coupling strength J_0 . (parameters: $\nu_0 = 3$ Hz, $K = 100$, $\tau_m = 10$ ms. a) $J_0 = 1$, b) $r = 10$)

where V represents the rescaled voltage, I is the constant input current between two incoming spikes, a_s and a_u are parameters controlling the voltage dynamics below and above $V = 0$, respectively, and τ is the time constant. We consider the regime $I > 0$, ensuring that $F(V) > 0$.

We consider rapid theta neurons subject to inhibitory Poisson input with a time-dependent rate $R(t) = \bar{R} + \hat{R}e^{i\omega t}$ and a negative amplitude $W < 0$. \bar{R} denotes the average input rate and \hat{R} is the modulation amplitude. Similarly, the resulting firing rate is by $\nu(t) = \bar{\nu} + \hat{\nu}e^{i\omega t}$.

For large values of V , the flux $J(t)$ approximates the firing rate $\nu(t)$, and the stationary voltage probability density

$P(V)$ is given by

$$\bar{P}(V) \approx \frac{\bar{v}}{F(V)} \approx \frac{\bar{v}\tau}{a_u V^2}.$$

where we ignored I in the denominator because $a_u V^2$ dominates for large V . The stationary shot noise flux $\bar{J}_s(V)$, representing voltage jumps induced by incoming spikes, is approximated as

$$\begin{aligned} \bar{J}_s(V) &\approx \bar{R} \int_V^{V+W} \bar{P}(u) du \\ &\approx \bar{R} \int_V^{V+W} \frac{\bar{v}\tau}{a_u y^2} dy \\ &= \frac{\bar{v}\tau W \bar{R}}{a_u V(V+W)} \end{aligned}$$

The high-frequency response $\hat{r}(\omega)$ is expressed as the Laplace transform of the steady-state shot-noise flux:

$$\hat{r}(\omega) = \frac{\hat{R}}{\bar{R}} \int_0^\infty e^{-\lambda} \bar{J}_s(\lambda, \omega) d\lambda,$$

where $\lambda(V, \omega) := i\omega T(V)$. The escape time $T(V)$ from voltage V to spike time $V = \infty$ is approximated as:

$$T(V) = \int_V^\infty \frac{dy}{F(y)} \approx \int_V^\infty \frac{\tau}{a_u y^2} dy = \frac{\tau}{a_u V}.$$

Thus,

$$\lambda = i\omega T = \frac{i\omega\tau}{a_u V}, \quad \text{and hence} \quad V = \frac{i\omega\tau}{a_u \lambda}.$$

Plugging this into $\bar{J}_s(V)$, we get:

$$\bar{J}_s(\lambda, \omega) = \frac{\bar{v}\tau W \bar{R}}{a_u \frac{i\omega\tau}{a_u \lambda} \left(\frac{i\omega\tau}{a_u \lambda} + W \right)} = \frac{\bar{v}\tau \bar{R} \lambda^2}{i\omega\tau \left(\frac{i\omega\tau}{a_u W} + \lambda \right)}.$$

The high-frequency response $\hat{v}(\omega)$ becomes

$$\begin{aligned} \hat{v}(\omega) &= \frac{\hat{R}}{\bar{R}} \int_0^\infty e^{-\lambda} \bar{J}_s(\lambda, \omega) d\lambda \\ &= \hat{R} \bar{v} \tau \int_0^\infty \frac{\lambda^2 e^{-\lambda}}{i\omega\tau \left(\frac{i\omega\tau}{a_u W} + \lambda \right)} d\lambda \end{aligned} \tag{27}$$

Let $x = \frac{i\omega\tau}{a_u W}$ and $t = \lambda + x$, so $\lambda = t - x$ and $d\lambda = dt$. The limits of integration become x to ∞ . Then the integral becomes

$$\begin{aligned} \hat{v}(\omega) &= \frac{\hat{R} \bar{v} e^x}{i\omega} \left[\int_x^\infty t e^{-t} dt - 2x \int_x^\infty e^{-t} dt + x^2 \int_x^\infty \frac{e^{-t}}{t} dt \right] \\ &= \hat{R} \bar{v} \left[\frac{2}{i\omega} - \frac{2\tau}{a_u W} - \frac{\omega\tau^2}{(a_u^2 W^2)} e^{\frac{i\omega\tau}{a_u W}} E_1 \left(\frac{i\omega\tau}{a_u W} \right) \right] \end{aligned}$$

where $E_1(x)$ is the exponential integral function, $E_1(z) = \int_z^\infty \frac{e^{-t}}{t} dt$.

The expression Eq. 27 contains two terms in the denominator, and depending on which term dominates, different behaviors of \hat{r} emerge. We will now analyze all possible regimes and develop analytical transition conditions between these regimes.

Quadratic Asymptotic Regime (large ω): For very large ω (i.e., $\omega\tau \gg 1, a_u, W$), the term involving ω^2 dominates the denominator. The denominator simplifies to:

$$D_1(\lambda) \approx -\frac{\omega^2\tau^2}{a_u W}.$$

Thus, the response becomes:

$$\begin{aligned} \hat{v}(a_u, \omega, W) &\approx -\hat{R}\bar{v} \int_0^\infty d\lambda e^{-\lambda} \frac{a_u \lambda^2}{\omega^2 \tau^2} \\ &= -\hat{R}\bar{v} \tau \frac{a_u}{(\omega\tau)^2} \int_0^\infty d\lambda e^{-\lambda} \lambda^2 \\ &= -\frac{2a_u \hat{R}\bar{v}}{\omega^2 \tau}. \end{aligned} \quad (28)$$

Here, we used $\int_0^\infty d\lambda e^{-\lambda} \lambda^2 = 2$.

Linear Shot Noise Regime (large W , large r) When a_u and W are large and $\omega^2/(a_u \lambda^2)$ is not dominant, the term $\frac{2i\omega W}{\lambda}$ dominates the denominator:

$$D_2(\lambda) \approx \frac{2i\omega W}{\lambda}.$$

The response becomes:

$$\hat{v}(a_u, \omega, W) \approx W \hat{R}\bar{v} \int_0^\infty d\lambda e^{-\lambda} \frac{\lambda}{2i\omega W} = \frac{\hat{R}\bar{v}}{2i\omega} \int_0^\infty d\lambda e^{-\lambda} \lambda = \frac{\hat{R}\bar{v}}{2i\omega}. \quad (29)$$

We used $\int_0^\infty d\lambda e^{-\lambda} \lambda = 1$.

Constant Regime For low frequencies ω , the linear response \hat{r} can be estimated using an adiabatic approximation, we perform a linear expansion of the steady-state firing rate \bar{v} with respect to small perturbations in the input rate \hat{R} :

$$\hat{v}_{\text{adiabatic}}(a_u, \omega, W) \approx \frac{d\bar{v}}{dR} \hat{R}$$

$$\hat{v}_{\text{adiabatic}}(a_u, \omega, W) \approx -\frac{1}{2} \frac{W\tau \hat{R} \sqrt{\bar{v}}}{\sqrt{R}}$$

Transition Between Quadratic and Linear Regime Set the quadratic frequency term equal to the linear frequency term:

$$\left| -\frac{\omega^2 \tau^2}{a_u \lambda^2} \right| \approx \left| \frac{2i\omega \tau W}{\lambda} \right|$$

Assuming the most significant contributions come from $\lambda \approx 1$:

$$\omega_{\text{transition}} \approx \frac{2a_u W}{\tau}$$

This transition happens at a value of $|\hat{\nu}|$ of

$$|\hat{\nu}_{\text{transition}}| = W \hat{R} \bar{\nu} \frac{2a_u}{\omega_{\text{transition}}^2 \tau^2} = W \hat{R} \bar{\nu} \frac{2a_u}{(2a_u W)^2} = \frac{\hat{R} \bar{\nu} \tau}{2W a_u}$$

Linking shot noise to recurrent network dynamics To convert back to the variables used in recurrent neural network, we have to first go back to the original rapid theta model without rescaled variables and then replace R by compound input spike rate $K\bar{\nu}$, where K is the number of synapses per neuron and $\bar{\nu}$ is the average firing rate. Moreover, we set $W = J_0/\sqrt{K}$, which is the balanced scaling of the negative coupling strength that maintains a finite variance of the input for large K . Moreover, we remember that $a_u = r(r+1)/2$.

This gives for the 'quadratic regime' (large ω limit):

$$\hat{\nu}_{\text{I}}(a_u, \omega, W) = -\frac{2W \hat{R} \bar{\nu} a_u}{\omega^2 \tau^2}.$$

For the linear 'shot noise regime' (large W and large r):

$$\hat{\nu}_{\text{II}}(a_u, \omega, W) = \frac{\hat{R} \bar{\nu} \tau}{2i\omega \tau}.$$

Thus, the intersection of the linear and quadratic regime is at:

$$\omega_{\text{transition}} \approx \frac{2a_u W}{\tau}$$

which corresponds to a value of $|\hat{\nu}|$ of

$$|\hat{\nu}_{\text{critical}}| = W \hat{R} \bar{\nu} \tau \frac{2a_u}{\omega_{\text{transition}}^2 \tau^2} = W \hat{R} \bar{\nu} \tau \frac{2a_u}{(2a_u W)^2} = \frac{\hat{R} \bar{\nu} \tau}{2W a_u}$$

To determine if the linear shot noise regime contributes at all, we have to determine if the transition between quadratic and linear regime happens before or after the constant regime dominates with $|\hat{\nu}_{\text{constant}}| = \frac{\hat{R}}{\sqrt{K}}$

$$|\hat{\nu}_{\text{transition}}| = W \hat{R} \bar{\nu} \tau \frac{2a_u}{\omega_{\text{transition}}^2 \tau^2} = W \hat{R} \bar{\nu} \tau \frac{2a_u}{(2a_u W)^2} = \frac{\hat{R} \bar{\nu} \tau}{2W a_u} = \frac{\hat{R}}{\sqrt{K}}$$

Plugging in $a_u = \frac{r(r+1)}{2}$ and $W = \frac{J_0}{\sqrt{K}}$ gives:

$$|\hat{\nu}_{\text{transition}}| = \frac{\hat{R} \bar{\nu} \tau}{J_0 r(r+1)} = \frac{\hat{R}}{\sqrt{K}}$$

Solving by r gives:

$$r = \frac{\sqrt{1 + 4 \frac{K \bar{\nu} \tau}{J_0}} - 1}{2}$$

For large r this is

$$r \approx \sqrt{\frac{K \bar{\nu} \tau}{J_0}}$$

Compare to $r_{\text{localization}}$

$$r_{\text{localization}} \propto \sqrt{\frac{K \nu_0 \tau_m}{J_0}}.$$

and

$$r_{\text{peak}} \propto \sqrt{\frac{K\nu_0\tau_m}{J_0}}$$

VI. MUTUAL INFORMATION RATE AND ACTION POTENTIAL ONSET RAPIDNESS

Figure 1 h of main paper.

Lower bound on mutual information rate: Using information theory, we can treat a neuron as a noisy communication channel, transforming a signal embedded in a noisy current into a spiking response sent to its postsynaptic partners. The mutual information rate measures how much the uncertainty about the input $x(t)$ is reduced given the spiking output $y(t)$ per unit time:

$$R(X, Y) = h(Y) - h(Y|X) = h(X) - h(X|Y) = \lim_{T \rightarrow \infty} \frac{1}{T} \int_X \int_Y p(x, y) \log_2 \left(\frac{p(x, y)}{p(x)p(y)} \right) \quad (30)$$

where $p(x, y)$ is the joint probability density function of $x(t)$ and $y(t)$, $h(X)$ and $h(Y)$ are their entropy rates, and $h(X|Y)$ is the conditional entropy rate of $x(t)$ given $y(t)$. The continuous Gaussian channel provides a lower bound on the mutual information rate for a Gaussian input signal [28, 29]:

$$R(X, Y) = h(X) - h(X|Y) \geq h(X) - h_{\text{Gaussian}}(X|Y) = R_{\text{lb}}(X, Y) \quad (31)$$

The inequality results from the property that a Gaussian process has the maximum entropy of all processes with fixed variance. Recently, it was shown that for moderate input modulation in a fluctuation-driven regime, this lower bound is very close to the mutual information rate estimated from direct methods [11]. This is convenient because estimating the mutual information from empirical data is computationally costly, requiring the sample size to be much larger than the size of the alphabet [23]. Continuous processes usually have to be discretized resulting in very large alphabets. In our case, a Gaussian channel approximation to the mutual information rate between input current and output spike train was estimated based on the spectral coherence between input current and output spike train, which relies purely on second-order statistics.

$$R_{\text{lb}}(X, Y) = - \int_0^{f_{\text{cutoff}}} df \log_2 (1 - C_{xy}(f)), \quad (32)$$

where $C_{xy}(f)$ denotes the magnitude squared spectral coherence. The spectral coherence is the frequency-domain analog of correlation, measuring the linear relationship between frequency components of input and output signal. Its magnitude squared is

$$C_{xy}(f) = \frac{|S_{xy}(f)|^2}{|S_{xx}(f)||S_{yy}(f)|} \quad (33)$$

$S_{xx}(f)$ is the power spectrum of band-limited Gaussian white noise:

$$S_{xx}(f) = \begin{cases} \sigma^2 & f \leq f_{\text{cutoff}} \\ 0 & \text{else.} \end{cases} \quad (34)$$

$S_{yy}(f)$ is the power spectrum of the spike train: $S_{yy}(f) = \lim_{T \rightarrow \infty} \frac{1}{T} \langle \tilde{y} \tilde{y}^* \rangle$, where $\tilde{y}(f)$ is the Fourier transform of the spike train. If and only if $x(t)$ and $y(t)$ are linearly scaled copies of each other, then $C_{xy}(f)=1$. If $x(t)$ and $y(t)$ are independent, then $C_{xy}(f)=0$; however, the reverse generally does not hold. Nonlinear effects and noise reduce the coherence. We calculated the spectral coherence in two independent ways: first, based on the numerical solution of the time-dependent Fokker-Planck equation, and second, based on direct numerical simulations with band-limited white noise. The time-dependent Fokker-Planck solution using the threshold integration scheme above yields a linear

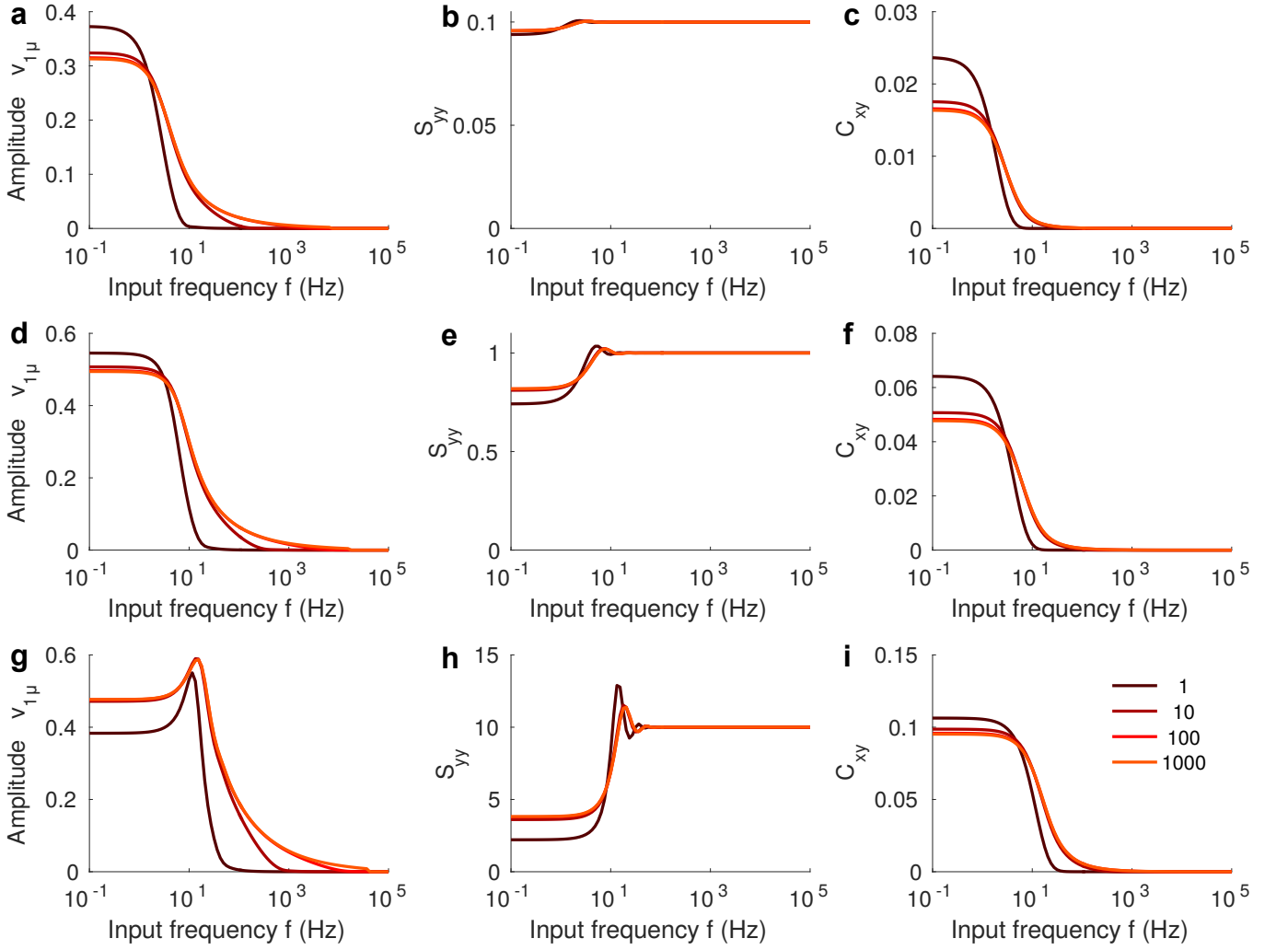


Figure 12. **Action potential onset rapidness r and ν_0 shape frequency-response, spike power spectra and spectral coherence:** **a)** Linear response for mean modulation of input current for $\nu_0 = 0.1$ Hz, **b)** Spike power spectra for different r for $\nu_0 = 0.1$ Hz. **c)** spectral coherence for different r for $\nu_0 = 0.1$ Hz. **d), e)** and **f)** same as **a**, **b** and **c** for $\nu_0 = 1$ Hz. At low rates, neurons are in the fluctuation-driven regime, therefore S_{yy} is flat. At high rates (mean-driven regime), the response amplitude $\nu_{1\mu}$ has a resonance close to ν_0 (parameters: $\nu_0 = 10$ Hz, $\mu_1 = 0.01$, $\tau_m = 10$ ms, $\Delta V = 10^{-4}$, $V_{th} = 10^4 = -V_r$).

response approximation of $S_{xy}(f)$ directly from the linear response. Assuming weak modulations of the input, the stationary power spectrum of the spike train is sufficient and can be obtained using again threshold integration again [14]. The dependences of $S_{yy}(f)$, $S_{xy}(f)$ and $C_{xy}(f)$ on rapidness r and mean rate ν_0 are depicted in **Fig. 12**. At low rates, due to our balanced scaling (see Section IX), neurons are in the fluctuation driven regime, therefore, S_{yy} is flat. At high firing rates, corresponding to a more mean-driven regime, the response amplitude $\nu_{1\mu}$ has a resonance close to ν_0 .

The Fokker-Planck ansatz and direct numerical simulations with band-limited white noise are in excellent agreement (**Fig. 13**).

The mutual information rate scales approximately logarithmically with r . For large rapidness, the mutual information rate saturates, with the saturation level is determined by the band limit of the incoming white noise (**Fig. 14**).

Dependence of mutual information rate on spike rapidness We know $S_{xy}(f)$ in both in the high-frequency limit from the analytical high-frequency response and the low-frequency limit because, for very low frequency input modulations ($f\tau_m \ll 1$), the spike rate follows the input adiabatically:

$$\lim_{f \rightarrow 0} S_{xy}(f) = \mu_1 \frac{\partial \nu_0}{\partial \mu} \quad (35)$$

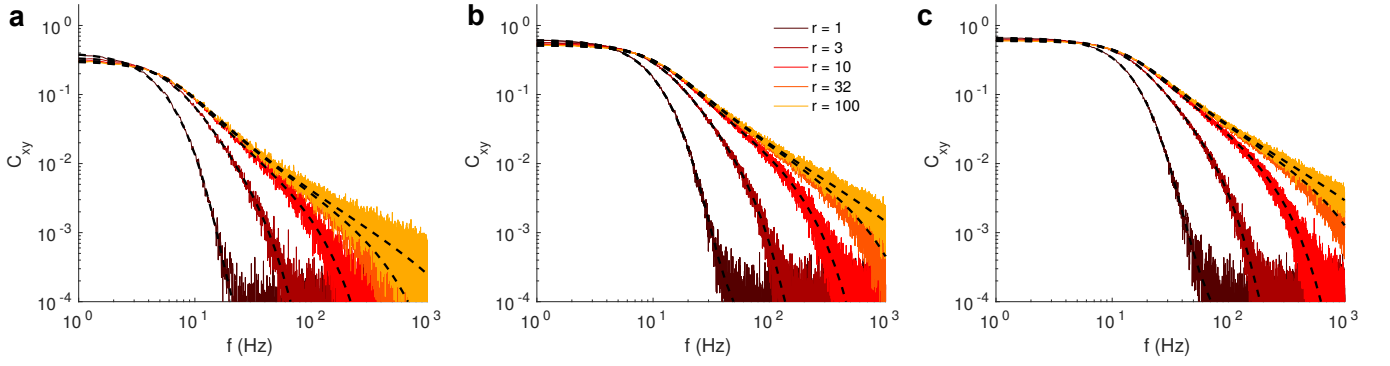


Figure 13. **Action potential onset rapidness r and ν_0 shape spectral coherence: (Fokker-Planck ansatz vs. direct numerical simulations).** a) $\nu_0 = 1$ Hz b) $\nu_0 = 5$ Hz c) $\nu_0 = 10$ Hz. C_{xy} normalized by input modulation μ_1^2 (parameters: $\mu_1 = 0.01$, $\tau_m = 10$ ms, $\Delta V = 10^{-3}$, $V_{th} = 10^3 = -V_r$)

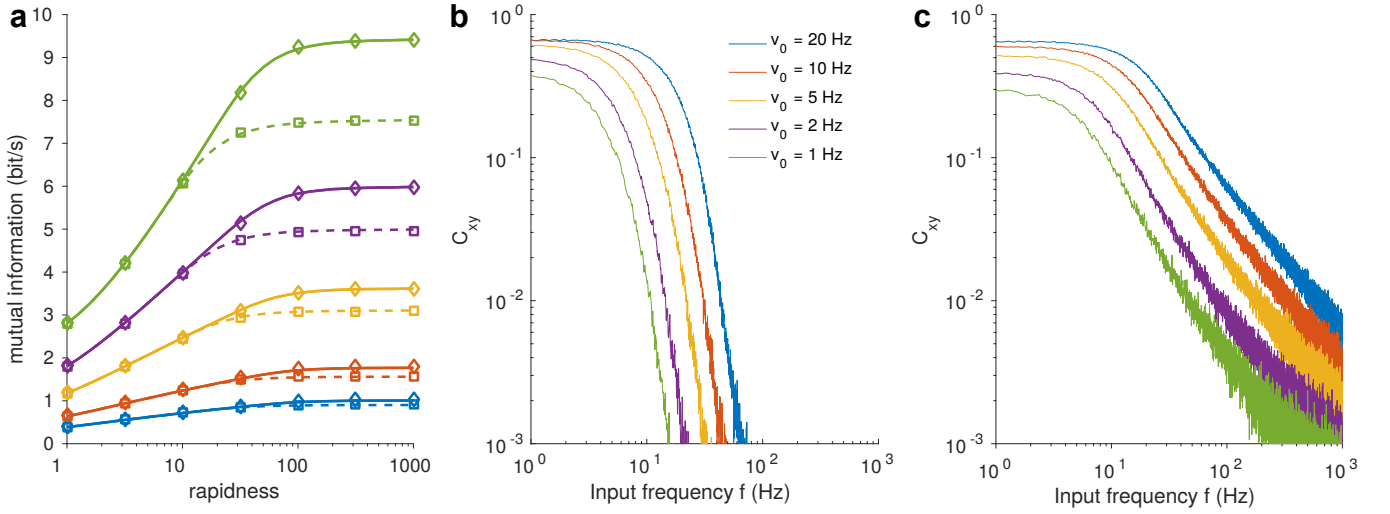


Figure 14. **Action potential onset rapidness r and ν_0 limit mutual information rate and spectral coherence:** a) Mutual information rate for two band limits of the incoming white noise: dashed lines for $f_{\text{bandlimit}} = 500$ Hz and full lines for $f_{\text{bandlimit}} = 2000$ Hz both from Fokker-Planck approach. Diamonds and squares are the corresponding direct numerical simulations with band-limited white noise input. b) Spectral coherence for different firing rates from direct numerical simulations $r = 1$. c) same as b) for $r = 1000$ (parameters: $\nu_0 = 10$ Hz, $\mu_1 = 0.01$, $\tau_m = 10$ ms, $\Delta V = 10^{-3}$, $V_{th} = 10^3 = -V_r$).

This is the slope of the $\nu_0 - \mu$ curve depicted in **Fig. 7**. For renewal processes, S_{yy} is given, for high input frequencies, by the firing rate

$$\lim_{f \rightarrow \infty} S_{yy}(f) = \nu_0 \quad (36)$$

and for low input frequencies

$$\lim_{f \rightarrow 0} S_{yy}(f) = \nu_0 c v^2, \quad (37)$$

where $c v$ is the coefficient of variation of the interspike intervals T : $c v = \sqrt{\langle T^2 \rangle - \langle T \rangle^2} / \langle T \rangle$. For intermediate frequencies at intermediate to high onset rapidness, an approximation of the frequency-response of the rapid theta neuron can be obtained from the analytical high-frequency response for high rapidness (Eq. 25). The reason is that for intermediate input frequencies, the glue point V_G acts like a hard threshold, if the time from threshold V_U to spike is smaller than the inverse frequency. Plugging these estimates into Eq. 33, we obtain an analytical approximation of

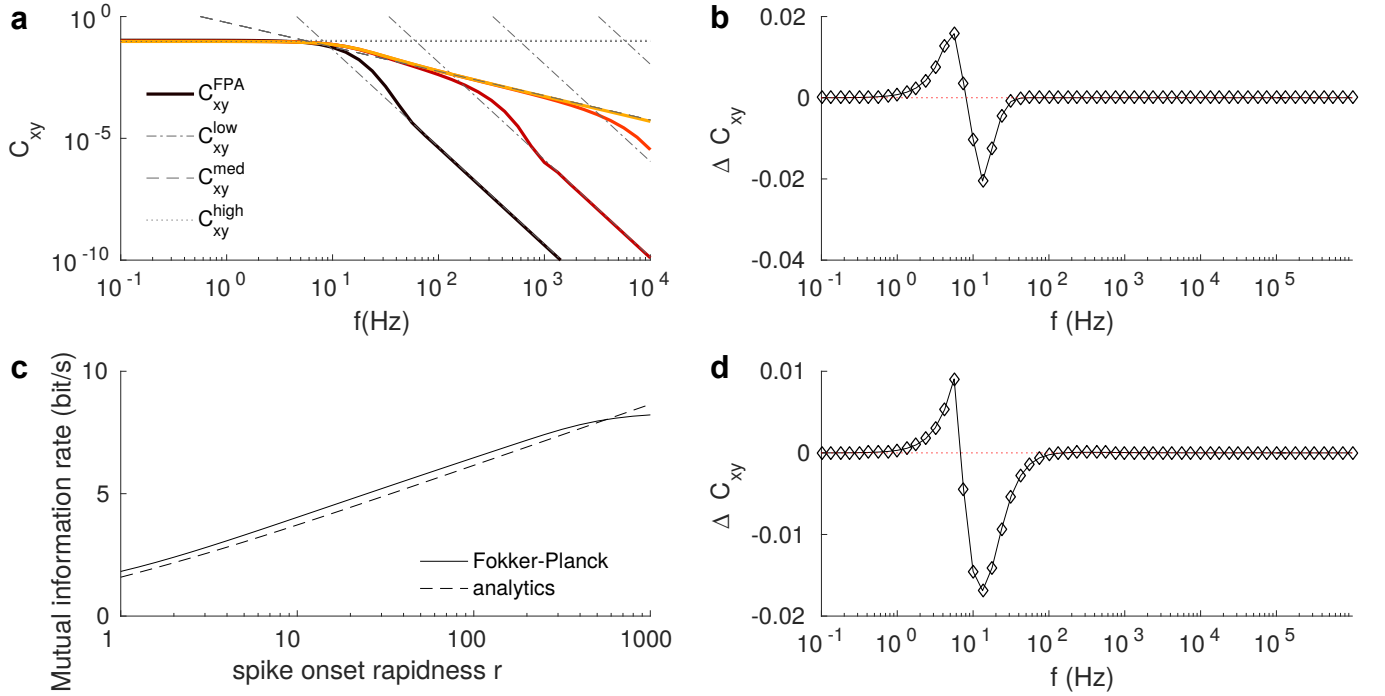


Figure 15. **Analytical estimate of the mutual information rate and spectral coherence explains logarithmic scaling with action potential onset rapidness r** $R_{\text{ib}}(r) \propto \log(r)$: **a)** Spectral coherence obtained from Fokker-Planck ansatz vs analytical estimates for low mid and high frequency regime. Dashed line: high-rapidness scaling, dash-dotted line: high-frequency scaling, dotted line: low frequency estimate. **b)** Deviation between Fokker-Planck ansatz and analytical estimates for $r = 1$. **c)** comparison of mutual information rates obtained from Fokker-Planck ansatz vs. analytical estimate. **d)** Same as **b)** for $r = 1000$ (parameters: $\nu_0 = 10$ Hz, $\mu_1 = 0.01$, $\tau_m = 10$ ms, $\Delta V = 10^{-3}$, $V_{\text{th}} = 10^3 = -V_r$).

the spectral coherence for different frequency regimes:

$$C_{xy}^{\text{low}}(f) = \frac{|S_{xy}(f)|^2}{|S_{xx}(f)||S_{yy}(f)|} = \frac{|\mu_1 \frac{\partial \nu_0}{\partial \mu}|^2}{\sigma^2 \nu_0 c v^2} = \mu_1^2 \left(\frac{\partial \nu_0}{\partial \mu} \right)^2 \quad (38)$$

$$C_{xy}^{\text{mid}}(f) = \frac{|S_{xy}(f)|^2}{|S_{xx}(f)||S_{yy}(f)|} = \frac{|\frac{\nu_0 \mu_1}{\sqrt{i\omega \tau_m}}|^2 \sigma^4}{\sigma^2 \nu_0} = \frac{\nu_0 \mu_1^2 \sigma^2}{2\pi f \tau_m} \quad (39)$$

$$C_{xy}^{\text{high}}(f) = \frac{|S_{xy}(f)|^2}{|S_{xx}(f)||S_{yy}(f)|} = \frac{|\frac{\nu_0 \mu_1 r(r+1)}{(i\omega \tau_m)^2}|^2 \sigma^4}{\sigma^2 \nu_0} = \frac{\nu_0 \mu_1^2 r^2 (r+1)^2 \sigma^2}{(2\pi f \tau_m)^4} \quad (40)$$

These approximations are precise in their respective limits of low and high frequencies. However, in the intermediate transition regimes, deviations occur (**Fig. 15**).

For intermediate mean firing rates, the analytical low coherence approximation overestimates the coherence, while at the transition zone, the analytical intermediate approximation underestimates the coherence. These two errors approximately compensate each other (**Fig. 15b**). At low rates, the overestimation in the analytical low coherence regime is smaller; therefore, the analytically obtained approach underestimates the mutual information rate (**Fig. 16**).

For high firing rates, the analytical coherence approximation strongly underestimates the coherence, therefore the analytical approach overestimates the mutual information rate (**Fig. 17**). The estimation errors are largely insensitive to rapidness, therefore the slopes are still in good agreement with the Fokker-Planck approach.

The transition point between the low and intermediate regimes is obtained by calculating the crossings between $C_{xy}^{\text{low}}(f)$ and $C_{xy}^{\text{mid}}(f)$ as follows:

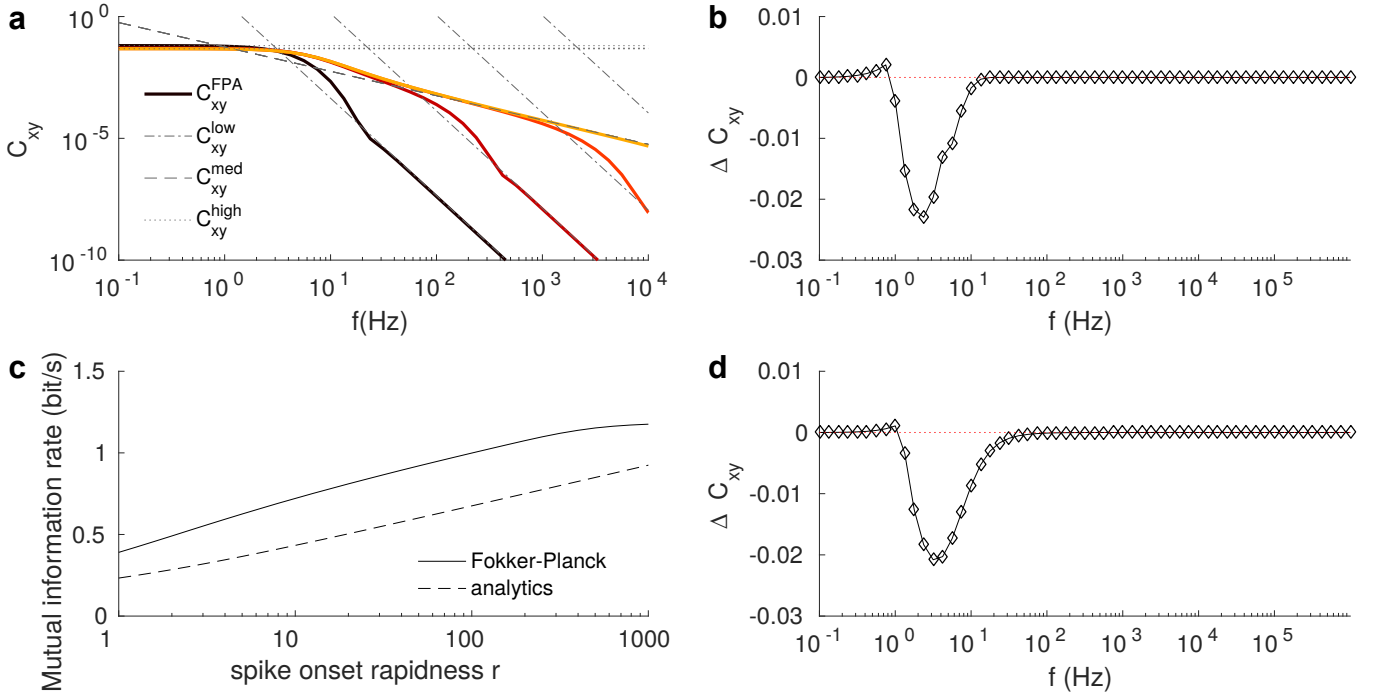


Figure 16. **Analytical estimate of the mutual information rate and spectral coherence with action potential onset rapidness r for low firing rate: $\nu_0 = 1$ (parameters same as Fig. 16).**

$$f^{\text{lm}}(r, \nu_0) = \frac{\nu_0^2 \sigma^4 c v^2}{\left(\frac{\partial \nu_0}{\partial \mu}\right)^2 \tau_m} \quad (41)$$

For weak noise input, we obtain from Eq. 10 that $\frac{\partial \nu_0}{\partial \mu} = \frac{1}{\pi \tau_m} \sqrt{\frac{r}{2r(r+1)I_{\text{ext}}}}$. The same is done for the second crossing with $C_{xy}^{\text{mid}}(f)$ and $C_{xy}^{\text{high}}(f)$:

$$f^{\text{mh}}(r, \nu_0) = \left[r(r+1) \sqrt{\nu_0 \tau_m} \right]^{2/3} \quad (42)$$

To obtain an analytical approximation of the mutual information rate, we stitched together analytical high-, middle-, and low-frequency approximations at the transition points. Plugging these into Eq. 32 gives us:

$$\begin{aligned} R_{\text{lb}} &= R_{\text{lb}} + R_{\text{lb}} + R_{\text{lb}} \\ &\approx - \int_0^{f_{\text{lm}}} df \log_2 (1 - C_{xy}^{\text{low}}(f)) - \int_{f_{\text{lm}}}^{f_{\text{mh}}} df \log_2 (1 - C_{xy}^{\text{mid}}(f)) - \int_{f_{\text{mh}}}^{f_{\text{cutoff}}} df \log_2 (1 - C_{xy}^{\text{high}}(f)) \end{aligned} \quad (43)$$

Only the contribution of the intermediate frequency term changes strongly as a function of rapidness in the relevant parameter regime. To obtain a simple analytical approximation for the dependence on rapidness, we need to evaluate

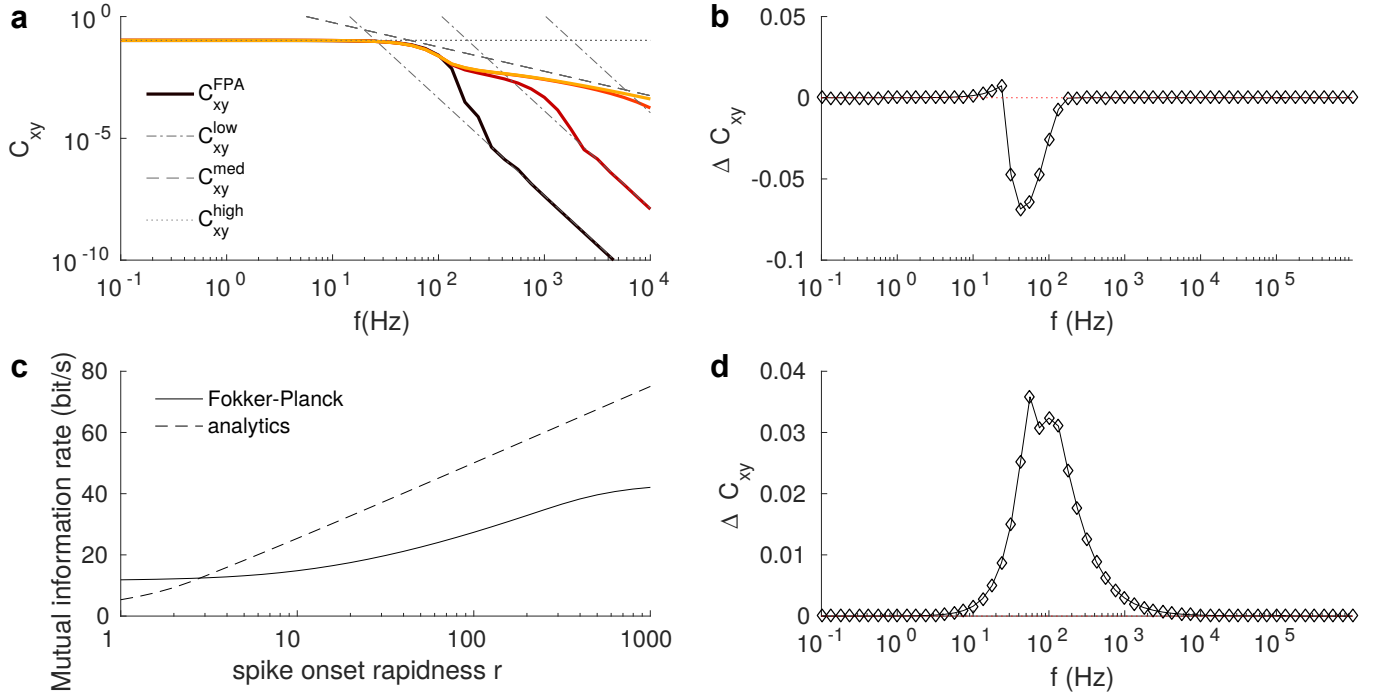


Figure 17. Analytical estimate of the mutual information rate and spectral coherence for different values of action potential onset rapidness r for high firing rate ($\nu_0 = 100$, other parameters same as Fig. 16).

only the second integral.

$$\begin{aligned}
 R_{1b} &\approx - \int_{f_{1m}}^{f_{mh}} df \log_2 (1 - C_{xy}^{\text{mid}}(f)) \\
 &= - \int_{f_{1m}}^{f_{mh}} df \log_2 \left(1 - \frac{c_1}{f} \right) \\
 &= \left[c_1 \log_2(f - c_1) - f \log_2 \left(1 - \frac{c_1}{f} \right) \right]_{f_{1m}}^{f_{mh}} \\
 &= c_1 \log_2(f_{mh} - c_1) - f_{1m} \log_2(f_{1m}) + (f_{1m} - c_1) \log_2(f_{1m} - c_1) - f_{mh} \log_2 \left(1 - \frac{c_1}{f_{mh}} \right)
 \end{aligned} \tag{44}$$

As short-hand notation, we defined $c_1 = \frac{\nu_0 \mu_1^2 \sigma^2}{2\pi \tau_m}$. Only the first term changes strongly as a function of rapidness, therefore

$$\begin{aligned}
R_{\text{lb}}(r) &\approx c_1 \log_2(f_{\text{mh}} - c_1) + \text{const} \\
&= c_1 \log_2 \left(\left[r(r+1) \sqrt{\nu_0 \tau_m} \right]^{2/3} - c_1 \right) + \text{const} \\
&\stackrel{r \gg c_1}{\approx} c_1 \log_2 \left(\left[r(r+1) \sqrt{\nu_0 \tau_m} \right]^{2/3} \right) + \text{const} \\
&= c_1 \frac{2}{3} \log_2 \left(r(r+1) \sqrt{\nu_0 \tau_m} \right) + \text{const} \\
&= c_1 \frac{2}{3} \log_2 (r(r+1)) + \text{const} \\
&\stackrel{r \gg 1}{\approx} c_1 \frac{4}{3} \log_2 (r) + \text{const} \\
&= \frac{2\nu_0 \mu_1^2 \sigma^2}{3\pi \tau_m} \log_2 (r) + \text{const}
\end{aligned} \tag{45}$$

We conclude that the mutual information rate scales approximately logarithmically with action potential onset rapidness for sufficiently large rapidness, weak input, and high band limit. Where does the logarithmic scaling of the mutual information rate with rapidness arise from? The reason is that the rapidness determines the cutoff frequency, up to which the rapid theta neuron transmits information approximately like a hard-threshold neuron (e.g., a leaky integrate-and-fire neuron). Contributions from frequencies beyond this cutoff are negligible to the first order. As a hard threshold always causes an asymptotic linear response $\propto 1/\sqrt{f}$, which becomes proportional to $1/f$ in the squared coherence, the integral that yields the lower bound of the mutual information (Eq. 32) always scales approximately proportional to $\log(f_{\text{cutoff}})$. Therefore $R_{\text{lb}}(r) \propto \log(r)$. This conclusion is not restricted to the rapid theta model; a similar line of argumentation holds also, e.g., for the exponential integrate-and-fire model and the rapid τ model [16, 20]. For the exponential integrate-and-fire neuron model, the mutual information rate also scales approximately logarithmically with the action potential onset rapidness parameter $1/\Delta_T$ despite the different asymptotic linear response, which scales $\hat{\nu}_\mu \propto \frac{1}{f}$ [16]. In the case of the rapid τ model, the same holds, despite the asymptotic linear response, which scales $\hat{\nu}_\mu \propto \frac{1}{\sqrt{f}} \exp(\frac{\omega}{r})$ [20].

VII. PHASE REPRESENTATION OF THE RAPID THETA NEURON

A phase representation of the rapid theta neuron model, similar to the classical theta neuron model, is obtained with the transformation $\tan \frac{\theta}{2} = V - V_G$ and $\theta \in [-\pi, \pi)$, yielding

$$\tau_m \frac{d\theta}{dt} = \begin{cases} \frac{r+1}{2r} (1 - \cos \theta) + (I(t) - I_T)(1 + \cos \theta) & \theta \leq 0 \\ \frac{r(r+1)}{2} (1 - \cos \theta) + (I(t) - I_T)(1 + \cos \theta) & \theta > 0. \end{cases} \tag{46}$$

For $r = 1$, the theta neuron model [2] is recovered.

The exact solutions of the rapid theta neuron model for constant positive external currents and δ pulse coupling allow us to derive a phase representation with constant phase velocity. This phase representation is convenient both for efficient, numerically exact, event-based simulation and also for analytical tractability.

The solution of the governing differential equation in the dimensionless voltage representation (4) for constant input

currents $I(t) \equiv I_T + I$ is

$$\begin{aligned} \frac{1}{I} \frac{dV}{1 + \left(\frac{V - V_G}{\sqrt{I/a_{S,U}}} \right)^2} &= \frac{1}{\tau_m} dt \\ \frac{1}{I} \sqrt{I/a_{S,U}} \left[\arctan \left(\frac{V - V_G}{\sqrt{I/a_{S,U}}} \right) \right]_{V_1}^{V_2} &= \frac{t_2 - t_1}{\tau_m} \\ \arctan \left(\frac{V_2 - V_G}{\sqrt{I/a_{S,U}}} \right) &= \arctan \left(\frac{V_1 - V_G}{\sqrt{I/a_{S,U}}} \right) + \sqrt{I/a_{S,U}} \frac{t_2 - t_1}{\tau_m}. \end{aligned} \quad (47)$$

This equation represents the solution for both branches of Eq. (4), separated by V_G as before. For the subthreshold part ($V \leq V_G$), the curvature is $a_S = \frac{r+1}{2r}$, and for the suprathreshold part ($V > V_G$), the curvature is $a_U = \frac{r(r+1)}{2}$. In the phase representation with phase $\phi \in [-\pi, \pi)$ and constant phase velocity, the phase evolution is given by

$$\phi_2 = \phi_1 + \omega \frac{t_2 - t_1}{\tau_m}. \quad (48)$$

Identifying Eq. (47) and (48) enables us to derive the constant phase velocity ω and the gluing point ϕ_G to define the transformation between the two representations

$$\frac{\phi - \phi_G}{\omega} = \arctan \left(\frac{V - V_G}{\sqrt{I/a_{S,U}}} \right) \frac{1}{\sqrt{I/a_{S,U}}}. \quad (49)$$

During one complete cycle, the time T_S spent in the subthreshold part ($V_2 = V_G$ and $V_1 \rightarrow -\infty$) and the time T_U spent in the suprathreshold part ($V_2 \rightarrow \infty$ and $V_1 \rightarrow V_G$) are obtained from Eq. (47):

$$T_S = \frac{\pi \tau_m}{\sqrt{2I(r+1)/r}} \quad \text{and} \quad T_U = \frac{\pi \tau_m}{\sqrt{2I(r+1)r}}.$$

The time spent in the subthreshold part is thus $T_S/T_U = r$ times as long as that in the suprathreshold part. The total cycle length, or unperturbed interspike interval, is

$$\begin{aligned} T^{\text{free}} &= (r+1)T_U \\ &= \frac{\pi \tau_m}{\sqrt{I}} \sqrt{\frac{r+1}{2r}}. \end{aligned} \quad (50)$$

Its inverse gives the firing rate for constant external input.

The constant phase velocity is then

$$\begin{aligned} \omega &= \frac{2\pi}{T^{\text{free}}} \\ &= \frac{2\sqrt{I}}{\tau_m} \sqrt{\frac{2r}{r+1}} = \frac{2}{\tau_m} \sqrt{I/a_S}. \end{aligned} \quad (51)$$

The phase corresponding to the gluing point is

$$\begin{aligned} \phi_G &= -\pi + \omega T_S \\ &= \pi \frac{r-1}{r+1}. \end{aligned} \quad (52)$$

The constant phase velocity (51) and the gluing point (52) define the transformation (49) between the voltage repre-

sensation and the phase representation:

$$\phi = \phi_G + \begin{cases} \frac{2}{a_S} \arctan\left(\frac{V-V_G}{\sqrt{I/a_S}}\right) & V \leq V_G \\ \frac{2}{ra_S} \arctan\left(r\frac{V-V_G}{\sqrt{I/a_S}}\right) & V > V_G \end{cases} \quad (53)$$

$$V = V_G + \begin{cases} \sqrt{I/a_S} \tan\left(a_S \frac{\phi-\phi_G}{2}\right) & \phi \leq \phi_G \\ \sqrt{I/r^2 a_S} \tan\left(ra_S \frac{\phi-\phi_G}{2}\right) & \phi > \phi_G. \end{cases} \quad (54)$$

This transformation between the two equivalent representations is now used to calculate the phase-transition curve $g(\phi)$ and the phase-response curve $Z(\phi)$. Receiving a δ pulse of strength J leads to a step like change of the neuron's voltage $V^+ = V^- + J$. If this change does not lead to a change from the subthreshold to the suprathreshold part or vice versa, the calculation of the phase-transition curve is straightforward. However, some care is needed if the δ pulse does lead to such a change.

An inhibitory pulse $J < 0$ can lead to a change from the suprathreshold to the subthreshold part. This happens if the neuron's phase is between ϕ_G and ϕ_- . The phase-transition curve for inhibitory δ pulses of strength J and constant external currents I with the effective coupling $C = J/\sqrt{I}$ and $\phi_- = \phi_G + \frac{2}{ra_S} \arctan(r(V_G - J - V_G)/\sqrt{I/a_S}) = \phi_G - \frac{2}{ra_S} \arctan(r\sqrt{a_S}C)$ is

$$g_-(\phi) = \phi_G + \begin{cases} \frac{2}{a_S} \arctan\left(\tan\left(a_S \frac{\phi-\phi_G}{2}\right) + \sqrt{a_S}C\right) & -\pi < \phi \leq \phi_G \\ \frac{2}{a_S} \arctan\left(\frac{1}{r} \tan\left(ra_S \frac{\phi-\phi_G}{2}\right) + \sqrt{a_S}C\right) & \phi_G < \phi < \phi_- \\ \frac{2}{ra_S} \arctan\left(\tan\left(ra_S \frac{\phi-\phi_G}{2}\right) + r\sqrt{a_S}C\right) & \phi_- \leq \phi < \pi. \end{cases} \quad (55)$$

For excitatory δ pulses of strength $J > 0$, the phase can change from the subthreshold to the suprathreshold part if the phase is between ϕ_+ and ϕ_G . The phase-transition curve for excitatory δ pulses of strength J and constant external currents I with the effective coupling $C = J/\sqrt{I}$ and $\phi_+ = \phi_G - \frac{2}{a_S} \arctan(\sqrt{a_S}C)$ (displayed in **Fig. 18**) is

$$g_+(\phi) = \phi_G + \begin{cases} \frac{2}{a_S} \arctan\left(\tan\left(a_S \frac{\phi-\phi_G}{2}\right) + \sqrt{a_S}C\right) & -\pi < \phi \leq \phi_+ \\ \frac{2}{ra_S} \arctan\left(r \tan\left(a_S \frac{\phi-\phi_G}{2}\right) + r\sqrt{a_S}C\right) & \phi_+ < \phi < \phi_G \\ \frac{2}{ra_S} \arctan\left(\tan\left(ra_S \frac{\phi-\phi_G}{2}\right) + r\sqrt{a_S}C\right) & \phi_G \leq \phi < \pi. \end{cases} \quad (56)$$

The phase-response curve is $Z_{\pm}(\phi) = g_{\pm}(\phi) - \phi$. Thus, the infinitesimal phase-response curve is the same for both excitatory and inhibitory pulses, since $\phi_{\pm} \rightarrow \phi_G$ for $C \rightarrow 0$:

$$Z(\phi) \stackrel{C \rightarrow 0}{\simeq} C \begin{cases} \frac{2\sqrt{a_S}}{a_S} \frac{1}{1+\tan\left(a_S \frac{\phi-\phi_G}{2}\right)^2} = \frac{1 + \cos(a_S(\phi - \phi_G))}{\sqrt{a_S}} & -\pi < \phi \leq \phi_G \\ \frac{2r\sqrt{a_S}}{ra_S} \frac{1}{1+\tan\left(ra_S \frac{\phi-\phi_G}{2}\right)^2} = \frac{1 + \cos(ra_S(\phi - \phi_G))}{\sqrt{a_S}} & \phi_G \leq \phi < \pi. \end{cases} \quad (57)$$

VIII. SINGLE SPIKE JACOBIAN OF THE RAPID THETA NEURON NETWORK

The analytical expression of the derivative of the evolution map, called the single spike Jacobian, is necessary for calculating the full Lyapunov spectrum with high precision. The single spike Jacobian describes the linear evolution of infinitesimal perturbations of the neuron's states and will be used to numerically calculate the Lyapunov spectra. Since infinitesimal perturbations are considered here, the spike-order in the networks is preserved, provided that there are no exactly synchronous spike events. Such exactly synchronous events generally should which generally should not occur in the asynchronous network states considered here. In a phase representation, the iterative map, which maps the state of the network at one spike time to the state at the next spike in the network, reads

$$\phi_i(t_{s+1}) = \phi_i(t_s) + \omega_i(t_{s+1} - t_s) + Z(\phi_i(t_s) + \omega_i(t_{s+1} - t_s))\delta_{i \in \text{post}(j^*)}, \quad (58)$$

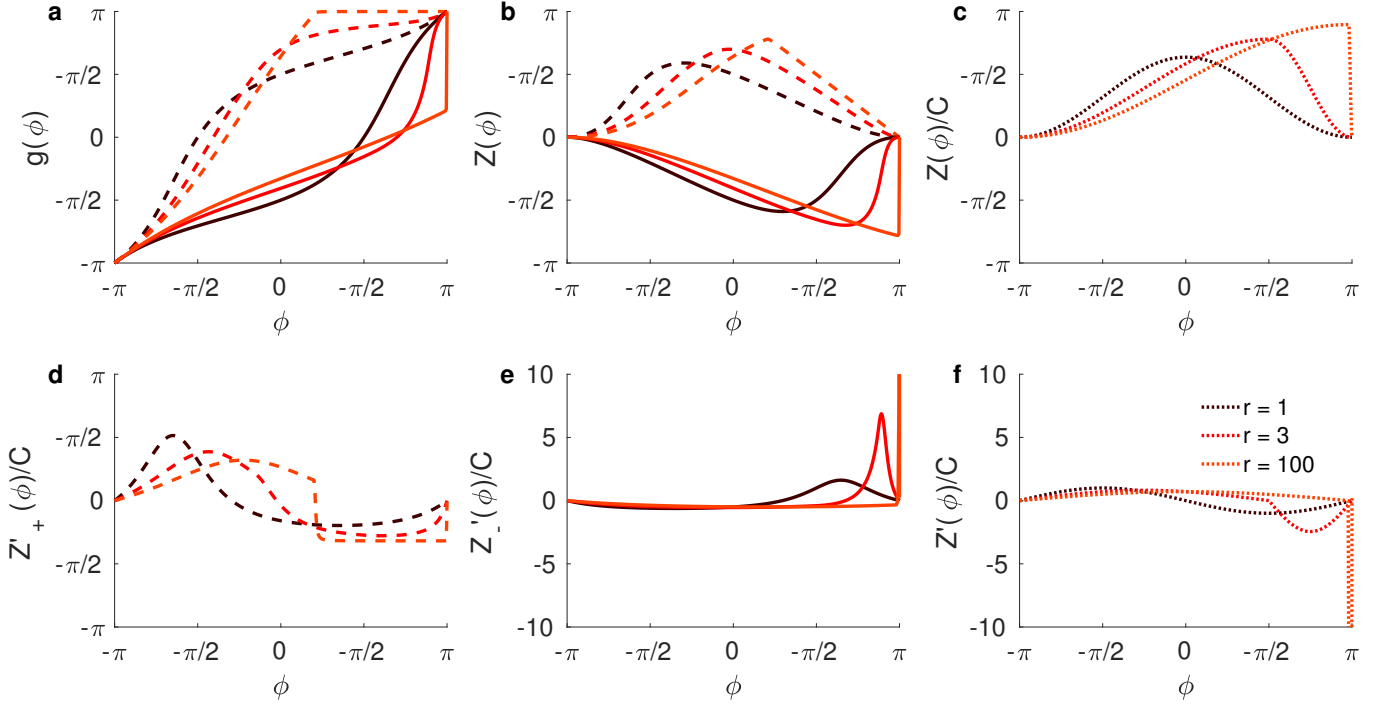


Figure 18. **Phase-transition curve (PTC), phase-response (PRC) and infinitesimal phase-response (iPRC) explain reduction of chaos for high AP onset rapidness r .** **a)** The phase-transition curve (PTC) $g(\phi)$ shown with inhibitory coupling $C = -1$ (full lines, Eq. (55)) and excitatory coupling $C = +1$ (dashed lines, Eq. (56)) for three values of spike onset rapidness $r = 1, 3, 100$. **b)** Same for phase response curve (PRC) $Z(\phi) = g(\phi) - \phi$. **c)** Same for infinitesimal PRC (Eq. (57)). **d)** Derivative of PRC for excitatory coupling. **e)** Derivative of PRC for inhibitory coupling. **f)** Derivative of derivative of infinitesimal phase response curve (Eq. (63)). Note that in the limit $r \rightarrow \infty$ the iPRC becomes monotonically increasing and its derivative is positive almost everywhere.

where $\delta_{i \in \text{post}(j^*)}$ is one if i is a postsynaptic neuron of the spiking neuron j^* and zero otherwise and $Z(\phi_i)$ is the phase-response curve.

Consequently, the single spike Jacobian reads

$$D_{ij}(t_s) = \frac{d\phi_i(t_{s+1})}{d\phi_j(t_s)} = \begin{cases} 1 + Z'(\phi_{i^*}(t_{s+1}^-)) & \text{for } i = j = i^* \\ -\frac{\omega_{i^*}}{\omega_{j^*}} Z'(\phi_{i^*}(t_{s+1}^-)) & \text{for } i = i^* \text{ and } j = j^* \\ \delta_{ij} & \text{otherwise,} \end{cases} \quad (59)$$

where j^* denotes the spiking neuron in the considered interval, firing at time t_{s+1} , $i^* \in \text{post}(j^*)$ are the spike receiving neurons and δ_{ij} is the Kronecker delta. The derivatives of the phase-response curves $Z'(\phi)$ are evaluated at the phases of the spike receiving neurons $\phi_{i^*}(t_{s+1}^-) = \phi_{i^*}(t_s) + \omega_{i^*}(t_{s+1} - t_s)$ just before spike reception. To investigate the collective dynamics of networks of rapid theta neurons, it is necessary to obtain the derivative $d(\phi_{i^*}(t_{s+1}^-)) = 1 + Z'(\phi_{i^*}(t_{s+1}^-))$ of the phase-transition curve for calculation of the single spike Jacobians. The derivative $d(\phi)$ in the case of inhibitory pulses is

$$d_-(\phi) = \begin{cases} \frac{\tan\left(\frac{a_S(\phi - \phi_G)}{2}\right)^2 + 1}{\left(\tan\left(\frac{a_S(\phi - \phi_G)}{2}\right) + \sqrt{a_S C}\right)^2 + 1} & -\pi < \phi \leq \phi_G \\ \frac{\tan\left(r a_S \frac{\phi - \phi_G}{2}\right)^2 + 1}{\left(\frac{1}{r} \tan\left(r a_S \frac{\phi - \phi_G}{2}\right) + \sqrt{a_S C}\right)^2 + 1} & \phi_G < \phi < \phi_- \\ \frac{\tan\left(r a_S \frac{\phi - \phi_G}{2}\right)^2 + 1}{\left(\tan\left(r a_S \frac{\phi - \phi_G}{2}\right) + r \sqrt{a_S C}\right)^2 + 1} & \phi_- \leq \phi < \pi. \end{cases} \quad (60)$$

In the voltage representation, the derivative $d(V)$ is useful for the analytical calculation of the mean Lyapunov

exponent in section XI:

$$d_-(V) = \begin{cases} \frac{r^2(V-V_G)^2 + \frac{I_0\sqrt{K}}{a_S}}{(V-V_G+C\sqrt{I})^2 + \frac{I_0\sqrt{K}}{a_S}} & V \leq V_G \\ \frac{r^2(V-V_G)^2 + \frac{I_0\sqrt{K}}{a_S}}{(V-V_G+C\sqrt{I})^2 + \frac{I_0\sqrt{K}}{a_S}} & V_G < V < V_- \\ \frac{r^2(V-V_G)^2 + \frac{I_0\sqrt{K}}{a_S}}{r^2(V-V_G+C\sqrt{I})^2 + \frac{I_0\sqrt{K}}{a_S}} & V_- \leq V. \end{cases} \quad (61)$$

The derivative of the phase-transition curve in the case of excitatory pulses is

$$d_+(\phi) = \begin{cases} \frac{\tan\left(a_S \frac{\phi-\phi_G}{2}\right)^2 + 1}{\left(\tan\left(a_S \frac{\phi-\phi_G}{2}\right) + \sqrt{a_S C}\right)^2 + 1} - 1 & -\pi < \phi \leq \phi_+ \\ \frac{\tan\left(a_S \frac{\phi-\phi_G}{2}\right)^2 + 1}{\left(r \tan\left(a_S \frac{\phi-\phi_G}{2}\right) + r\sqrt{a_S C}\right)^2 + 1} - 1 & \phi_+ < \phi < \phi_G \\ \frac{\tan\left(r a_S \frac{\phi-\phi_G}{2}\right)^2 + 1}{\left(\tan\left(r a_S \frac{\phi-\phi_G}{2}\right) + r\sqrt{a_S C}\right)^2 + 1} - 1 & \phi_G \leq \phi < \pi. \end{cases} \quad (62)$$

The derivative of the phase-response curve is $Z'_\pm(\phi) = d_\pm(\phi) - 1$ and the derivative of the infinitesimal phase-response curve is

$$Z'(\phi) \stackrel{C \rightarrow 0}{\simeq} -C \begin{cases} \sqrt{a_S} \sin(a_S(\phi - \phi_G)) & -\pi < \phi \leq \phi_G \\ r\sqrt{a_S} - \sin(r a_S(\phi - \phi_G)) & \phi_G \leq \phi < \pi. \end{cases} \quad (63)$$

The phase-transition curves (PTC, $g(\phi)$, Eqs. (55) and (56)), the phase response curves (PRC, $Z(\phi) = g(\phi) - \phi$), and the infinitesimal phase-response curves (iPRC, Eq. (57)) of the rapid theta neuron model are displayed in **Fig. 18**. The iPRC of the theta neuron ($r = 1$) is fully symmetric [2], whereas for increasing AP onset rapidness r the iPRC becomes more and more asymmetric. In the limit $r \rightarrow \infty$ it becomes monotonically increasing/decreasing and one might expect that this can qualitatively change the collective network dynamics.

IX. SETUP OF NETWORK AND EVENT-BASED SIMULATION

The pattern of action potentials in cortical tissue is asynchronous and irregular [31], despite the reliable response of single neurons [32]. This is commonly explained by a balance of excitatory and inhibitory synaptic currents [35], which cancels out large mean synaptic inputs. A dynamically self-organized balance can be achieved without the fine-tuning of synaptic coupling strength, if the connectivity is inhibition dominated [1]. The statistics of this state is described by a mean-field theory, which is largely independent of neuron model. We studied large sparse networks of N rapid theta neurons arranged on a directed Erdős–Rényi random graph of mean indegree K . All neurons $i = 1, \dots, N$ receive constant external currents I_{ext} and non-delayed δ -pulses from the presynaptic neurons $j \in \text{pre}(i)$. The external currents are chosen to obtain a certain average network firing rate $\bar{\nu}$ using a bisection method in purely inhibitory networks. In purely inhibitory networks, the non-zero coupling strengths are set to $J_{ij} = -J_0/\sqrt{K}$ and all neurons receive identical external currents. In two-population networks, the intra-population couplings are $J_{EE} = \frac{J_0}{\sqrt{K}}\eta\varepsilon$ and $J_{II} = -\frac{J_0}{\sqrt{K}}\sqrt{1-\varepsilon^2}$ for the excitatory (E) and inhibitory (I) population, respectively. The inter-population coupling strengths are $J_{IE} = \frac{J_0}{\sqrt{K}}\varepsilon$ and $J_{EI} = -\frac{J_0}{\sqrt{K}}\sqrt{1-\eta^2\varepsilon^2}$. At $\varepsilon = 0$, all excitatory neurons are completely passive. They only receive inputs from the inhibitory neurons but do not provide feedback. Increasing ε above zero activates the excitatory feedback loops in the network. The specific choice of coupling strengths preserves the temporal variance of the input currents $\sigma_I^2 = J_0^2\bar{\nu}$ in both purely inhibitory networks and two-population networks, as explained below. In mixed networks, the external currents are adapted using the two-dimensional Newton-Raphson root-finding method, to obtain the desired mean firing rate in the excitatory and inhibitory population.

Setup of balanced network with strong couplings and nonvanishing fluctuations. The coupling strengths in inhibitory and excitatory-inhibitory networks were chosen such that the magnitudes of the input current fluctuations are identical in all studied networks. Assuming that inputs from different presynaptic neurons are weakly correlated, the compound input spike train received by neuron i is modeled as a Poisson process with rate

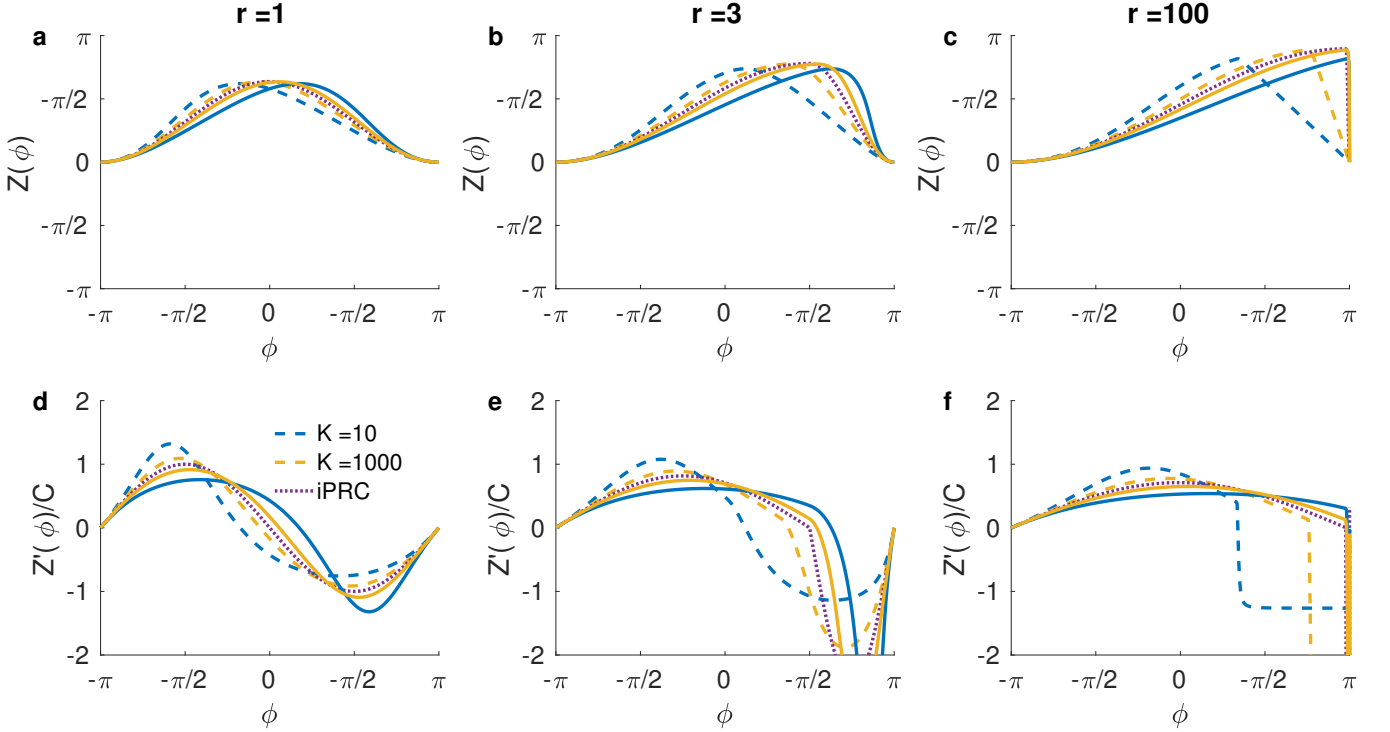


Figure 19. **Phase-response (PRC) and infinitesimal phase-response (iPRC) of the rapid theta neuron model for different effective coupling strengths.** **a)** The PRC is shown for different K corresponding to different coupling strengths $C = -\frac{J_0}{\sqrt{K}}\sqrt{\frac{\alpha s}{I}}$ for inhibitory (full lines Eq. (55)) and excitatory couplings (dashed lines, Eq. (56)) for AP onset rapidness $r = 1$. The infinitesimal PRC (Eq. (57)) is also displayed for comparison (dotted lines) **b)** Same as **a)** for AP onset rapidness $r = 3$ **c)** Same as **a)** for AP onset rapidness $r = 100$. **d)** Derivative of PRC normalized by C for $r = 1$. The derivative of the infinitesimal PRC is shown as dotted line (Eq. (63)). **e)** Same as **d)** for $r = 3$. **f)** Same as **d)** for $r = 100$ (parameters: $I_0 = 1, J_0 = 1$).

$\Omega_i = \sum_{j \in \text{pre}(i)} \nu_j \approx K\bar{\nu} \equiv \Omega$, where $\bar{\nu}$ is the network-averaged firing rate and K the average number of presynaptic neurons. For inhibitory networks, the nonzero coupling strengths were $J_{ij} = -\frac{J_0}{\sqrt{K}}$. Assuming that the compound input spike train is a Poisson process, the input current auto-correlation function is given by

$$\begin{aligned}
 C(\tau) &= \langle \delta I(t) \delta I(t + \tau) \rangle_t \\
 &\approx \left(\frac{J_0}{\sqrt{K}} \right)^2 \Omega \int \delta(t-s) \delta(t+\tau-s) ds \\
 &= \frac{J_0}{K} \Omega \delta(\tau) \\
 &\approx J_0^2 \bar{\nu} \delta(\tau)
 \end{aligned} \tag{64}$$

Thus, the fluctuations in the input currents are described as delta-correlated white noise of magnitude

$$\sigma^2 = J_0^2 \bar{\nu}. \tag{65}$$

Note that due to the scaling of the coupling strengths $J = -\frac{J_0}{\sqrt{K}}$ with the square root of the number of synapses K , the magnitude of the fluctuations σ^2 is independent of the number of synapses. Therefore, the input fluctuations do not vanish in the thermodynamic limit, and the balanced state in sparse networks emerges robustly [1].

The existence of a balanced state fixed point in the large K -limit can be derived from the equation of the network-averaged mean current

$$\bar{I} \approx \sqrt{K}(I_I - J_0 \bar{\nu}).$$

In the large K -limit, self-consistency requires the balance of excitation and inhibition to be $I_I = J_0\bar{\nu}$: If $\lim_{K \rightarrow \infty}(I_I - J_0\bar{\nu}) > 0$, the mean current \bar{I} would diverge to ∞ and the neurons would fire at their maximal rate. This resulting strong inhibition would break the inequality, leading to a contradiction. If $\lim_{K \rightarrow \infty}(I_I - J_0\bar{\nu}) < 0$, the mean current \bar{I} would diverge to $-\infty$, and the neurons would be silent. This resulting lack of inhibition again breaks the inequality. The large K -limit is self-consistent if

$$\lim_{K \rightarrow \infty} (I_I - J_0\bar{\nu}) = \mathcal{O}\left(\frac{1}{\sqrt{K}}\right),$$

such that the excitatory external drive and mean recurrent inhibitory current cancel out each other. Note that since $I_I - J_0\bar{\nu} = \mathcal{O}(1/\sqrt{K})$, the network mean current has a finite large K -limit. The average firing rate in units of the membrane time constant τ_m is approximately given by the balance equation (also called the van Vreeswijk equation):

$$\bar{\nu} = \frac{I_I}{J_0} + \mathcal{O}\left(\frac{1}{\sqrt{K}}\right). \quad (66)$$

Setup of mixed network The input current autocorrelations in balanced networks with excitatory (E) and inhibitory (I) populations are derived analogously to Eq. 64 and also display delta-correlated white noise. Assuming the same average indegree K from each population, the magnitudes of the input fluctuations are

$$\begin{aligned} \sigma_I^2 &= J_{II}^2\bar{\nu}_I + J_{IE}^2\bar{\nu}_E \\ \sigma_E^2 &= J_{EE}^2\bar{\nu}_E + J_{EI}^2\bar{\nu}_I. \end{aligned}$$

Choosing the coupling weights to be

$$\mathbf{J} = \begin{pmatrix} J_{EE} & -J_{EI} \\ J_{IE} & -J_{II} \end{pmatrix} = \frac{J_0}{\sqrt{K}} \begin{pmatrix} \eta\varepsilon & -\sqrt{1 - (\eta\varepsilon)^2} \\ \varepsilon & -\sqrt{1 - \varepsilon^2} \end{pmatrix}, \quad (67)$$

and setting the average firing rates in both populations identical $\bar{\nu}_E = \bar{\nu}_I \equiv \bar{\nu}$ leads to

$$\sigma_E^2 = \sigma_I^2 \equiv \sigma^2 = J_0^2\bar{\nu}.$$

Thus, the magnitude of fluctuations is identical in all networks considered, independent of the excitatory feedback loop activation ε . Accordingly, the statistical characteristics of the balanced state are preserved when activating the excitatory loops. However, the dynamical features of the collective activity, change upon activation of the excitatory loops. Increasing the excitatory coupling enhances chaoticity in the network dynamics. It is important to note that the balanced state arises in an extended portion of the parameters space in mixed networks. This region is constrained by the following inequalities, which can be derived by self-consistency arguments similar to those used for the purely inhibitory network:

$$\frac{J_{EE}}{J_{EI}} < \frac{J_{IE}}{J_{II}} < \min\left\{1, \frac{\bar{\nu}_I}{\bar{\nu}_E}\right\} \text{ and } \frac{J_{EE}}{J_{IE}} < \frac{J_{EI}}{J_{II}} < \frac{E_0}{I_0}. \quad (68)$$

The particular parametrization with η and ε is used to keep the input statistics fixed.

All simulations were run event-based, following Ref. [3], where an exact map is iterated from spike to spike in the ϕ -representation of the rapid theta neuron model with homogeneous coupling strengths and homogeneous external currents for all neurons in each population. The next spike time in each population is obtained by inverting Eq. 48

$$t_s = t_{s-1} + \min_i \left\{ \frac{\pi - \phi_i(t_{s-1})}{\omega} \right\}. \quad (69)$$

The phase map $f(\vec{\phi}(t_{s-1})) = \vec{\phi}(t_s)$, iterating all neuron's phases between two successive spike events t_{s-1} and t_s in the network, is then the concatenation of Eq. 48 and the phase transition curve (Eq. 55 and Eq. 56)

$$f(\phi_i(t_{s-1})) = \begin{cases} \phi_i(t_{s-1}) + \omega(t_s - t_{s-1}) & \text{if } i \notin \text{post}(j^*) \\ g(\phi_i(t_{s-1}) + \omega(t_s - t_{s-1})) & \text{if } i \in \text{post}(j^*), \end{cases} \quad (70)$$

where $\text{post}(j^*)$ denotes the set of neurons postsynaptic to the spiking neuron j^* in the considered interval.

Eq. 70 is used for all network simulations in an iterative event-based procedure [3]. At the beginning of an iteration the next spike time in the network is calculated with Eq. (69). Then all neuron's phases are evolved until the next spike time using Eq. (70). Since the external currents are identical for all neurons in each population, it is sufficient to search for the neuron with the largest phase and then calculate the corresponding next spike time.

The average number of spikes per second of simulation time gives the firing rate in hertz. We used the interspike intervals T_i between subsequent spike times to calculate the coefficients of variation, $\text{cv}_i = \sqrt{\langle T_i^2 \rangle - \langle T_i \rangle^2} / \langle T_i \rangle$, where $\langle \dots \rangle$ denotes the temporal average. The neurons' firing rate and coefficient of variation distributions are shown in **Fig. 2** of the main manuscript.

X. CONVERGENCE OF THE LYAPUNOV SPECTRA

The single spike Jacobians Eq. 59 is evaluated using Eq. 60 and Eq. 62 with the exact phases of the neurons before spike reception, t . These were used to numerically calculate all Lyapunov exponents with the standard procedure [4]. Following a warmup of the network dynamics of typically 100 spikes per neuron on average, we started with a random N -dimensional orthonormal system that was evolved in each iteration using the single spike Jacobian. Subsequently, after a short warmup of the orthonormal system of about one spike per neuron, these norms were used to calculate the N Lyapunov exponents, $\lambda_i = \lim_{p \rightarrow \infty} \frac{1}{t_p} \sum_{s=1}^p \log g_i(t_s)$. The evolved vectors were reorthonormalized every $\mathcal{O}(N/K)$ network spikes, yielding the norms of the orthogonalized vectors $g_i(t_s)$ and the orthonormal system to be used in the following iterations.

All calculations were performed using custom code written in Julia and C++ with double precision. The GNU Scientific Library (GSL) was used for the random number generator (Mersenne-Twister), the Automatically Tuned Linear Algebra Software (ATLAS) for matrix multiplications in the Gram-Schmidt procedure and the Message Passing Interface (MPI) for the parallel implementation of the simulations. The sparseness of the networks was used for efficient storage of the coupling matrices, the updates of the postsynaptic neurons, and the matrix multiplications of the orthonormal system with the sparse single spike Jacobians. For very large networks ($N > 10^6$), the topology was not stored as a sparse matrix but generated on the fly during the simulation using the index of the spiking neuron as a seed for the random number generator used to generate the indices of the postsynaptic neurons [33]. For the reorthonormalization, we chose a parallel recursive blocked version of the Gram-Schmidt procedure [5] in our C++ implementation and the default LAPACK (Linear Algebra PACKage) routines for our Julia implementation which is using Householder reflections.

Note that the non-converged Lyapunov exponents generated during the transient are meaningless, as they neither reflect the local nor finite-time Lyapunov exponents. The converged Lyapunov exponents capture the network dynamics on the (chaotic) attractor. **Fig. 20a** displays the convergence towards the full Lyapunov spectrum on a logarithmic time scale. To ensure robustness, this calculation was repeated for 10 different initial phases **Fig. 20b** shows the results of ten such runs for six representative Lyapunov exponents (gray lines), together with their averages $\lambda_i = \frac{1}{10} \sum_{n=1}^{10} \lambda_{i,n}$ (solid color lines) and confidence intervals (dotted color lines) of the double standard error $2\Delta\lambda_i = 2\sqrt{\frac{1}{10} \sum_{n=1}^{10} (\lambda_{i,n} - \lambda_i)^2}$. The Lyapunov spectrum was independent of the initial phases, and in the limit of large networks, independent of network realizations. Generally, all calculations of the Lyapunov spectra were repeated ten times with different initial phases and network realizations. Numerical errors were usually smaller than the symbol sizes in the presented figures in the main manuscript.

Fig. 22 shows the double standard error of Lyapunov exponents, dynamical entropy rate and attractor dimension in random inhibitory networks across 10 trials. **Fig. 23** shows the same for mixed networks. We identified two main contributions to the variability of numerically calculated Lyapunov spectra. Firstly, variability arises the fact that Lyapunov spectra are asymptotic properties estimated from finite-time calculations. Secondly variability arising from the quenched disorder in different random network topologies. The first contribution is expected to vanish in the limit of infinitely long simulations for ergodic systems. The second contribution is expected to vanish in the limit of large network size due to self-averaging. Therefore, the Lyapunov spectrum of one realization of a large network is representative for the whole ensemble. Hence, averaging over many network realizations is unnecessary in large networks.

To validate our results, we applied three independent checks of our semi-analytic numerically exact calculation of Lyapunov spectra. First, the largest Lyapunov exponent can be calculated numerically by measuring the exponential rate of divergence or convergence of nearby trajectories, as described in [4, 34]. Secondly, in autonomous systems that are not at a fixed point, there is always a neutral Lyapunov vector in the direction of the flow, which has a zero

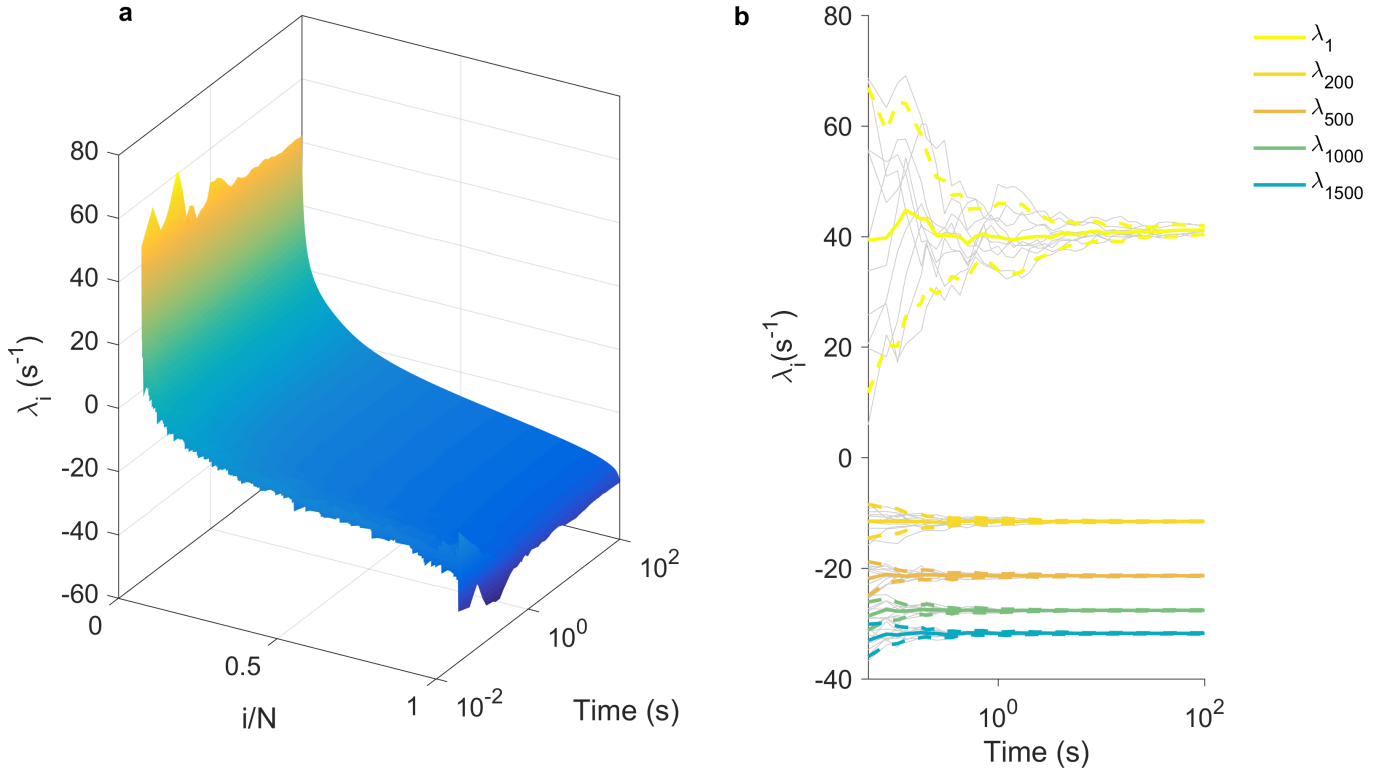


Figure 20. **Convergence of Lyapunov spectra over time in inhibitory networks with small AP rapidness ($r=3$).** (logarithmic time scale) **a**) Convergence of Lyapunov spectrum for one initial condition, **b**) gray lines: some Lyapunov exponents for ten different network realizations, solid color lines: averages, dotted color lines: averages \pm double standard errors (parameters: $N = 2000$, $\bar{\nu} = 1$ Hz, $K = 100$, $J_0 = 1$, $\tau_m = 10$ ms).

corresponding Lyapunov exponent, as the system can be shifted in time. Thirdly, random matrix theory allows for the calculation of the mean Lyapunov exponent, as shown in the next paragraph. All checks confirmed the results obtained from our implementation of the semi-analytic calculation of the full Lyapunov spectrum, validating the accuracy of our approach.

XI. RANDOM MATRIX THEORY OF THE MEAN LYAPUNOV EXPONENT

Using the single spike Jacobian (Eq. 59), we derived a random matrix approximation for the mean Lyapunov exponent, $\bar{\lambda} = \frac{1}{N} \sum_{i=1}^N \lambda_i$. The mean Lyapunov exponent describes the rate of phase space volume compression, which is captured by the determinant of the long-term Jacobian $\mathbf{T} = \mathbf{D}(t_s) \cdots \mathbf{D}(0)$:

$$\begin{aligned} \bar{\lambda} &= \frac{1}{N} \lim_{s \rightarrow \infty} \frac{1}{t_s} \ln(\det \mathbf{T}) \\ &= \frac{1}{N} \lim_{s \rightarrow \infty} \frac{1}{t_s} \sum_{p=1}^s \ln(\det \mathbf{D}(t_p)). \end{aligned} \quad (71)$$

The random matrix approximation is obtained by assuming that the single spike Jacobians to be random matrices of the form Eq. 59, with independent and identically distributed random elements that are obtained from the function $d(V)$, (Eq. (61)). The probability distribution of these random elements is determined by the stationary membrane potential distribution $P(V)$ in the network.

For inhibitory networks, the determinants of the random matrices can be approximated by $\det \mathbf{D} = \prod_{i^*} d_{i^*} \approx d(V)^K$, since on average there are K diagonal elements d_{i^*} , one for each postsynaptic neuron. We assume homogeneous coupling strengths $J_{ij} \equiv -J_0$ between connected neurons and identical external currents $I_i^{\text{ext}} \equiv I_0$ for all neurons. The number of network spike events per second is given by $\lim_{s \rightarrow \infty} \frac{1}{t_s} \sum_{p=1}^s 1 = N\bar{\nu}$. Thus, in the random matrix

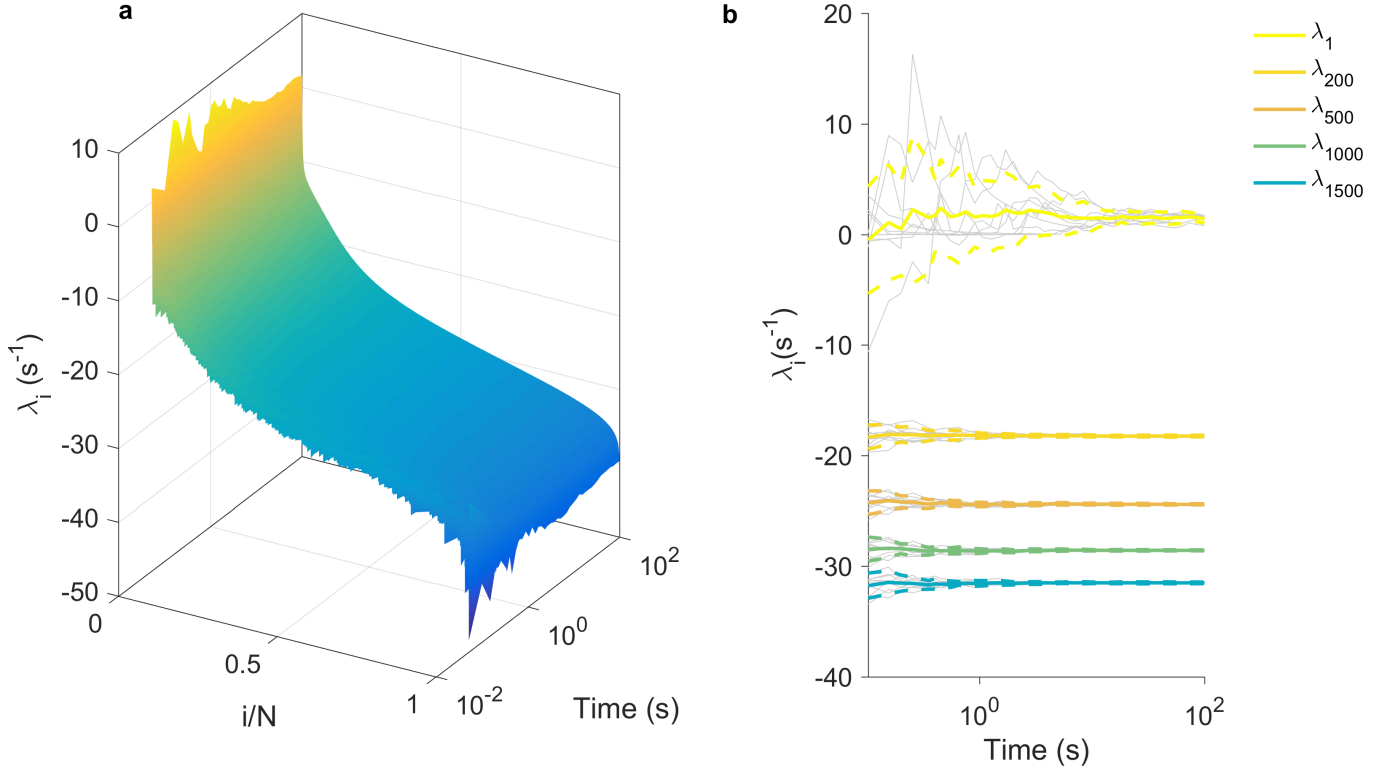


Figure 21. **Convergence of Lyapunov spectra versus time in inhibitory rapid theta networks for large AP rapidness ($r=100$).** (logarithmic time scale) **a)** Convergence of Lyapunov spectrum for one initial condition, **b)** gray lines: some Lyapunov exponents for ten different network realizations, solid color lines: averages, dotted color lines: averages \pm double standard errors (parameters: $N = 2000$, $\bar{\nu} = 1$ Hz, $K = 100$, $J_0 = 1$, $\tau_m = 10$ ms).

approximation, the mean Lyapunov exponent for inhibitory networks becomes

$$\begin{aligned}\bar{\lambda} &\approx \frac{1}{N} N \bar{\nu} \int \ln(d(V)^K) P(V) dV \\ &= K \bar{\nu} \int \ln d(V) P(V) dV.\end{aligned}\quad (72)$$

We obtain $d(V)$ from Eq. (60) using Eq. (54)

$$d_-(V) = \begin{cases} \frac{(V-V_G)^2 + \frac{I_0 \sqrt{K}}{a_S}}{(V-V_G + C\sqrt{I})^2 + \frac{I_0 \sqrt{K}}{a_S}} & V \leq V_G \\ \frac{r^2(V-V_G)^2 + \frac{I_0 \sqrt{K}}{a_S}}{(V-V_G + C\sqrt{I})^2 + \frac{I_0 \sqrt{K}}{a_S}} & V_G < V < V_- \\ \frac{r^2(V-V_G)^2 + \frac{I_0 \sqrt{K}}{a_S}}{r^2(V-V_G + C\sqrt{I})^2 + \frac{I_0 \sqrt{K}}{a_S}} & V_- \leq V. \end{cases}\quad (73)$$

In the large K limit, $d(V)$ can be approximated by

$$d_-(V) \stackrel{K \rightarrow \infty}{\simeq} \begin{cases} 1 + \frac{2a_S J_0 (V-V_G)}{I_0 K} + \mathcal{O}(K^{3/2}) & V \leq V_G \\ 1 + \frac{a_S (r^2 - 1)(V-V_G)^2}{I_0 \sqrt{K}} + \frac{(2a_S J_0 - (r^2 - 1)(V-V_G)^3)(V-V_G)}{I_0^2 K} + \mathcal{O}(K^{3/2}) & V_G < V < V_- \\ 1 + \frac{2a_S r^2 J_0 (V-V_G)}{I_0 K} + \mathcal{O}(K^{3/2}) & V_- \leq V. \end{cases}\quad (74)$$

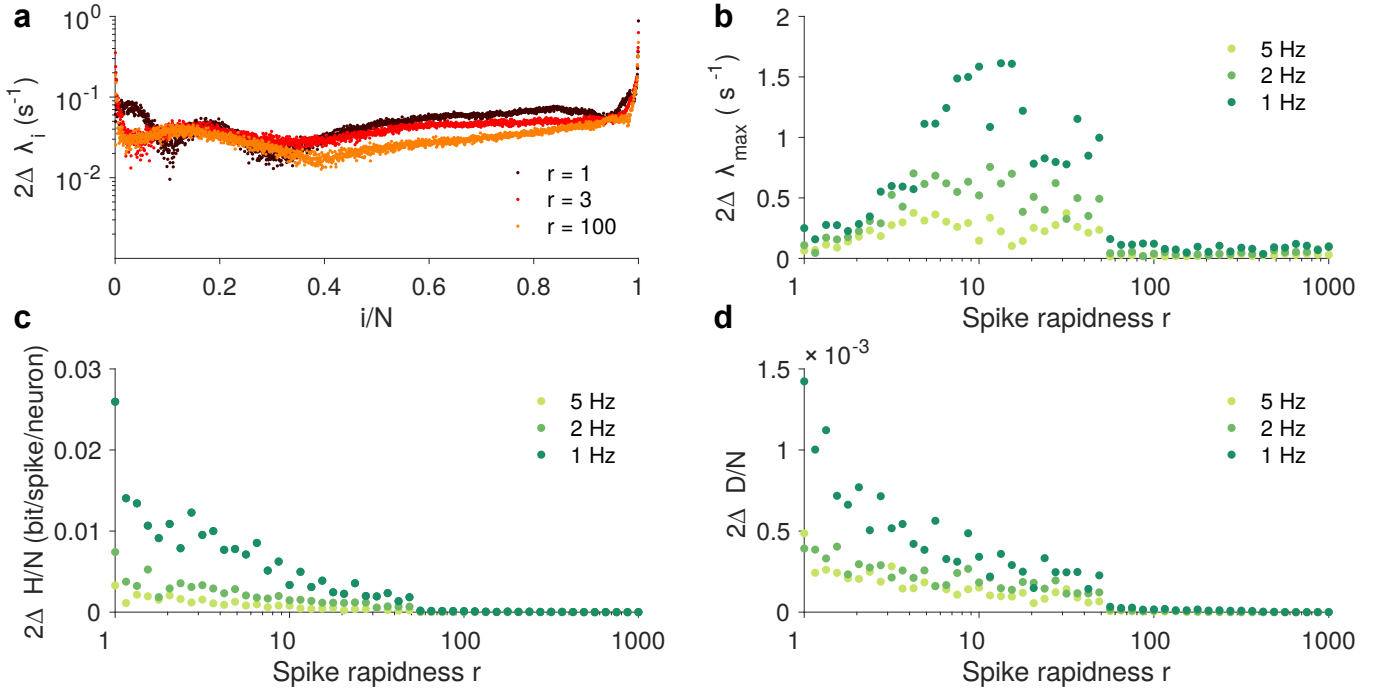


Figure 22. **Small double standard error of Lyapunov exponents, dynamical entropy rate and attractor dimension in random inhibitory network** **a)** double standard error of Lyapunov exponents across different network realizations for different values of rapidness. **b)** double standard error across network realizations of largest Lyapunov exponent for different values of rapidness. **c)** same as **b)** for dynamical entropy rate. **d)** same as **b)** for relative attractor dimension. Note that all standard errors are orders of magnitude smaller than the mean values for the respective quantities. ($N = 2000$, $K = 100$, $J_0 = 1$, $\tau_m = 10$ ms).

These approximations, along with the balance equation (66), lead to

$$\bar{\lambda} \stackrel{K \rightarrow \infty}{\simeq} \frac{2a_S \langle V_{V \leq V_G} \rangle}{\tau_m} \alpha + \frac{2u \langle V_{V > V_G} \rangle}{\tau_m} (1 - \alpha) + \mathcal{O}\left(\frac{1}{\sqrt{K}}\right), \quad (75)$$

where $\langle V_{V \leq V_G} \rangle$ ($\langle V_{V > V_G} \rangle$) denotes the average membrane potential below (above) V_G , and α is the fraction of neurons below V_G .

We have compared the derived random matrix approximations of the mean Lyapunov exponent in inhibitory networks Eq. (72) and the large- K limits, Eq. (75), with the results from simulations (**Fig. 24**). They are in very good agreement, indicating the validity of the random matrix approximation. This likely results from the commutativity of the determinants of the Jacobians, a property that generally does not hold for the product of the Jacobians.

XII. SCALING OF THE LARGEST LYAPUNOV EXPONENT WITH NETWORK PARAMETERS

The largest Lyapunov exponent exhibits a single maximum as a function of the action potential onset rapidness. The peak position, which we call peak rapidness r_{peak} , scales approximately as shown in **Fig. 25**:

$$r_{\text{peak}} \propto \sqrt{\frac{K \nu_0 \tau_m}{J_0}} \quad (76)$$

This behavior can be understood as a transition between two qualitatively different scaling regimes for the largest Lyapunov exponent. For small values of K and $\bar{\nu}$ the largest Lyapunov exponent grows, while for large values of K and $\bar{\nu}$ the largest Lyapunov exponent reaches a plateau. Qualitative differences between these two collective network states become clear in the localization of the first covariant Lyapunov vector, the local Lyapunov exponents and in a spatiotemporal analysis of the network chaos in section XIII.

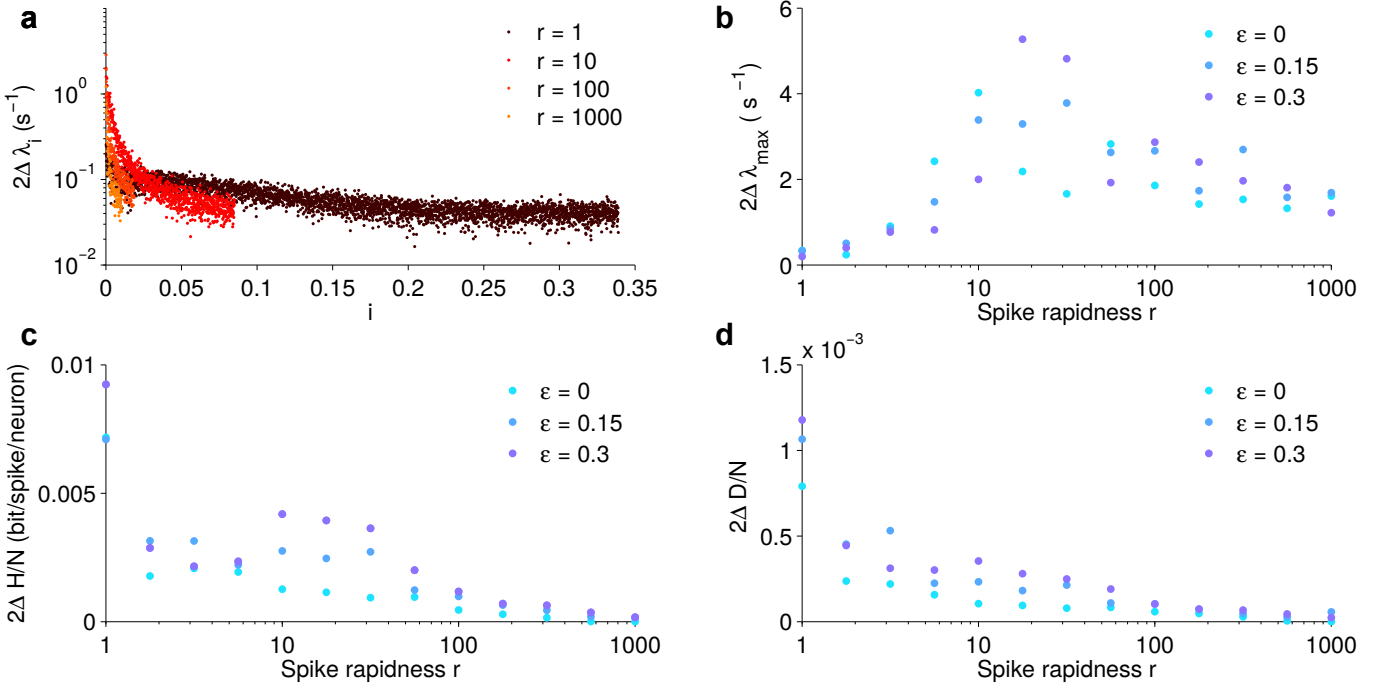


Figure 23. **Small double standard error of Lyapunov exponents, dynamical entropy rate and attractor dimension in random mixed network** **a)** double standard error of Lyapunov exponents across different initial conditions for different values of rapidness ($\epsilon = 0.3$). **b)** double standard error across network realizations of largest Lyapunov exponent for different values of rapidness. **c)** same as **b)** for dynamical entropy rate. **d)** same as **b)** for relative attractor dimension. Note that all standard errors are orders of magnitude smaller than the mean values for the respective quantities. ($N_E = 8000$, $N_I = 2000$, $K = 100$, $J_0 = 1$, $\tau_m = 10$ ms).

The critical spike onset rapidness r_{crit} separates the chaotic dynamics from the stable dynamics. This transition with network parameters has the following scaling behavior (**Fig. 27**):

$$r_{\text{crit}} = N^{0.5} K^{0.4} \bar{\nu}^{0.8} \tau_m^{0.8} J_0^{-0.7} \quad (77)$$

This scaling indicates that in the thermodynamic limit of large K and large N , the critical rapidness r_{crit} diverges and the network is always chaotic. This is in agreement with the scaling of the flux tube radius of networks of leaky integrate and fire neurons, which goes to zero in the limit of large networks. Note however that even in the thermodynamic limit it is possible to bring the largest Lyapunov exponent and thus also the Kolmogorov Sinai entropy rate arbitrarily close to zero by increasing the AP onset rapidness r .

Extensivity of Lyapunov spectrum and asymptotic form: **Figure 2** and **3** of the main paper show that for sufficiently large networks the dynamical entropy rate and Kaplan-Yorke attractor dimension scales linear with network size N indicating extensive deterministic chaos. While the dynamical entropy rate and Kaplan-Yorke attractor dimension converge to a linear scaling with N already for moderate network size, the largest Lyapunov exponent exhibited a slower convergence to its large N limit (**Fig. 28**). While the peak rapidness r_{peak} is independent of N , $\lambda_{\text{max}}(N)$ converges exponentially towards its large N limit. This exponential convergence allows an estimate of the asymptotic value $\lim_{N \rightarrow \infty} \lambda_{\text{max}}(N)$, indicated in **Fig. 28b** by a dashed line. Note that the critical rapidness r_{crit} diverges with N as shown in **Fig. 27**.

XIII. PARTICIPATION RATIO AND LOCALIZATION OF CHAOS

To quantify how many neurons contribute to the chaotic dynamics at each and every moment in time, we investigated properties of the covariant Lyapunov vectors $\delta\vec{\phi}^c(t)$. The first Lyapunov vector, which corresponds to the first Gram-Schmidt vector ($\sum_{i=1}^N \delta\phi_i(t)^2 = 1$) gives at any point in time the direction in which almost all initial

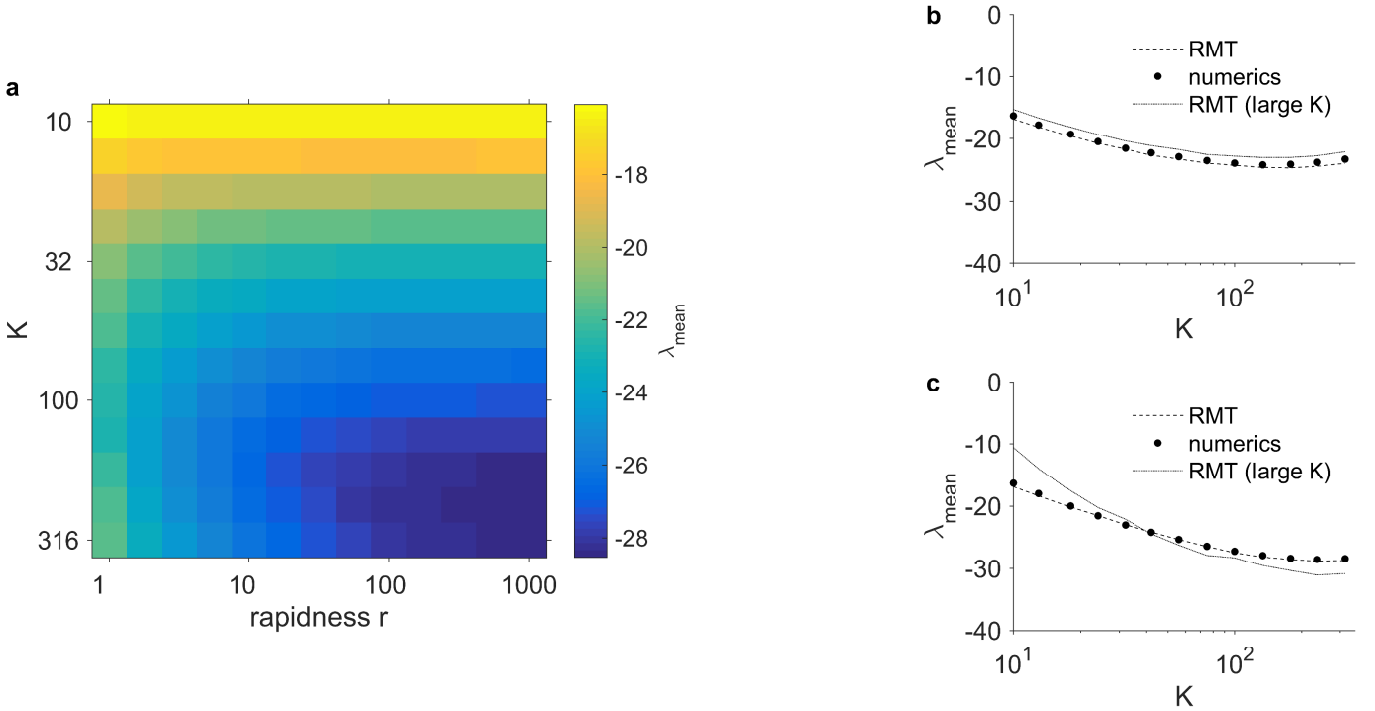


Figure 24. **Good match between mean Lyapunov exponent in random matrix approximations and numerical simulations in balanced rapid theta neuron networks.** **a)** Mean Lyapunov exponent from numerical simulations for different K and r with $N = 1000$. **b)** K -dependence for $r = 3$. Solid lines: numerical simulations, dashed lines: random matrix approximations with full membrane potential distributions, dotted lines: random matrix approximation in the large K -limit **c)** K -dependence for $r = 100$. Eq. (75) (parameters: $\bar{\nu} = 1$ Hz, $J_0 = 1$, $\tau_m = 10$ ms).

infinitesimal perturbations grow with average rate λ_{\max} . The number of neurons contributing to the maximally growing direction at time t can be measured by the participation ratio $P(t) = \left(\sum_{i=1}^N |\delta\phi_i(t)|^4\right)^{-1}$ [39–41]. If all neurons contribute similarly to the Lyapunov vector $|\delta\phi_i(t)| = 1/\sqrt{N}$ the participation ratio is $P(t) = 1/(N/N^2) = N$. If only one neuron contributes to the Lyapunov vector the participation ratio is $P(t) = 1$. We found that the participation ratio strongly depends on the spike onset rapidness. Increasing rapidness generally reduced the participation ratio (**Fig. 29**) for large networks. This means that for increasing rapidness fewer neurons contribute to the most unstable direction. On the level of the single neuron dynamics, this can be explained by a decreasing fraction of (postsynaptic) neurons that are in the unstable regime with voltages above the glue point V_G for increasing values of r . Thus, there exist on average fewer entries in the Jacobian with large entries $d(V_i)$. Therefore, the first Lyapunov vector is on average expected to have few entries with large values.

To further characterize the nature of the chaotic collective network state, it is crucial to investigate the scaling of the mean participation ratio $\bar{P} = \langle P(t) \rangle$ with network size. Whether the Lyapunov vector is called localized or delocalized depends on how \bar{P} scales as a function of network size N . A delocalized state is indicated by a linear scaling $\bar{P} \sim N$, while in case of a localized state, the participation ratio would be independent of N .

In an earlier study of theta neurons, corresponding to $r = 1$, it was found that the Lyapunov vector was dominated by subsets of neurons that changed over time [12]. The participation ratio exhibited a sublinear scaling $\bar{P} \sim N^\alpha$, with $0 < \alpha < 1$. Here, we found a strong dependence of the participation ratio and localization on the spike onset rapidness r . For increasing spike onset rapidness r , the exponential scaling parameter α decreased approximately logarithmically as function of r and turned zero at a certain value of rapidness that depends on firing rate $\bar{\nu}$, coupling strength J_0 , number of synapses per neuron K , and membrane time constant τ_m (**Fig. 30**). For larger values of rapidness, there was on average a fixed number of neurons contributing to the first Lyapunov vector, which was independent of network size N for sufficiently large networks. An extensive analysis of the scaling of the onset rapidness with network parameters where the localization occurred coincided with the scaling of the rapidness where the Lyapunov

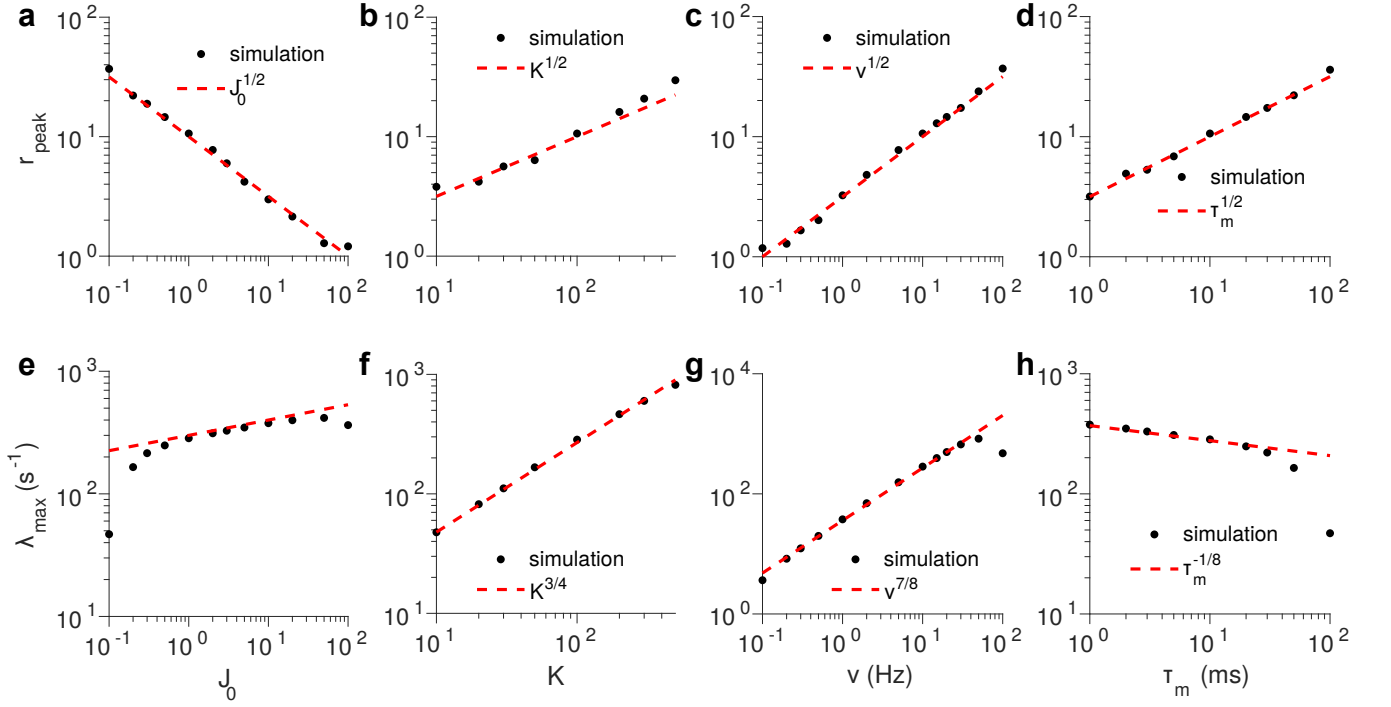


Figure 25. **Scaling of peak AP onset rapidness r_{peak} with network parameters in balanced inhibitory networks** $r_{\text{peak}} \propto \sqrt{K\nu_0\tau_m/J_0}$. At the peak onset rapidness r_{peak} the largest Lyapunov exponent has its maximum as a function of rapidness (**Fig. 2** of main paper). **a)** peak onset rapidness r_{peak} vs. J_0 , dashed red lines indicate power-law fit using the Levenberg-Marquardt algorithm. **b)** peak onset rapidness r_{peak} vs. K . **c)** peak onset rapidness r_{peak} vs. J_0 . **d)** peak onset rapidness r_{peak} vs. J_0 . **e-h)** Second row: corresponding peak onset rapidness λ_{max} (parameters: $\bar{\nu} = 1$ Hz, $J_0 = 1$, $\tau_m = 10$ ms, $N = 1000$, $K = 100$).

exponents peaks (**Fig. 30**)

$$r_{\text{localization}} \propto \sqrt{\frac{K\nu_0\tau_m}{J_0}}. \quad (78)$$

The scaling behavior indicates that the localization of the first Lyapunov vector occurs when K , ν_0 or τ_m is sufficiently small or when J_0 is sufficiently large. Thus, localization occurs, when there are few postsynaptic potentials per spike (K small), which occur infrequent (ν_0 or τ_m small), and/or are strong (J_0 large).

Note that despite the same scaling, localization occurs always at slightly larger values of rapidness than the peak in the largest Lyapunov exponent. So the first Lyapunov vector seems to localize not until the largest Lyapunov exponent is in the regime where it is independent of the number of synapses per neuron K .

For large values of spike onset rapidness r at a fixed network size N , we found that the participation ratio increases with rapidness until it saturates at $\bar{P} = N$ (**Fig. 31a**). This saturation occurred exactly at the critical spike onset rapidness r_{crit} , when the largest Lyapunov exponent becomes zero (**Fig. 31c**).

XIV. CELLULAR DYNAMICS PROPEL NETWORK CHAOS AT INSTABILITY EVENTS

To scrutinize how the collective network chaos depends on the single neuron dynamics, we performed a time-resolved analysis of the first covariant Lyapunov vector and the state of postsynaptic neurons. The first covariant Lyapunov vector is ruled by a small and temporally varying fraction of neurons (**Fig. 32a**). We found different behavior of the local Lyapunov exponent in the localized regime: There were infrequent *instability events* with large local Lyapunov exponents, which coincided with a sudden decrease of the participation ratio $P(t)$. When these *instability events* occurred, a postsynaptic neuron was in the instable regime of its internal dynamics **Fig. 33**. Larger spike onset rapidness r leads to shorter but more unstable episodes of postsynaptic neurons in the susceptible regime. The envelop of the local Lyapunov vector weighted by the entries of the first Lyapunov vector as function of the

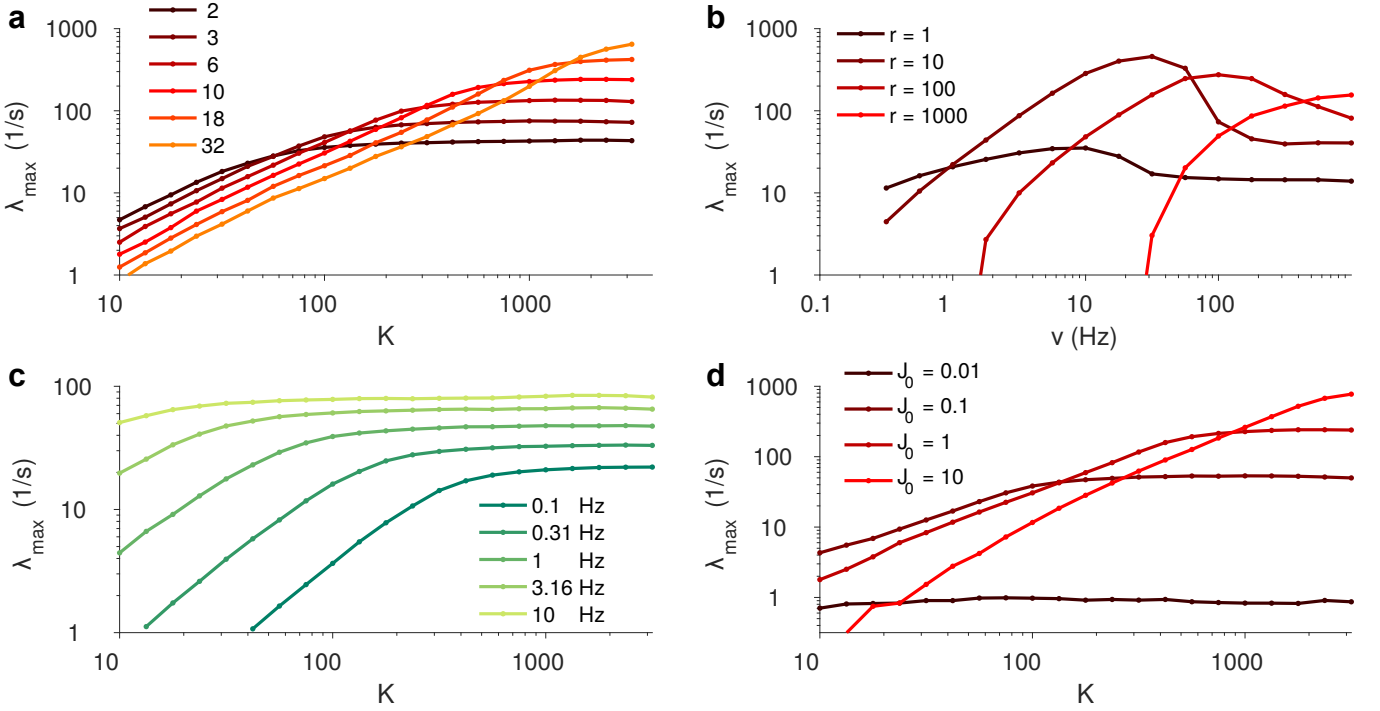


Figure 26. **Different scaling regimes explain peak in the largest Lyapunov exponent λ_{\max} .** **a)** K -dependence of largest Lyapunov exponent for different values of rapidness r with $N = 10000$. **b)** ν -dependence of largest Lyapunov exponent for different rapidness r . **c)** K -dependence of largest Lyapunov exponent for mean firing rate ν_0 with $N = 1000$. **d)** K -dependence of largest Lyapunov exponent for different coupling strength J_0 (parameters: $\bar{\nu} = 10$ Hz, $J_0 = 1$, $\tau_m = 10$ ms, $N = 10000$, $K = 100$).

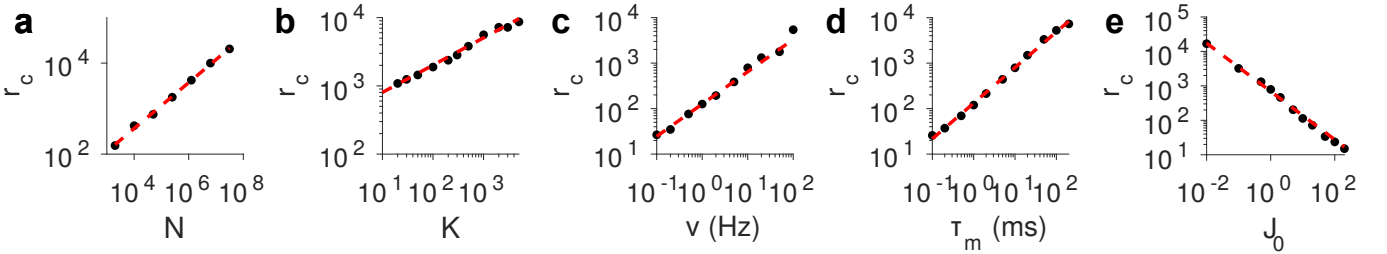


Figure 27. **Scaling of critical AP onset rapidness r_c between stable and chaotic dynamics in balanced inhibitory networks** $r_{\text{crit}} \propto N^{0.5} K^{0.4} \bar{\nu}^{0.8} \tau_m J_0^{-0.7}$. The critical spike rapidness r_{crit} separates chaotic dynamics (above) from stable dynamics (below). **a)** r_{crit} vs. N , **b)** r_{crit} vs. K , **c)** r_{crit} vs. $\bar{\nu}$, **d)** r_{crit} vs. τ_m , **e)** r_{crit} vs. J_0 Power-law fits done using the Levenberg-Marquardt algorithm (parameters: $\bar{\nu} = 10$ Hz, $J_0 = 1$, $\tau_m = 10$ ms, $N = 2000$, $K = 100$).

postsynaptic phase is captured by the derivative of the phase-response curve. This establishes a direct link between the collective network chaos and the single neuron dynamics.

XV. PAIRWISE CORRELATIONS IN RAPID THETA NETWORKS

Figure 3 e-g of main paper. We measured spiking correlations using zero-lag pairwise Pearson spike count correlations. First we obtained spike counts $n(t)$ by binning the spike train of each neuron i into bins of window size T_{win} . The pairwise Pearson spike count correlation between spike trains of neuron i and j was then calculated using the standard expression [6]:

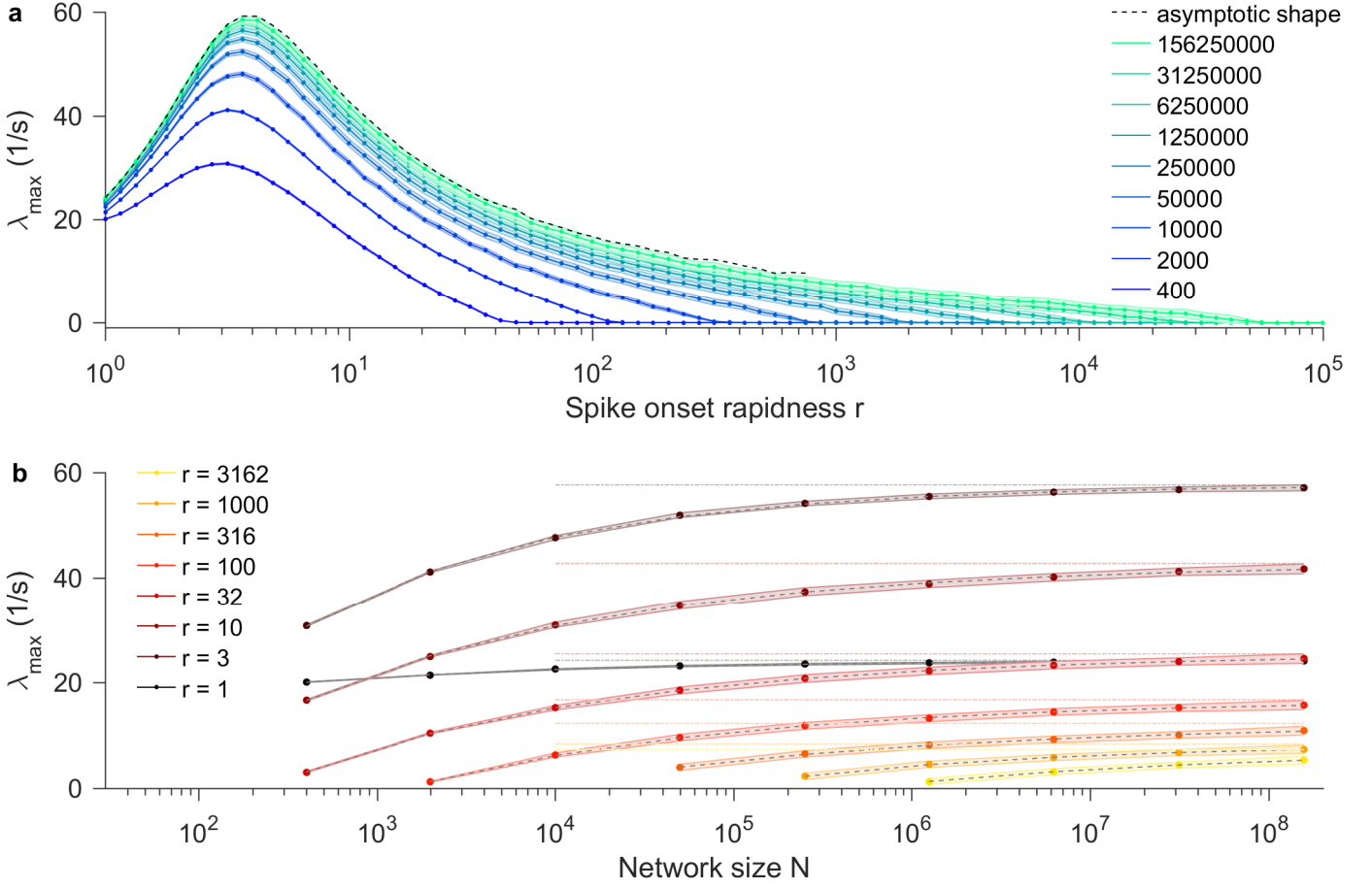


Figure 28. **Largest Lyapunov exponent converges to asymptotic shape for very large network size N :** **a)** The largest Lyapunov exponent exhibits a slow convergence with network size N ($\bar{\nu} = 1$ Hz). **b)** The convergence of $\lambda_{\max}(N)$ can be accurately fitted by $\lambda_{\max}(N) = \lambda_{\max}(\infty) - c \cdot N^{-\frac{1}{\gamma}}$, where $\lambda_{\max}(\infty) = \lim_{N \rightarrow \infty} \lambda_{\max}(N)$ (median (dots) across 10 topologies, shaded error shadings indicate median bootstrapped 95% confidence intervals). The estimated $\lambda_{\max}(\infty)$ is indicated by a black dashed line. ($r = 10$, $\bar{\nu} = 10$ Hz) (parameters: $J_0 = 1$, $\tau_m = 10$ ms, $K = 100$).

$$r_{ij} = \frac{\text{cov}(n_i, n_j)}{\sigma_i \sigma_j}, \quad (79)$$

where $\text{cov}(n_i, n_j)$ is the covariance between the spike counts of cells i and j and σ_i, σ_j are the respective standard deviations. By definition, $r_{ij} \in [-1, 1]$. For figure 3 of the main paper, we chose a window size of $T_{\text{win}} = 20$ ms.

To estimate the effect of our limited sampling time, we generated jittered spike trains, where the total number of spikes per neuron was fixed but the spike times drawn uniformly in the interval $[0, T_{\text{total}}]$, where T_{total} is the total simulation time. We calculated the correlation of the shuffled spike trains r_{ij}^{shuffled} using the same binning and definition for the correlation.

To provide a fair comparison of pairwise correlations for networks with different spike onset rapidness r , the mean firing rate $\bar{\nu}$ was fixed by adapting the external current I_{ext} .

Additional results: We characterized the effect of different count window sizes T_{win} on the mean and standard deviation of the pairwise spike count correlation (**Fig. 34**).

At large count window size, the mean pairwise correlations tend to be smaller for large rapidness. This can be explained by the faster inhibitory feedback for large action potential onset rapidness. As for large rapidness, rapid theta neurons are capable of tracking input changes more quickly (**Figure 1d, e** of main paper). Therefore, the dynamic decorrelation of balanced networks, which was described earlier [6], is more effective. For small bin size, the mean pairwise correlations of rapid theta neurons with large rapidness are larger. This is because rapid theta neurons

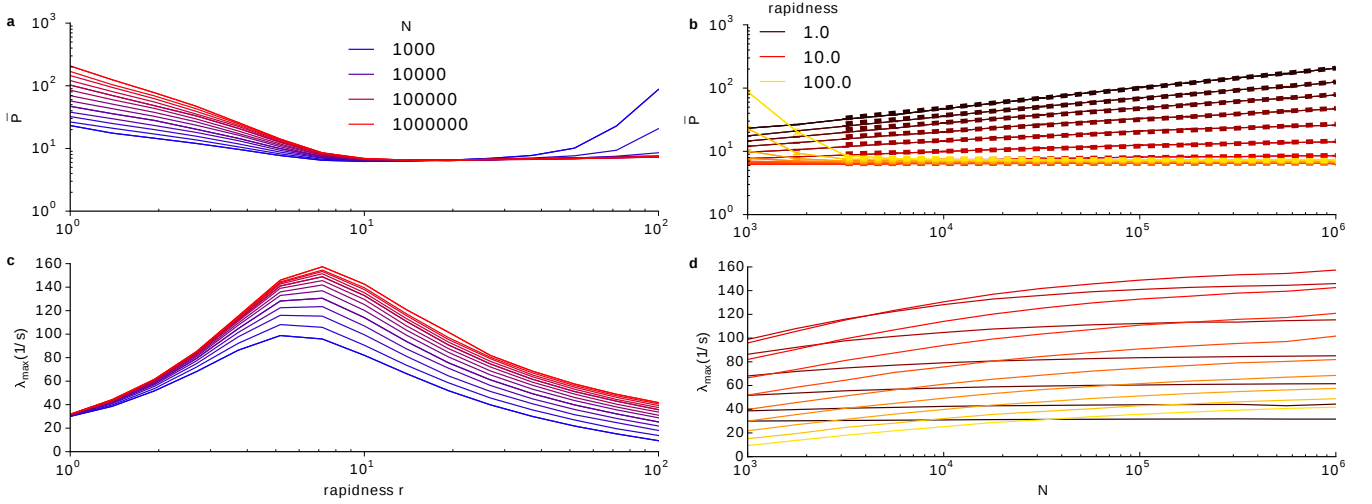


Figure 29. **Average participation ratio vs rapidness r and network size N reveals localization of first covariant Lyapunov vector above peak rapidness:** **a)** The mean participation ratio \bar{P} versus rapidness r , colors encode network size N . **b)** \bar{P} versus N , colors encode rapidness r . \bar{P} shows power-law scaling $\bar{P} \sim N^\alpha$, where the exponent α decreases as function of rapidness r , dashed lines indicate power-law fits using the Levenberg-Marquardt algorithm (see **Fig. 30** for comprehensive scaling of α). **c)** The largest Lyapunov exponent vs rapidness r exhibits a peak approximately where the participation ratio becomes independent of network size N in **a**. **d)** The largest Lyapunov exponent vs. N converges exponentially to asymptotic limit (parameters: $\bar{\nu} = 3$ Hz, $J_0 = 1$, $\tau_m = 10$ ms, $K = 100$).

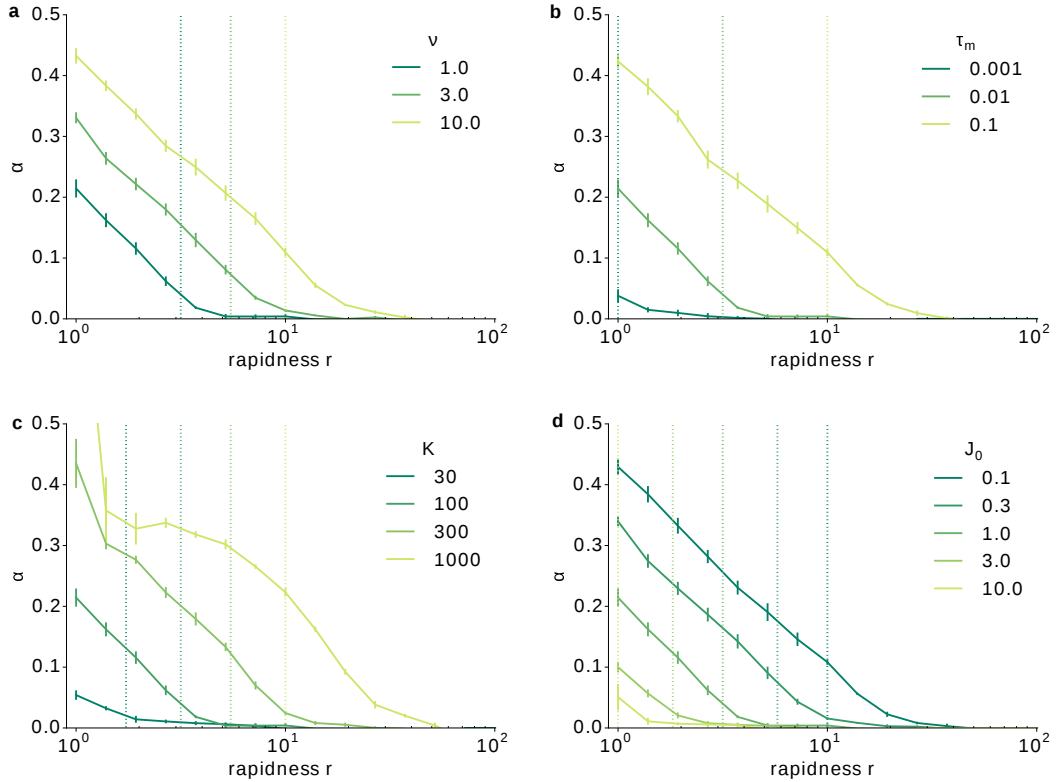


Figure 30. **Scaling of participation ratio with network parameters shows that localization of first covariant Lyapunov vector has same r -scaling as peak rapidness:** **a)** power-law scaling exponent α from $\bar{P} \sim N^\alpha$ fits mean firing rate $\bar{\nu}$ decreases approximately logarithmically as function of r . Dashed vertical lines indicate corresponding values of peak rapidness r_{peak} . **b)** Same for different membrane time constants τ_m . **c)** Same for different number of synapses per neuron K . **d)** Same for different coupling strengths J_0 (parameters: $N = 10^3 - 10^6$, $K = 100$, $\bar{\nu} = 1$ Hz, $J_0 = 1$, $\tau_m = 10$ ms, $\varepsilon = 0.3$).

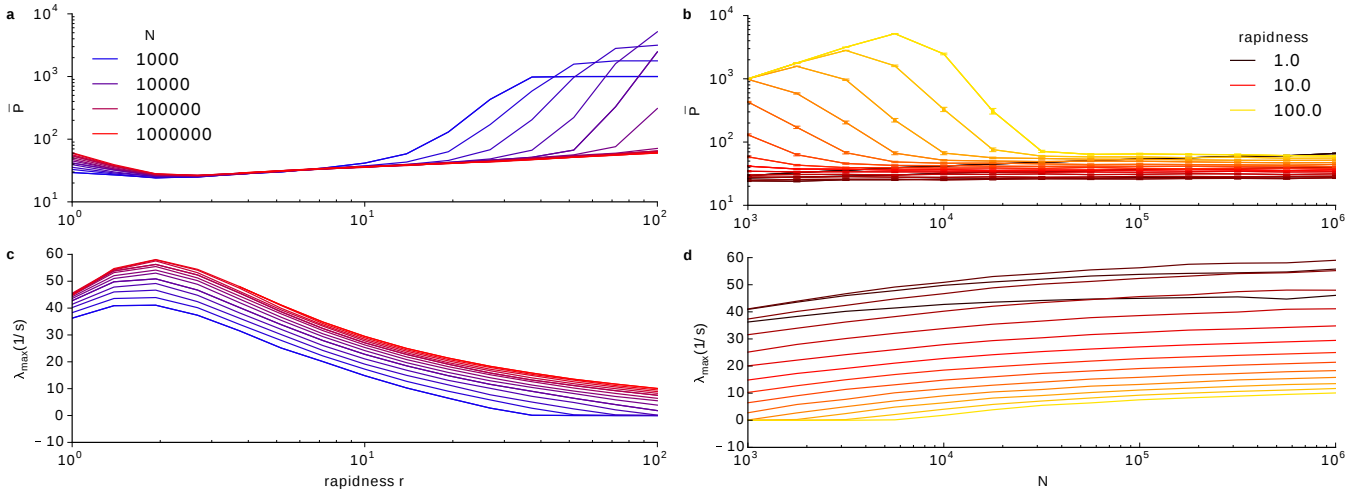


Figure 31. **Average participation vs rapidness r and network size N reveals delocalization of first covariant Lyapunov vector at critical rapidness:** Same as Fig. 29 for $\bar{\nu} = 1$ Hz, $J_0 = 3$. Note that for large spike onset rapidness r the mean participation \bar{P} increases in small networks and saturates at $\bar{P} = N$, when the largest Lyapunov exponent becomes zero (parameters: $\bar{\nu} = 1$ Hz, $J_0 = 3$, $\tau_m = 10$ ms, $K = 100$).

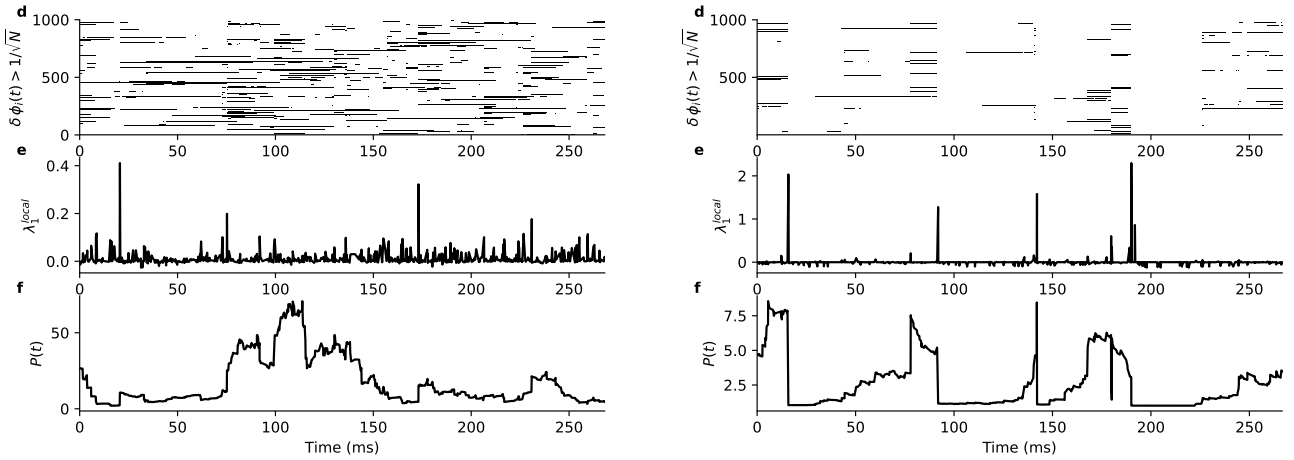


Figure 32. **Cellular dynamics propel network chaos at instability events:** **a)** First covariant Lyapunov vector $\delta\vec{\phi}(t)$ (black whenever $|\delta\phi(t)| > 1/\sqrt{N}$). **b)** First local Lyapunov exponent $\lambda_1^{\text{local}}(t)$, **c)** participation ratio $P(t)$ of first covariant Lyapunov vector for $r \approx 1.33$. **d), e), f)** same as **a, b, c** for $r \approx 31.6$. Note that the largest Lyapunov exponent is approximately the same for the left and right column, but the network is in the two different regimes described in section XIII. Parameters as in Fig. 29 with $N = 1000$.

which receive shared excitatory input and are kicked across the unstable fixed point will spike almost instantaneously, which results in moderately increased correlations on very short time scales (Fig. 34b).

Cross-correlograms: The cross-correlogram between the pairs of the binned the spike trains $n_i(t)$ and $n_j(t)$ was calculated as:

$$c_{ij}(\tau) = \frac{\text{cov}(n_i(t), n_j(t + \tau))}{\bar{\nu}_i \bar{\nu}_j} - 1. \quad (80)$$

where $\text{cov}(n_i, n_j)$ is the covariance between the spike counts of cells i and j and $\bar{\nu}_i, \bar{\nu}_j$ are the respective mean firing rates. By definition $c_{ij} \in [-\infty, \infty]$, but $\lim_{t \rightarrow \infty} c_{ij} = 0$ for shuffled spikes.

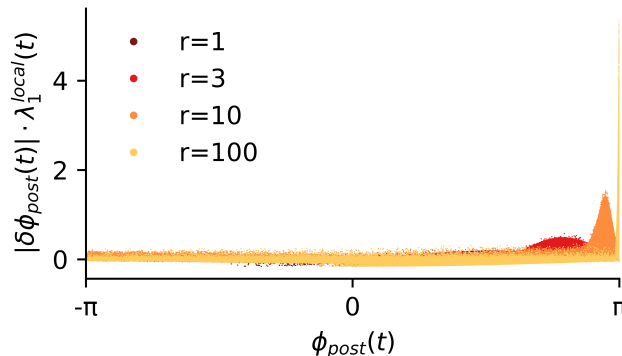


Figure 33. **Network chaos is mostly sustained by postsynaptic neurons close to spiking:** Local Lyapunov exponent projected on entries of first Lyapunov vector of postsynaptic neurons vs. phase of postsynaptic neurons for different rapidness r . Large local Lyapunov exponents are associated with postsynaptic neurons with $\phi_{\text{post}} > \phi_{\text{G}}$. Larger spike onset rapidness r leads to shorter but more unstable episodes of postsynaptic neurons in susceptible regime. The envelop of this figure is captured by the derivative of the phase-response curve. Parameters as in **Fig. 29** with $N = 1000$ and $T_{\text{total}} = 600$ s).

XVI. ATTRACTOR DIMENSION AND “ENTANGLED” STATISTICS

In the main paper, we show both an upper and lower bound for the attractor dimension which both strongly depend on the spike onset rapidness (**Fig. 3**). For increasing spike rapidness, the network dynamics has a transition from chaotic to stable dynamics. While chaotic dynamics is accompanied in continuous dynamical systems by a fractal attracting set with dimension $D > 2$, stable dynamics has an attractor dimension $D = 1$. Here, we compare this to Gaussian estimates of the dimensionality, based on pairwise correlations, to evaluate higher order correlations. Assuming Gaussian statistics, all dependencies between neurons would be captured by the pairwise correlations. Based on the correlation matrix, an estimate of the dimensionality can be obtained. We use two common estimators of the dimensionality: the number of principle components needed explain 95% of the correlation matrix’s variance and a dimensionality based on the participation ratio of the correlation matrix that measures the effective number of degrees of freedom over which power is distributed.

Figure 35a+b shows the correlation matrix for two different values of spike onset rapidness. Principal component analysis (PCA) yields the percentage of the total variance explained by each principal component (**Fig. 35c**). The number of principal components necessary to account for 95% of the total variance gives an estimate of the number of degrees of freedom of the underlying dynamics. If few principal components would explain most of the variance, most of the dynamics is constrained to a hyperellipsoid with few large axes. If many principal components are necessary to explain most of the variance, no such collective structures are detected. This excludes the possibility that the dynamics is explained solely by pairwise correlations. A different estimate of the dimensionality based on the correlation matrix is the inverse participation ratio of the eigenvalue spectrum of the correlation matrix. The inverse participation ratio is defined as the normalized inverse squared sum of eigenvalues of the correlation matrix:

$$D_{\text{PR}} = \frac{(\sum \lambda_i)^2}{\sum (\lambda_i^2)} \quad (81)$$

where λ_i is the i^{th} eigenvalue of the correlation matrix. Thus, D_{PR} is 1 if one eigenvalue is dominating while the others are zero. If all eigenvalues contribute equally $\lambda_i = \frac{1}{N}$, the dimension is N [12, 13, 58, 92]. The dimensionality estimate based on the participation ratio also shows that the pairwise correlations have very little localized structure independent of spike onset rapidness (**Fig. 37b+d**). Furthermore, we show that this result is largely insensitive to the spike count window of the correlation matrix (**Fig. 37a+c**). To conclude, we find a low attractor dimensionality based on the Kaplan-Yorke dimension and our lower bound estimate coming from the number of positive Lyapunov exponents, despite low and weakly structured pairwise correlations. To obtain a precise estimate of the pairwise spike count correlations, we averaged the correlation matrix over 100 runs with different initial conditions but identical network topology each with $T_{\text{total}} = 1000$ s.

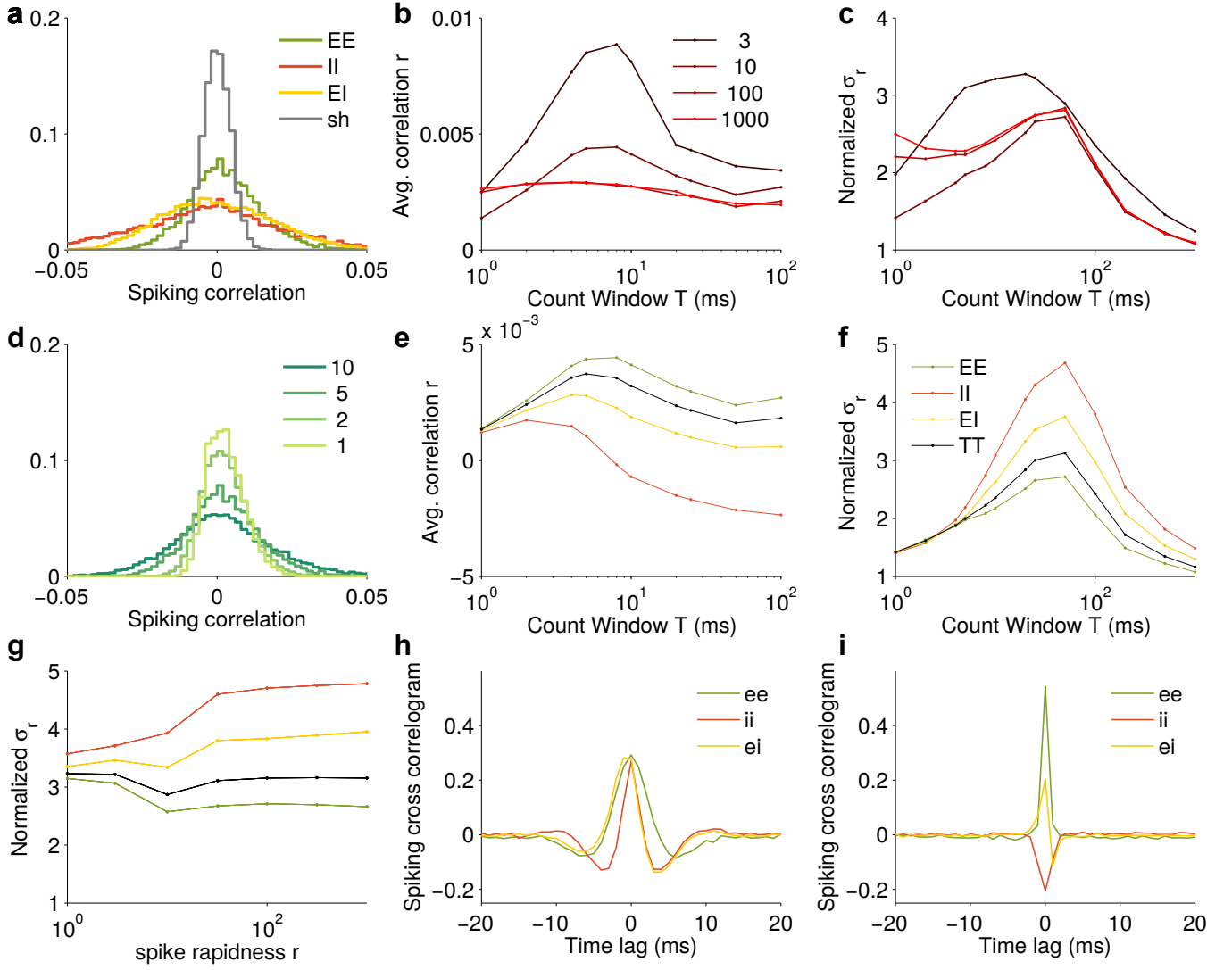


Figure 34. **Pairwise correlations in balanced spiking networks with different values of spike onset rapidness:** **a)** Histograms of the pairwise count spike correlation r_{ij} for different cell pairs from excitatory and inhibitory populations (count window $T_{\text{win}} = 20$ ms. Jittered spike trains were generated by Poisson process of same rate. **b)** Mean of pairwise spike count correlation vs. count window sizes T_{win} for different values of rapidness. **c)** Standard deviation of spike count correlations vs. T_{win} for different values of rapidness. **d)** Histogram of pairwise correlations for different mean firing rates. **e)** Standard deviation of pairwise spiking correlation as a function of rapidness for $T_{\text{win}} = 20$ ms. **f)** Average spike cross correlogram of different pair types for rapidness $r = 10$ **g)** same as **f)** for $r = 1000$. **h)** Spiking cross correlogram of different pair types for rapidness $r = 10$. **i)** same as **h)** for $r = 1000$ (parameters as in **Fig. 3** of main paper).

XVII. NETWORK SYNCHRONY

We quantify network synchrony network by using the network synchrony measure [78]: $\chi^2 = \frac{\sigma_{\phi(t)}^2}{\sum_{i=1}^N \sigma_{\phi_i(t)}^2 / N}$, where $\phi(t) = \sum_{i=1}^N \phi_i(t) / N$ is the mean activity in a phase representation. We find that networks are in an asynchronous regime with $\chi \propto \frac{1}{\sqrt{N}}$ for various values of r across 4 order of magnitude (see **Fig. 38**). We note that balanced networks of theta neurons ($r = 1$) have well-known pathological network oscillations [70] for large K and strong coupling J_0 /low firing rate that were recently described in a mean-field approach [96]. We observed in rapid theta (and also EIF) networks, that increasing rapidness r causes oscillations to vanish -or requires a larger K for oscillations to emerge [70]. A more detailed account will be given elsewhere.

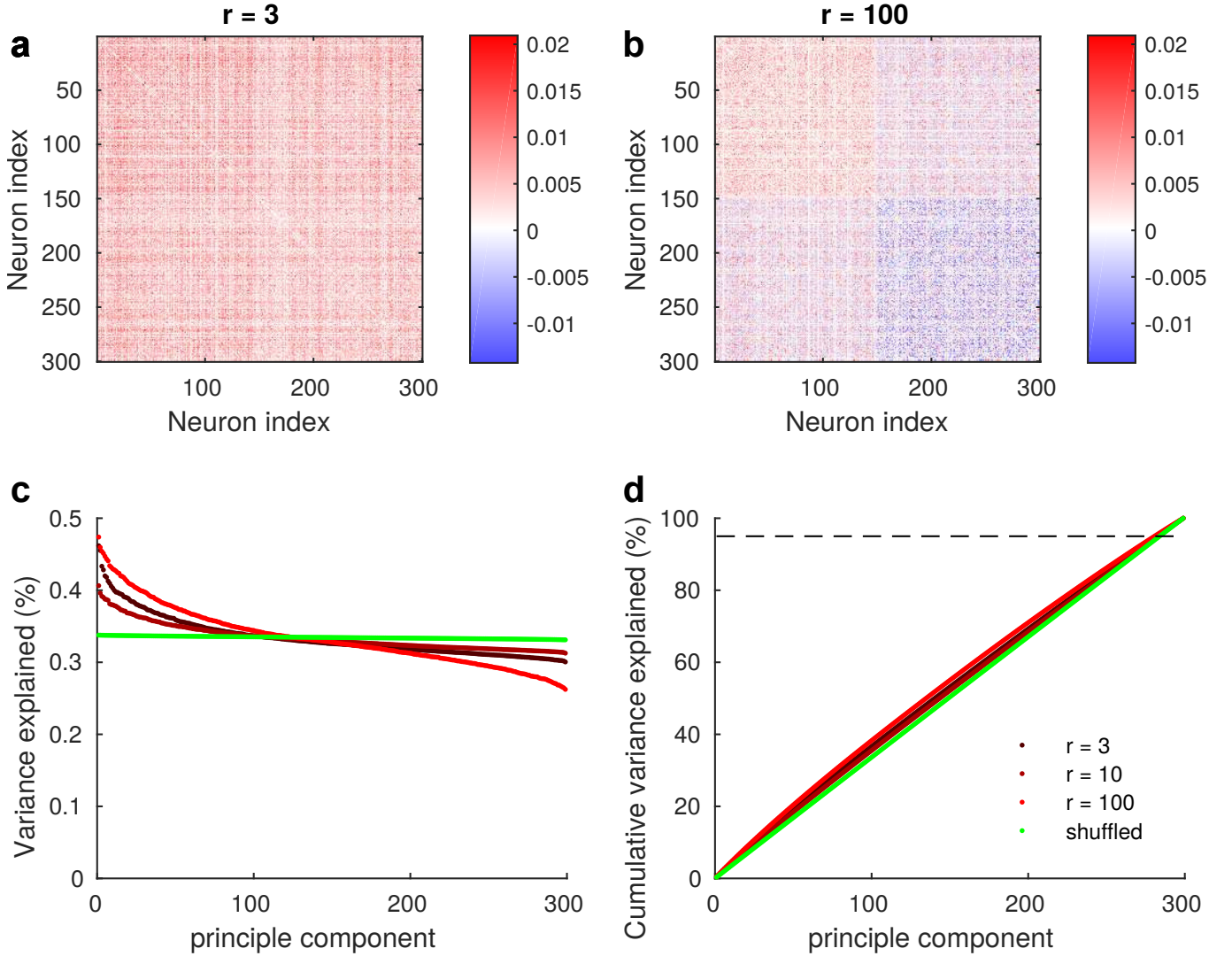


Figure 35. **Weakly structured correlation matrix in balanced spiking networks with different values of spike onset rapidness:** **a)** Matrix of pairwise spike count correlations r_{ij} for rapidness $r = 3$. First 150 neurons are excitatory, others inhibitory. **b)** same for $r = 100$. **c)** Variance explained per principal component for different rapidness. Jittered spike trains were generated by a Poisson process of the same rate. **d)** Cumulative variance explained for different values of rapidness, (parameters: $T_{\text{win}} = 20$ ms, $T_{\text{total}} = 1000$ s, other parameters as in **Fig. 34**).

XVIII. FLUX-TUBE STRUCTURE OF PHASE SPACE, STABLE CHAOS AND SINGLE-SPIKE PERTURBATIONS

Figure 3 d,h of main paper: For sufficiently large spike onset rapidness, we find that infinitesimal perturbations decay exponentially but sufficiently strong perturbation lead to an exponential decorrelation of neighboring trajectories. This exotic phase space structure was first described in balanced purely inhibitory networks of pulse-coupled leaky integrate and fire neurons earlier and termed flux tubes [30]. Following Ref. [30], we find the critical perturbation strength ε_{ft} that is sufficient for an exponential decorrelation of trajectories by fitting the probability that a perturbation of strength ε causes an exponential state separation to the function

$$P_s(\varepsilon) = 1 - \exp(-\varepsilon/\varepsilon_{\text{ft}}) \quad (82)$$

ε_{ft} is the average radius of a basin of attraction, called flux tube radius. We found that this flux tube radius strongly depends on the spike onset rapidness r . For values of r only slightly larger than the critical rapidness r_{crit} , the flux

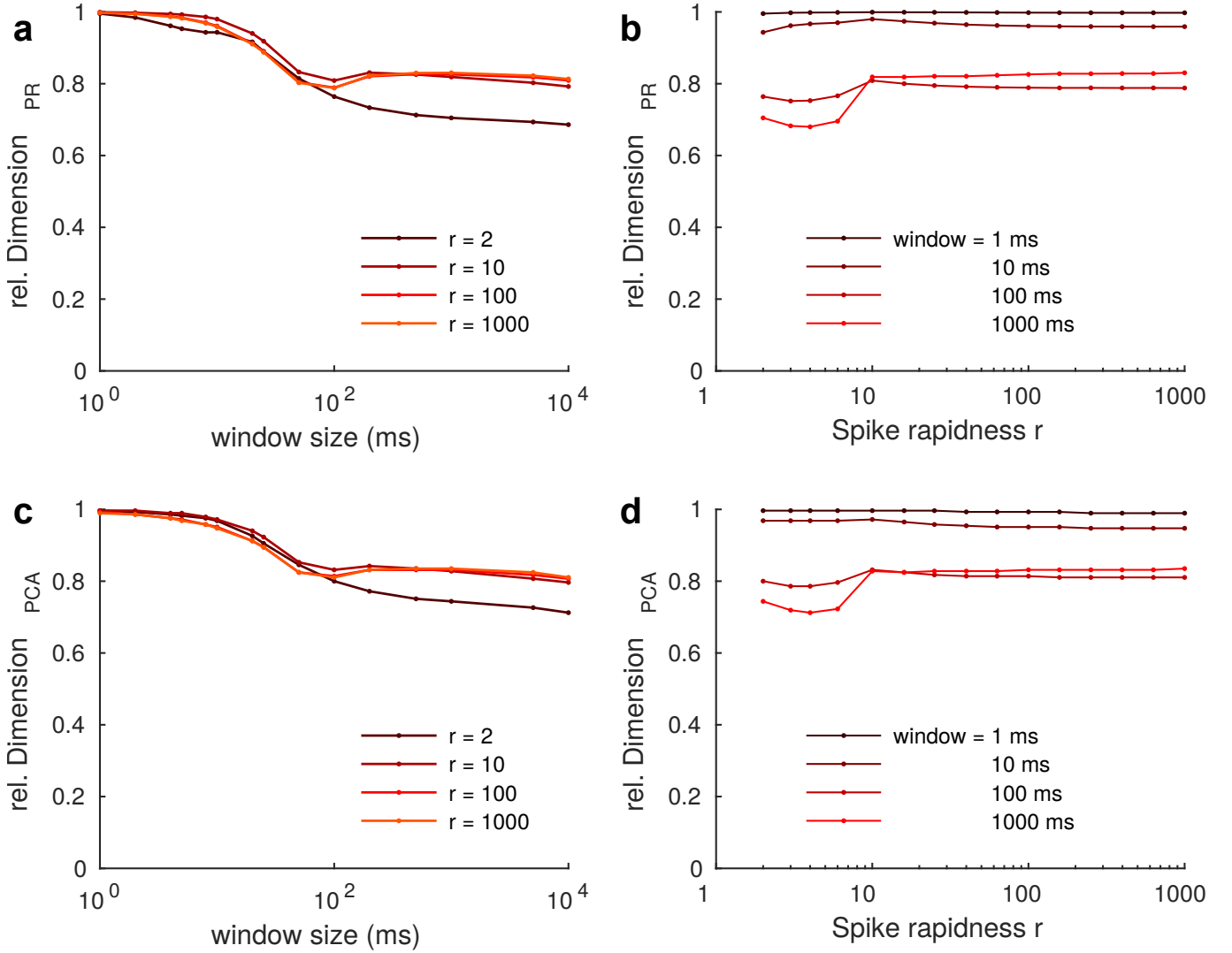


Figure 36. **Correlation based dimensionality estimates of dynamics based on pairwise correlations indicates weakly structured correlations:** **a)** relative dimension based on participation ratio (Eq. 81) vs. window size T_{win} . **b)** same as **a)** as a function of spike rapidness r . **c)+d)** same as **a)+b)** for relative dimension based on PCA. (parameters as in **Fig. 3**)

tube radius is small, but large r yield larger basins of attraction. This is depicted in **Fig. 34**.

We perturbed initial conditions along two random N -dimensional vectors orthogonal to the flow of the dynamics \vec{I} . These two vectors span a two-dimensional cross section of the N -dimensional phase space. Each pixel is a different initial condition for a simulation. Neighboring initial conditions that converge to the same trajectory are assigned same colors. For increasing values of r , the flux tubes radius increases and the boundaries become straighter. In the limit of very large r , the flux tubes are similar to those in the leaky integrate and fire model (compare to **Fig. 7** in [30]). Overall, flux tube radii get smaller with increasing network size N , number of synapses per neuron K , mean firing rate $\bar{\nu}$ and decreasing spike rapidness r . At the critical rapidness r_{crit} the flux tubes vanish.

XIX. POINCARÉ MAPS OF CHAOTIC NETWORKS

A Poincaré map is the intersection of the trajectory of a N degree of freedom dynamical system with a $N - 1$ dimensional subspace called the Poincaré surface or section.

Increasing the spike rapidness leads to a thinning of stable phase space regions (**Fig. 40**). Beyond the critical spike rapidness, the network settles after a transient period into a periodic orbit. Therefore, there is only a finite number of unique points in the Poincaré section. For increasing network size, the Poincaré sections did not capture the exotic

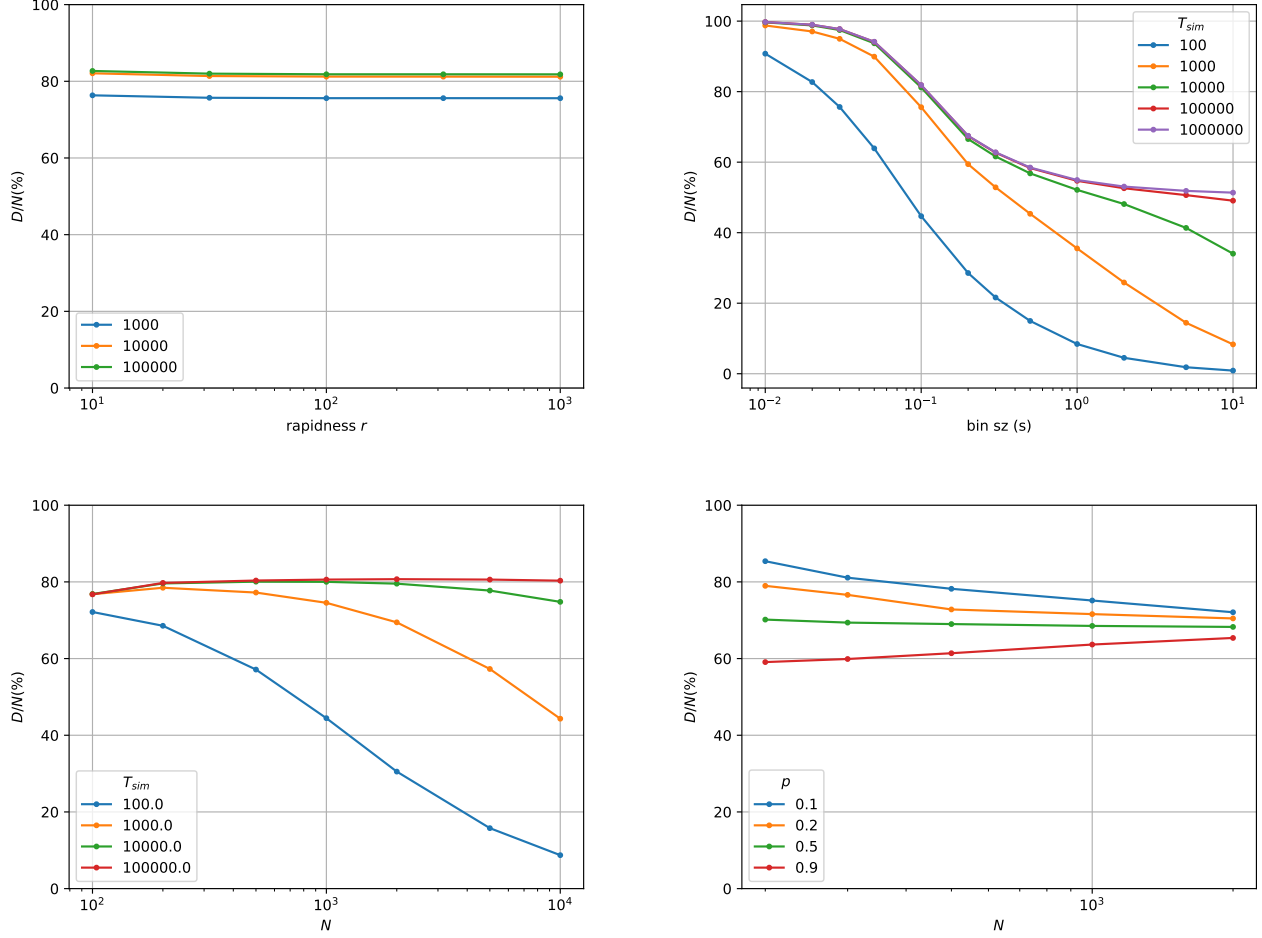


Figure 37. **Correlation based dimensionality estimates of dynamics based on pairwise correlations indicates weakly structured correlations (Fixed indegree):** **Top right)** relative dimension based on participation ratio (Eq. 81) rapidness for fixed synaptic indegree K . PCA-dimension (participation ratio) is largely independent of rapidness for inhibitory balanced rapid theta networks. Colors are different simulation time T_{sim} . **top right)** same as **a** as a function of window bin size (in s) for fixed indegree. Colors are different simulation time T_{sim} . **bottom left)** PCA-dimension (participation ratio) for varying network size N with fixed synaptic indegree K . Colors are different simulation time T_{sim} . **bottom right)** PCA-dimension (participation ratio) for varying network size N with fixed connection probability $p = K/N$. Colors are different simulation time p , simulation time is $T = 10^5 s$ and $r = 1000$. (Other parameters if not mentioned: $K = 30$, $\nu = 1 Hz$, $J_0 = 1$, $r = 1000$, bin size = 100ms)

structure of the phase space. This stresses again that the attractor is a high-dimensional object, which is hard to visualize in two dimensions.

XX. LOCAL LYAPUNOV EXPONENTS REVEAL STABLE AND UNSTABLE PHASE SPACE REGIONS

In the three-dimensional network, the local Lyapunov exponents (LLEs) can visualize further structural properties of the strange chaotic attractor. In **Fig. 43a**, colors indicate the first local Lyapunov exponent, when neuron 1 spikes, plotted at the location of phases of neuron 2 and 3 for rapidness $r = 1$. Red colors indicate a positive LLE, blue colors indicate a negative LLE. The fine structure of the first LLE is similar to the density (**Fig. 40**), while the third LLE has a fine structure which dissimilar to the density. A possible explanation is that the first LLE is smooth along the unstable manifolds, while the third LLE is smooth along the stable manifolds. The spatial distribution of the LLEs on the Poincaré surface is determined by the topology in combination with the single neuron properties. In the

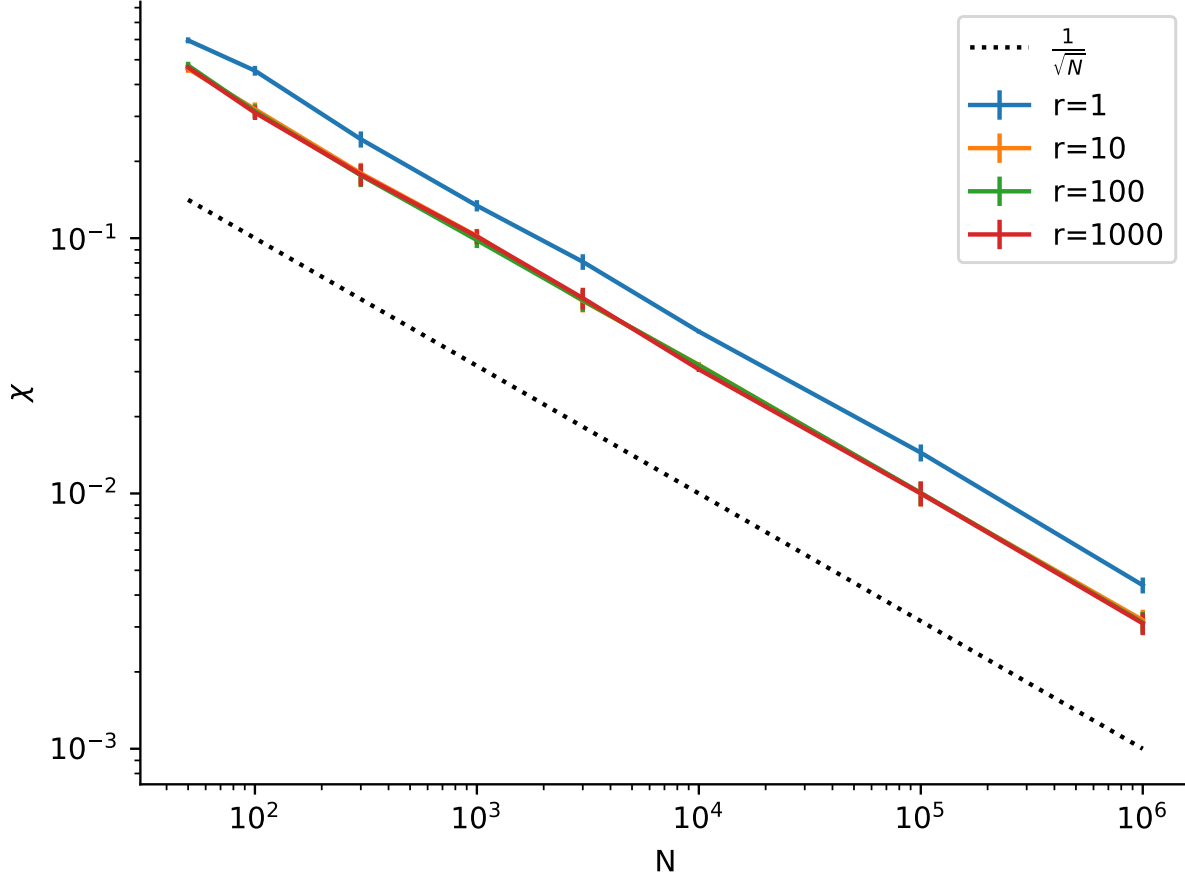


Figure 38. **Asynchronous network dynamics in balanced rapid theta networks**

Network synchrony measure χ as a function of number of neurons N for different values of rapidness r . We find asynchronous network dynamics indicated by $\chi \propto \frac{1}{\sqrt{N}}$ for various values of r .

displayed network, neuron 1 is only connected to neuron 2, therefore the LLEs mainly reflect the derivative of the phase response curve evaluated at the respective value of neuron 2. This can also be observed at a higher rapidness (rapidness $r = 1$ **Fig. 44**).

XXI. CHAOS AND DYNAMICAL ENTROPY RATE IN STRUCTURED NETWORK TOPOLOGIES

Figure 4 a-e of main paper: To test whether spike onset also exerts a strong influence on the phase space structure in more realistic network topologies, we used a previously established multilayered model of a cortical column with 77169 neurons and around 285 million synapses [7]. Numbers of neurons per population and inter-layer wiring probabilities were taken from a numerical model of a cortical column based on anatomically measured synapse counts and connection probabilities between different cortical layers [7]. The cortical column model consists of four layers (layers 2/3, 4, 5 and 6) each with an excitatory and an inhibitory population. The number of neurons in each layer and the connection probability between layers are stated in Table 1. According to these numbers, the connectivity for each population and each projection between the populations is generated as a directed sparse Erdős-Rényi random graph (Table I). We calculated also for this large network the Lyapunov spectrum making use of a parallelized implementation of the semi-analytic calculation described in section X. The sparseness of the connectivity was utilized for the efficient storage of the coupling matrices, the updates of the postsynaptic neurons and the matrix multiplications of the orthonormal system with the sparse single spike Jacobians implemented in

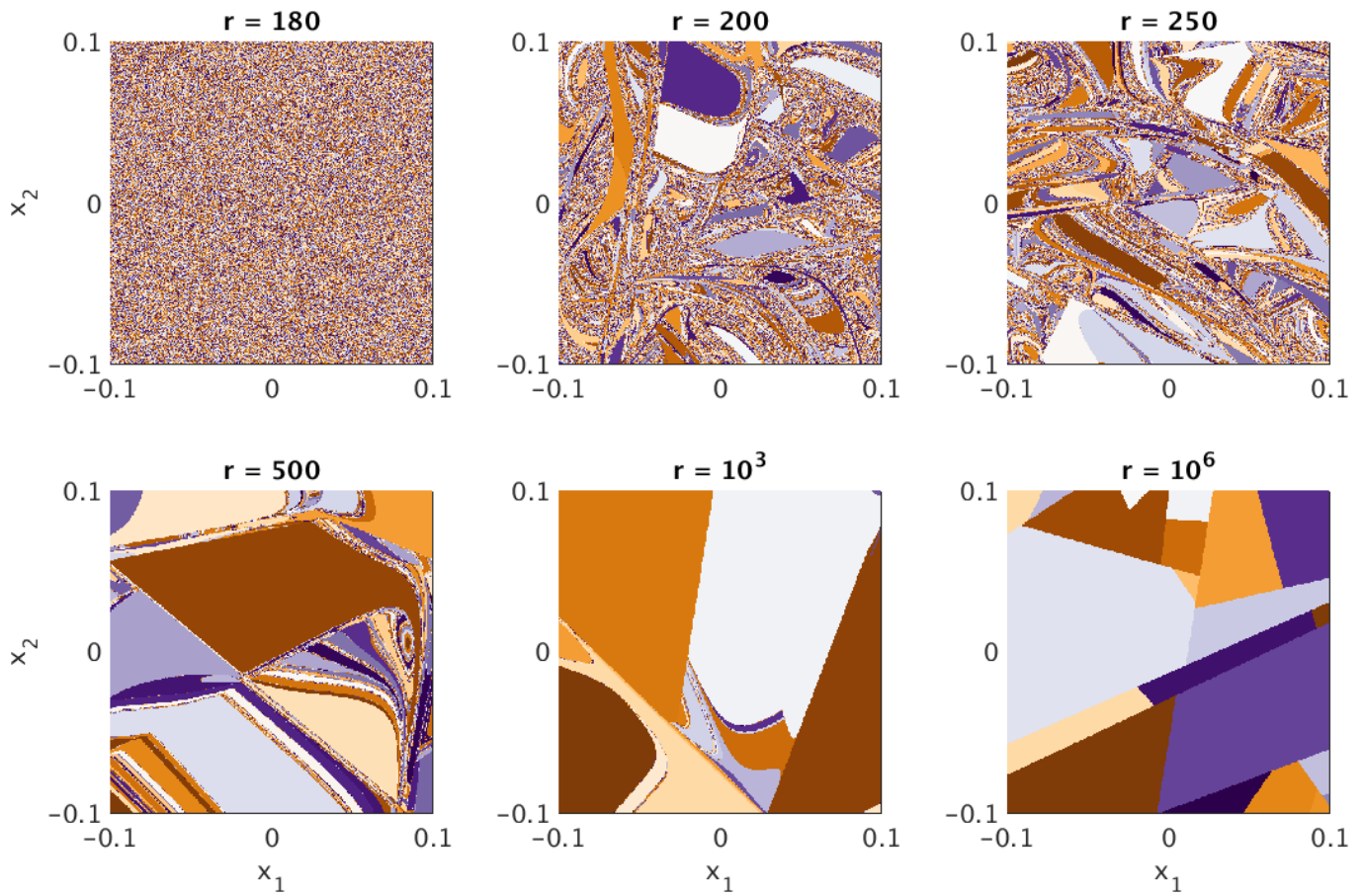


Figure 39. **Random cross section through N-dimensional phase space for different values of spike onset rapidness r :** Phase space cross sections spanned by two random N-dimensional vectors x_1 and x_2 orthogonal to the trajectory $\vec{1}$ and to each other. Initial conditions that converge to the same trajectory are drawn in the same color (parameters: $\bar{\nu} = 10$ Hz, $J_0 = 1$, $\tau_m = 10$ ms, $N = 200$, $K = 100$).

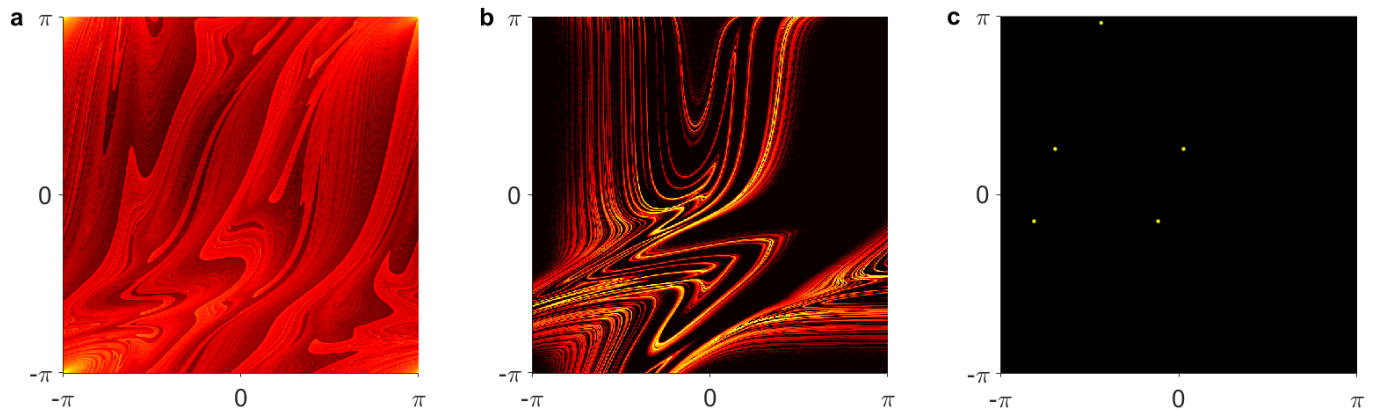


Figure 40. **Poincaré sections through phase space reveal reorganization of chaotic strange attractor by AP onset rapidness r in small networks $N = 3$:** **a)** Poincaré section of the phases of neuron 2 and 3 whenever neuron 1 spikes for low rapidness ($r = 1$). The relative density of points is represented using a heat map, where hot colors indicate high densities. **b)** Same as **a** for $r = 4$. **c)** Same as **a** for $r = 25$ (parameters: $\bar{\nu} = 14.5$ Hz, $J_0 = 1$, $\tau_m = 10$ ms, $N = 3$, $K = 1$, $r = 1, 4, 25$).

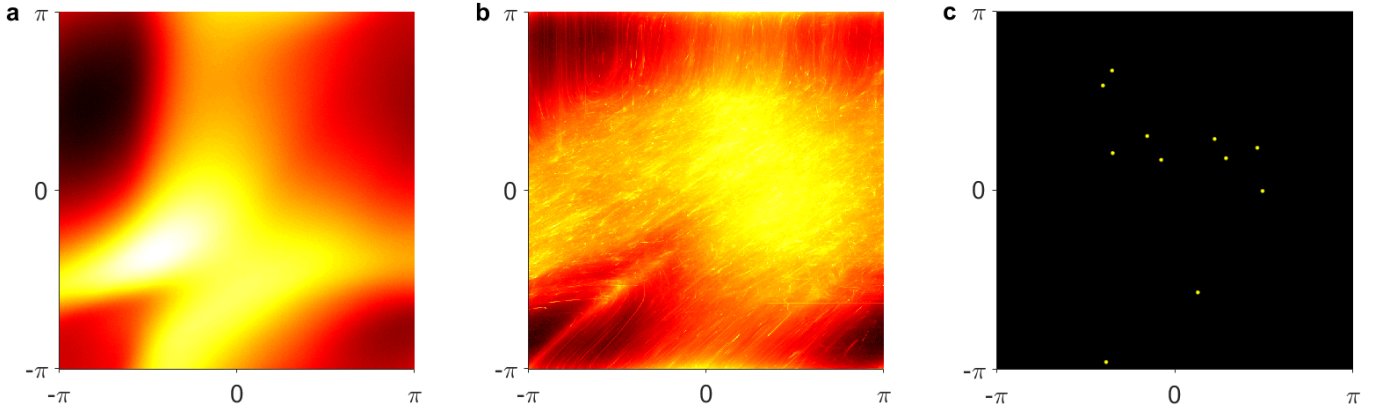


Figure 41. **Two-dimensional sections through phase space for different values of spike onset rapidness r for $N = 20$:** Surface of the phases of neuron 2 and 3 whenever neuron 1 spikes for low rapidness ($r = 1$). The relative density of points is represented using a heat map, where hot colors indicate high densities. **b)** Same as **a** for $r = 10$. **c)** Same as **a** for $r = 25$ (parameters: $\bar{\nu} = 14.5$ Hz, $J_0 = 1$, $\tau_m = 10$ ms, $N = 3$, $K = 1$, $r = 1, 10, 25$).

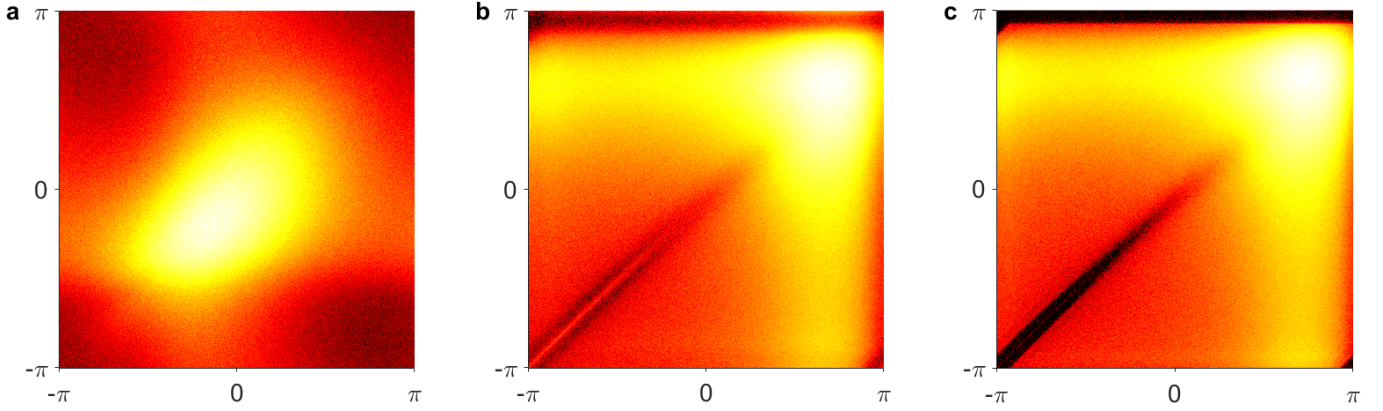


Figure 42. **Two-dimensional sections through phase space for different values of spike onset rapidness r for $N = 200$:** Surface of the phases of neuron 2 and 3 whenever neuron 1 spikes for low rapidness ($r = 1$). The relative density of points is represented using a heat map, where hot colors indicate high densities. **b)** Same as **a** for $r = 25$. **c)** Same as **a** for $r = 250$ (parameters: $\bar{\nu} = 14.5$ Hz, $J_0 = 1$, $\tau_m = 10$ ms, $N = 3$, $K = 1$, $r = 1, 25, 250$).

custom code written in Julia and C++ making use of the Automatically Tuned Linear Algebra Software (ATLAS) for matrix multiplications in the Gram–Schmidt procedure and the Message Passing Interface (MPI) for the parallel implementation of the simulations. For the reorthonormalization, we chose a parallel recursive blocked version of the Gram–Schmidt procedure [5]. Constant external input currents were adapted to obtain a desired global firing rate, for a fair comparison across different values of AP onset rapidness r . The convergence of the Lyapunov spectrum across different initial conditions is shown in **Fig. 45**. The shaded lines correspond to different initial conditions, dashed lines indicate standard error of the mean. Even for such large networks, the numerically precise event-based implementation fully converges. The neutral Lyapunov exponent converges to zero across multiple orders of magnitude (**Fig. 45b**). The dynamical entropy rate per spike of the multilayered network is considerably smaller than in random networks. A reason for that might be the occurrence of very high firing rate in some neurons with low firing rates in other neurons, possibly because the balance inequality (Eq. 68) is not satisfied. The dynamical entropy rate per spike is known to decrease for high firing rates (See **Fig. 26**).

Figure 4 f, g of main paper: We also studied the dynamics of networks with a structured microscopic architecture to corroborate our main results. We used second order networks (SONETS), which are random networks where two synapse motifs and connection probabilities are varied, while keeping higher order structures random [9]. This is achieved by using dichotomized Gaussian random variables with a desired covariance structure to generate the topology [10]. In an Erdős–Rényi graph only the connection probability $p = K/(N - 1) = P(A_{ij} = 1)$ is fixed, hence for any two synapses, the joint probability of being connected is $P(A_{ij} = 1, A_{kl} = 1) = p^2$. In SONETS, also the joint

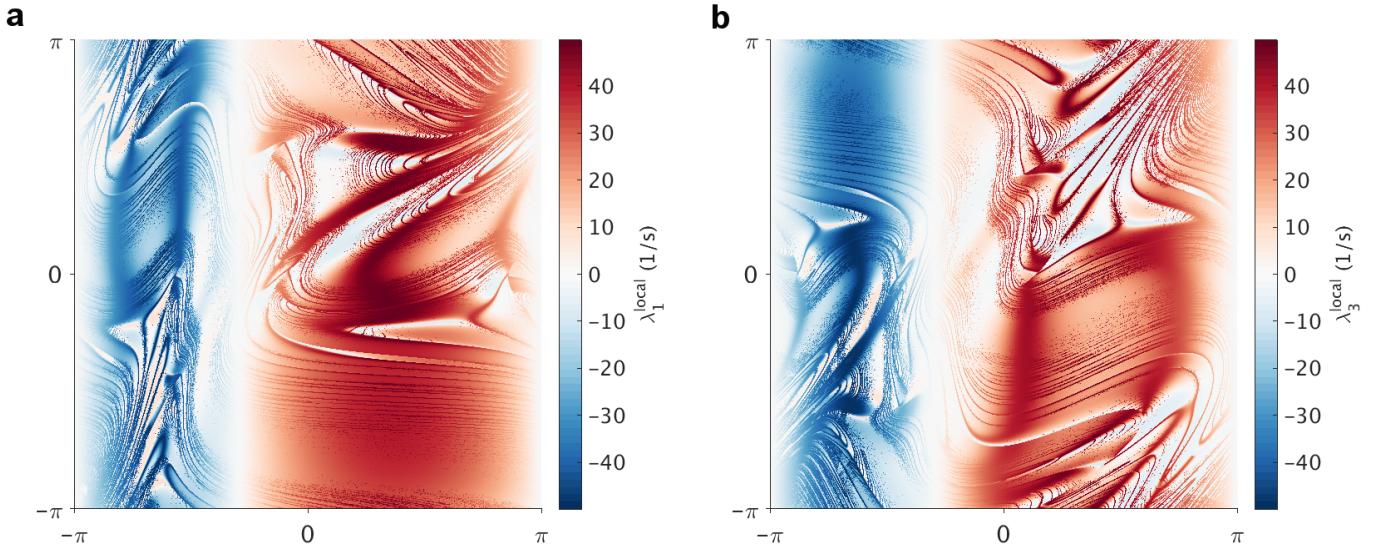


Figure 43. **Local Lyapunov exponent reveal stable and unstable phase space regions of chaotic attractor in small networks $N = 3, r = 1$:** **a)** Poincaré section of the phases of neuron 2 and 3 whenever neuron 1 spikes. The first local Lyapunov exponents (LLE) at each point is color-coded, red colors indicate local instability, blue indicates local stability. **b)** Same as **a)** for third LLE. The second LLE is trivially zero (neutral direction, not shown). The associated density of states is depicted in **Fig. 40a** (parameters: $\bar{\nu} = 14.5$ Hz, $J_0 = 1$, $\tau_m = 10$ ms, $K = 1$, $r = 1$).

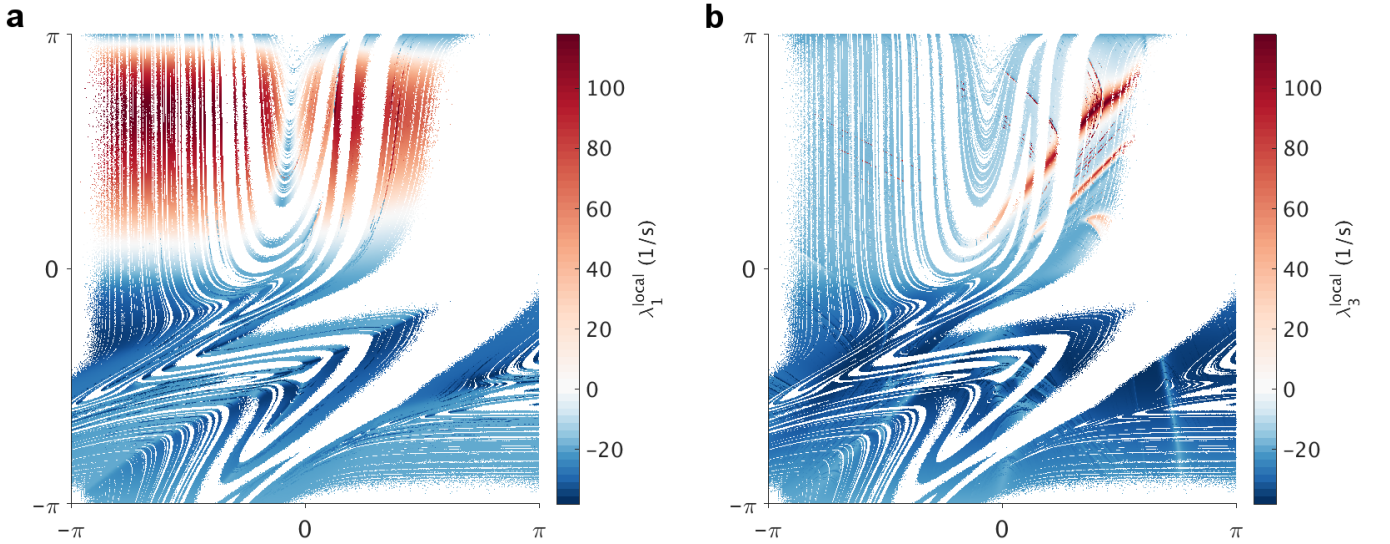


Figure 44. **Local Lyapunov exponent reveal stable and unstable phase space regions of chaotic attractor in small networks $N = 3, r = 4$:** **a)** Poincaré section of the phases of neuron 2 and 3 whenever neuron 1 spikes. The first local Lyapunov exponents (LLE) at each point is color-coded, red colors indicate local instability, blue indicates local stability. **b)** Same as **a)** for third LLE. The second LLE is trivially zero (neutral direction, not shown). The associated density of states is depicted in **Fig. 40b** (parameters: $\bar{\nu} = 14.5$ Hz, $J_0 = 1$, $\tau_m = 10$ ms, $N = 3$, $K = 1$, $r = 4$).

probability of two connections $P(A_{ij} = 1, A_{kl} = 1) = p^2(1 + \alpha_x)$ is fixed, where α_x is the respective motif frequency $\alpha_x = \{\alpha_{\text{reciprocal}}, \alpha_{\text{converging}}, \alpha_{\text{diverging}}, \alpha_{\text{chain}}\}$. $\alpha_{\text{converging}}$ is proportional to the variance of the indegree K_{in} , $\alpha_{\text{diverging}}$ is proportional to the variance of the outdegree K_{out} and α_{chain} is proportional to the covariance of the indegree K_{in} and the outdegree K_{out} . Using this approach, we interpolated excitatory-excitatory connectivity from a random graph to a graph with the second order motif structure found experimentally in superficial cortical layers [8]. Again we fixed the average network firing rate by adapting the external current I_{ext} . We used excitatory-inhibitory networks with $N_I = 2000$, $N_E = 8000$, $\eta = 0.9$, $\varepsilon = 0.3$. The excitatory-excitatory adjacency matrix was interpolated between a directed Erdős-Rényi graph and a SNET with the experimentally found motif structure. While varying second

Probability	from									
	L2/3e	L2/3i	L4e	L4i	L5e	L5i	L6e	L6i		
to	L2/3e	0.101	0.169	0.044	0.082	0.032	0	0.008	0	
	L2/3i	0.135	0.137	0.032	0.052	0.075	0	0.004	0	
	L4e	0.008	0.006	0.050	0.135	0.007	0.0003	0.045	0	
	L4i	0.069	0.003	0.079	0.160	0.003	0	0.106	0	
	L5e	0.10	0.062	0.051	0.006	0.083	0.373	0.020	0	
	L5i	0.055	0.027	0.026	0.002	0.060	0.316	0.009	0	
	L6e	0.016	0.007	0.021	0.017	0.057	0.020	0.040	0.225	
	L6i	0.036	0.001	0.003	0.001	0.028	0.008	0.066	0.144	

	number of neurons	external input
L2/3e	20683	3.6923
L2/3i	5834	12.272
L4e	21915	4.5737 94.0675
L4i	5479	16.5517 106.0455
L5e	4850	19.6825
L5i	1065	85.1521
L6e	14395	9.6156 99.1084
L6i	2948	34.0002 123.491

Table I. Wiring probabilities and number of neurons per population in cortical column model.

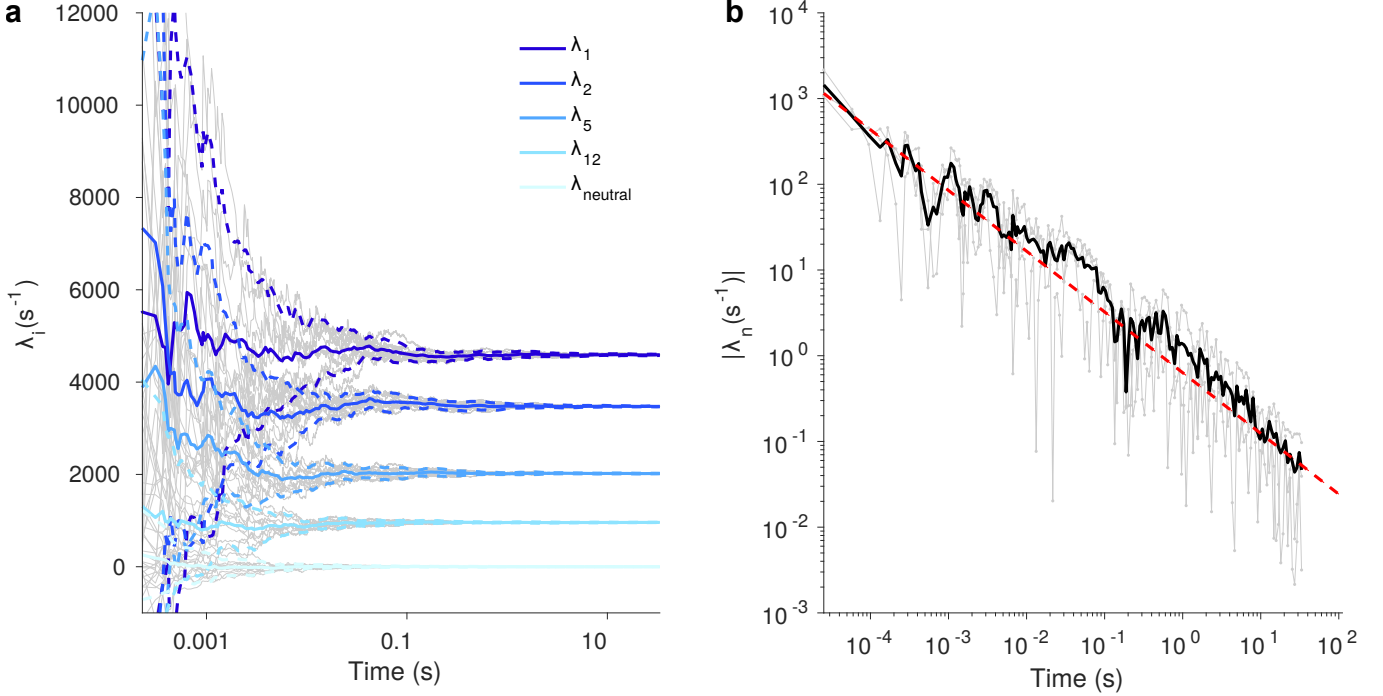


Figure 45. **Lyapunov exponents for cortical column model convergence over orders of magnitude:** **a)** gray lines: some Lyapunov exponents for ten different initial conditions, solid color lines: averages, dotted color lines: averages \pm double standard errors. $r = 10$, where the largest Lyapunov exponent is maximal. **b)** Convergence of the neutral Lyapunov exponent. Grey lines: absolute value of neutral Lyapunov exponent for three initial conditions, black line: average of absolute values of neutral Lyapunov exponents across initial conditions, red line: power law fit using the Levenberg-Marquardt algorithm with exponent -0.7 .

order motifs can generally change the largest Lyapunov exponent, dynamical entropy and the attractor dimensionality by a factor of ≈ 3 , we demonstrate that the importance of action potential onset rapidness prevails.

XXII. EXPERIMENTALLY MEASURED ACTION POTENTIAL (AP) ONSET RAPIDNESS IN CORTICAL CIRCUITS

Action potential initiation is an important bottleneck for cortical information transmission. Only the information a neuron encodes in its spike train can be used by its local network, by subsequent processing stages and, ultimately, to guide behavior. Experimental studies estimated that the spiking output of a cortical neuron contains twenty- to one hundred fold less information about the synaptic input than its membrane potential [42]. This might not come as a surprise because the membrane potential carries more information about the dense stream of incoming postsynaptic potentials than the temporally sparse sequence of outgoing action potentials. However, the finding highlights the

gatekeeping function of the action potential generation mechanism for the information transmission: it decides which aspects of the membrane potential are reflected in the outgoing spike train.

In this paragraph, we want to relate the rapidness in the idealized mathematically tractable rapid theta model with realistic values of spike onset rapidness based on effective neurons models fitted to experimental data.

Experimental findings revealed a surprisingly broad encoding bandwidth of cortical neurons: high-frequency input components of a stimulus immersed in noise are reliably encoded in the outgoing spike trains up to frequencies of several hundred Hertz. This has been first reported in acute slice preparations of regular-spiking layer 5 pyramidal cells of the rat somatosensory cortex for mean-modulated fluctuations [43] and was also later found for variance-modulated fluctuations later [44]. Independent studies confirmed the broad bandwidth using a protocol with weaker stimulation strength both in the time and frequency domain [45–48].

Theoretical predictions Theoretical studies predict that a rapid spike onset is necessary for the ultra-fast response in a feedforward architecture. Ensembles of neurons with instantaneous spike onset, such as leaky integrate-and-fire neurons [21], can transmit signals in the variance channel unattenuated for arbitrarily high frequencies [22, 49]. For the mean-modulation channel, however, the output amplitude declines $\propto \frac{1}{\sqrt{f}}$ [49]. More generally, high spike onset rapidness increases the population encoding bandwidth. This relationship between broad encoding bandwidth and high action potential (AP) onset rapidness was first directly demonstrated in the exponential integrate-and-fire model, whose AP onset rapidness is changeable [16]. A strong influence of spike onset on high-frequency encoding was also predicted by Naundorf and colleagues [18, 19]. Wei and Wolf confirmed this analytically using a mathematically tractable piecewise linear neuron model, which allows an analytical calculation of the frequency response for different AP onset rapidness [20]. In numerical simulations of multi-compartment conductance-based models, which reproduce the initiation of spikes in the axon initial segment, fast AP onset at the initiation site was necessary for encoding high frequencies [48].

Experimental confirmations These theoretical predictions on the importance of rapid AP onset for high-frequency encoding were confirmed in several experiments. In a recent study, different ways of decreasing the AP onset rapidness all impaired the ability to encode high-frequency stimulus components into the spike train [48]. In this experiment, the AP onset rapidness was decreased in slices of rat visual cortex first by decreasing extracellular sodium concentration by partially substituting NaCl by choline chloride in the extracellular solution. Secondly, the effective density of voltage-gated sodium channels (Na_V) was reduced by blocking voltage-gated sodium channels using small concentrations of tetrodotoxin (TTX) locally at the site of the axon initial segment (AIS). Both manipulations had the effect of impairing the high-frequency encoding. A similar impaired high-frequency encoding was observed in neurons from juvenile animals (P9 - P13), which naturally have a slower AP onset [48]. However, the underlying mechanism of the rapid spike onset is still a largely open question of interest for both biophysical modeling and electrophysiological experiments.

Experimentally measured AP onset rapidness While it is experimentally challenging to measure the transmembrane potential at the axon initial segment, somatic measurements of the membrane potential are routinely performed. Mathematical neuron models of different complexity have been fitted to the membrane potential for a time-varying input stimulus. A univariate integrate-and-fire type model, that has been fitted to experimental data with surprisingly accurate results is the exponential integrate-and-fire neuron [16].

$$\frac{dV}{dt} = \frac{1}{\tau_m} \left(E - V + \Delta_T \exp \left(\frac{V - V_T}{\Delta_T} \right) \right), \quad (83)$$

Δ_T is a parameter to vary the instability at the spike onset which is called spike slope factor. Small Δ_T corresponds to large values of spike onset rapidness.

Various experiments fitted recorded voltage traces based on time-varying injected currents [50–56] (see table II). We used two methods to convert the experimentally measured values of spike onset rapidness of these fitted exponential integrate-and-fire models into spike onset rapidness of the rapid theta model. In the first method, EIF and rapid theta model have the same slope $\frac{d\dot{V}}{dV}$ at the unstable fixed point (in case of no external input). In order to do so, we calculated the slope of the $\dot{V} - V$ -curve of the fitted EIF neuron for $\dot{V} = 0$ and converted to dimensionless variables by multiplying by τ_m :

$$r_{\dot{V}=0} = \frac{d\dot{V}}{dV}(\dot{V} = 0) \cdot \tau_m$$

In the second method, the EIF model and rapid theta model have the same curvature at the vertex, where \dot{V} takes

ΔT (mV)	$V_T - E$ (mV)	r_{V_G}	$r_{\dot{V}=0}$	neurons	species	cell type/location	Reference
1.2 ± 0.4	12.6	10.5	12.1	$n = 14$	mouse	layer 5 pyramidal neurons (pn)	[50]
1.34 ± 0.550	29.8	22.2	24.5	$n = 31$	male Wistar rats	layer 2/3 pn	[52]
1.28 ± 0.394	23.2	18.2	20.2	$n = 29$		layer 4 pn	[52]
1.35 ± 0.523	20.1	14.9	16.8	$n = 29$		slender-tufted layer 5 pn	[52]
1.16 ± 0.479	15.7	13.5	14.8	$n = 47$		thick-tufted layer 5 pn	[52]
1.00 ± 0.35	20.4	20.4	22.6	$n = 5$		male B6CBF1 mice	thick-tufted layer 5 pn
only histogram				$n = 10$	male C57Bl/6J mouse	layer 5 pn	[55]
only histogram				$n = 6$		GABAergic cortical interneurons	[51]

Table II. Experimentally measured values of action potential onset rapidness, where $r_{\dot{V}=0} = \frac{d\dot{V}}{dV}(\dot{V} = 0) \cdot \tau_m$ and $r_{V_G} = \frac{V_T - E}{\Delta T}$

its minimum value, which is in case of the rapid theta model also the glue point V_G . The value r_{V_G} is thus given by:

$$r_{V_G} = \frac{V_T - E}{\Delta T}$$

Table II gives both $r_{\dot{V}=0}$ and r_{V_G} converted from the EIF model fitted to experimental data recorded in various cell types.

These experimental findings unanimously indicate high values of spike onset rapidness obtained by both methods ($r \in [10.5, 22.6]$) - more than one order of magnitude higher than the classical theta model with $r = 1$ [2]. This is consistent with earlier reports of high spike onset rapidness [18, 19, 50, 51] and consistent with a strong voltage dependence of the escape rate in spike response models [55]. The experimentally fitted values of spike onset rapidness are inside the sparse chaos regime we found in balanced networks of rapid theta neurons (Figure 5 c and d of main paper). Our scaling analysis shows that the peak rapidness r_{peak} is independent of network size N for large networks but depends on membrane time constant, coupling strength, firing rate and the mean number of synapses per neuron. As these parameters do not vary by orders of magnitude across the cortex, we propose that many cortical circuits operate in the sparse chaos regime.

How well streams of spikes from one circuit can control spiking dynamics in the subsequent circuit limits its ability to encode information. It is presumably harder to control very chaotic networks by input spike trains. Therefore, we conjecture that high spike onset rapidness facilitates network state control and information transmission of subsequent circuits.

XXIII. MINIMAL EXAMPLE FOR JULIA

The following code for Julia (www.julialang.org) Version 1.0 demonstrates the event-based simulations by calculating the Poincaré sections displayed in **Fig. 40a**. Performant code for calculating Lyapunov spectra is available upon request.

```

using PyPlot
function poincare()
Ncalc = 10^7
A = 0 .<[0 0 0;1 0 1;0 1 0]
phi = rand(3)
pAll = Float64[]
for s = 1:Ncalc
    pMax,j = findmax(phi)
    dt = pi/2-pMax
    phi.+= dt
    p = A[:,j]
    phi[p] = atan.(tan.(phi[p]).-1)
    phi[j] = -pi/2
    j==1 && append!(pAll,phi[2:3])
end

```

number of spikes in calculation
define connectivity matrix
initialize neurons

find next spiking neuron j
calculate next spike time
evolve phases till next spike time
postsynaptic neurons
update postsynaptic neurons
reset spiking neuron to $-\pi/2$
save neuron 2 & 3 whenever neuron 1 spikes

```

plot(2pAll[1:2:end], 2pAll[2:2:end], "k", alpha=0.01); axis("off")
end

```

XXIV. SCALE INVARIANCES OF THE THETA MODEL

We note that the rapid theta in the parametrization introduced in the main text has several scale-invariances. This means, certain reparametrizations of pairs of the network parameters τ_m , J_0 and I give rise to exactly the same network dynamics with identical spike times. We now demonstrate these scale-invariances and describe their implications for the interpretation of the results. We first consider the QIF model:

$$\tau_m \frac{dV}{dt} = V^2 + I_{\text{ext}}$$

where $I_{\text{ext}} = I_0 \sqrt{K} = \tau_m \sqrt{K} J_0 \nu_w$. So

$$\tau_m \frac{dV}{dt} = V^2 + \tau_m \sqrt{K} J_0 \nu_w$$

A. Scaling J_0 and ν_w by factor $\alpha > 0$

$$\tau_m \frac{dV}{dt} = V^2 + \alpha^2 \tau_m \sqrt{K} J_0 \nu_w$$

Rescaling voltage and time using $V = \alpha \hat{V}$ and $\hat{t} = \alpha t$, with $d\hat{t} = \alpha dt$:

$$\tau_m \alpha \frac{d\hat{V}}{d\hat{t}/\alpha} = \alpha^2 \hat{V}^2 + \alpha^2 \tau_m \sqrt{K} J_0 \nu_w$$

After dividing both sides by α^2 :

$$\tau_m \frac{d\hat{V}}{d\hat{t}} = \hat{V}^2 + \tau_m \sqrt{K} J_0 \nu_w$$

Thus, we arrived at identical dynamics for \hat{V} after rescaling time. Note that when receiving input spikes, the voltage experiences a jump of $-\frac{\alpha J_0}{\sqrt{K}}$ (due to the scaling of J_0). Given the voltage rescaling $V = \alpha \hat{V}$ this corresponds to a jump of $-\frac{J_0}{\sqrt{K}}$ in the rescaled voltage \hat{V} . This scale invariance arises from the homogeneity of the QIF voltage dynamics, where all terms scale consistently under the transformations $V \rightarrow \alpha \hat{V}$ and $t \rightarrow \alpha \hat{t}$. Specifically, if $F(V) = V^2$, then rescaling V by α results in $\alpha^2 \hat{V}^2$, and the $\frac{dV}{dt}$ term also scales by α^2 after the time rescaling. Moreover, as for QIF, reset and threshold are $-\infty$ and ∞ respectively, voltage can be rescaled. This invariance generally does not hold for neuron models whose dynamics lack this homogeneity or who have a finite reset V_{re} or threshold V_{th} . In the case, of finite V_{re} or V_{th} , these also have to be rescaled accordingly to find the identical network dynamics.

B. Scaling τ_m and J_0 by a Factor $\beta > 0$

Consider scaling τ_m to $\beta \tau_m$ and J_0 to βJ_0 :

$$\beta \tau_m \frac{dV}{dt} = V^2 + \beta^2 \tau_m \sqrt{K} J_0 \nu_w$$

Rescaling voltage: $V = \beta \hat{V}$:

$$\beta^2 \tau_m \frac{d\hat{V}}{dt} = \beta^2 \hat{V}^2 + \beta^2 \tau_m \sqrt{K} J_0 \nu_w$$

Dividing by β^2 :

$$\tau_m \frac{d\hat{V}}{dt} = \hat{V}^2 + \tau_m \sqrt{K} J_0 \nu_w$$

Note that time is not rescaled.

C. Scaling τ_m and ν_w by a Factor $\gamma > 0$ and $\frac{1}{\gamma}$

Consider scaling τ_m to $\gamma \tau_m$ and ν_w to $\frac{\nu_w}{\gamma}$:

$$\gamma \tau_m \frac{dV}{dt} = V^2 + \gamma \tau_m \sqrt{K} J_0 \frac{\nu_w}{\gamma}$$

Rescaling time: $t = \gamma \hat{t}$, so $dt = \gamma d\hat{t}$:

$$\tau_m \frac{dV}{d\hat{t}} = V^2 + \tau_m \sqrt{K} J_0 \nu_w$$

Thus, the dynamics of V as a function of the rescaled time \hat{t} are identical to the original dynamics of V as a function of t .

In conclusion, we find three interrelated scale-invariances of the QIF model. The last scale-invariance is generic and also exists for other integrate-and-fire type models, as it relies on rescaling the time, related to the arbitrariness in which units time is measured (τ_m is the only timescale of the system and could be in milliseconds, seconds or hours). The other two rely on the homogeneity of the QIF dynamics.

D. Scale invariances of the rapid theta model

The same three scale invariances also hold for the rapid theta model

$$\tau_m \frac{dV}{dt} = \begin{cases} a_S (V - V_G)^2 + \tau_m \sqrt{K} J_0 \nu_w & \text{for } V \leq V_G \\ a_U (V - V_G)^2 + \tau_m \sqrt{K} J_0 \nu_w & \text{for } V > V_G. \end{cases} \quad (84)$$

Let's define center the voltage $\tilde{V} = V - V_G$. The original equation becomes:

$$\tau_m \frac{d\tilde{V}}{dt} = \begin{cases} a_S \tilde{V}^2 + \tau_m \sqrt{K} J_0 \nu_w & \text{for } \tilde{V} \leq 0 \\ a_U \tilde{V}^2 + \tau_m \sqrt{K} J_0 \nu_w & \text{for } \tilde{V} > 0. \end{cases} \quad (85)$$

We observe that the piecewise equation for \tilde{V} obeys the same homogeneity. Now considering multiplying J_0 and ν_w by a factor α :

$$\tau_m \frac{d\tilde{V}}{dt} = \begin{cases} a_S \tilde{V}^2 + \alpha^2 \tau_m \sqrt{K} J_0 \nu_w & \text{for } \tilde{V} \leq 0 \\ a_U \tilde{V}^2 + \alpha^2 \tau_m \sqrt{K} J_0 \nu_w & \text{for } \tilde{V} > 0. \end{cases} \quad (86)$$

Then rescaling voltage $\tilde{V} = \alpha\hat{V}$ and rescaling time $\hat{t} = \alpha t$, so $d\hat{t} = \alpha dt$ gives

$$\alpha^2 \tau_m \frac{d\tilde{V}}{d\hat{t}} = \begin{cases} a_S \alpha^2 \tilde{V}^2 + \alpha^2 \tau_m \sqrt{K} J_0 \nu_w & \text{for } \tilde{V} \leq 0 \\ a_U \alpha^2 \tilde{V}^2 + \alpha^2 \tau_m \sqrt{K} J_0 \nu_w & \text{for } \tilde{V} > 0. \end{cases} \quad (87)$$

which yields the initial dynamics with rescaled time. The other two scale invariances also hold for the rapid theta model. For the second invariance (scaling τ_m and J_0 by β), the derivation follows analogously to the QIF case, applied separately to both pieces of the piecewise definition, leveraging the homogeneity on both branches. Similarly, the third invariance (scaling τ_m and ν_w) holds due to the time rescaling argument, which is independent of the specific form of voltage dynamics.

* re2365@columbia.edu

- [1] van Vreeswijk, C. & Sompolinsky, H. Chaos in Neuronal Networks with Balanced Excitatory and Inhibitory Activity. *Science* **274**, 1724–1726 (1996); van Vreeswijk, C. & Sompolinsky, H. Chaotic Balanced State in a Model of Cortical Circuits. *Neural Computation* **10**, 1321–1371 (1998).
- [2] Ermentrout, G. & Kopell, N. Parabolic Bursting in an Excitable System Coupled with a Slow Oscillation. *SIAM J. Appl. Math.* **46**, 233–253 (1986); Gutkin, B. S. & Ermentrout, G. B. Dynamics of Membrane Excitability Determine Interspike Interval Variability: A Link Between Spike Generation Mechanisms and Cortical Spike Train Statistics. *Neural Computation* **10**, 1047–1065 (1998); Brumberg, J. C. & Gutkin, B. S. Cortical pyramidal cells as non-linear oscillators: Experiment and spike-generation theory. *Brain Research* **1171**, 122–137 (2007).
- [3] Tsodyks, M., Mitkov, I. & Sompolinsky, H. Pattern of synchrony in inhomogeneous networks of oscillators with pulse interactions. *Phys. Rev. Lett.* **71**, 1280–1283 (1993); Ernst, U., Pawelzik, K. & Geisel, T. Synchronization Induced by Temporal Delays in Pulse-Coupled Oscillators. *Phys. Rev. Lett.* **74**, 1570–1573 (1995).
- [4] Benettin, G., Galgani, L., Giorgilli, A. & Strelcyn, J.-M. Lyapunov characteristic exponents for smooth dynamical systems and for Hamiltonian systems - A method for computing all of them. I - Theory. II - Numerical application. *Meccanica* **15**, 9–30 (1980).
- [5] Yokozawa, T., Takahashi, D., Boku, T. & Sato, M. Efficient parallel implementation of classical Gram-Schmidt orthogonalization using matrix multiplication. in *Proceedings of Fourth International Workshop on Parallel matrix Algorithms and Applications (PMAA'06)* 37–38 (2006).
- [6] Renart, A. et al. The Asynchronous State in Cortical Circuits. *Science* **327**, 587–590 (2010).
- [7] Potjans, T. C. & Diesmann, M. The Cell-Type Specific Cortical Microcircuit: Relating Structure and Activity in a Full-Scale Spiking Network Model. *Cereb. Cortex* **24**, 785–806 (2014).
- [8] Song, S., Sjöström, P. J., Reigl, M., Nelson, S. & Chklovskii, D. B. Highly Nonrandom Features of Synaptic Connectivity in Local Cortical Circuits. *PLoS Biol* **3**, e68 (2005).
- [9] Zhao, L., II, B. B., Netoff, T. & Nykamp, D. Q. Synchronization from second order network connectivity statistics. *Front. Comput. Neurosci.* **5**, 28 (2011).
- [10] Macke, J. H., Berens, P., Ecker, A. S., Tolias, A. S. & Bethge, M. Generating Spike Trains with Specified Correlation Coefficients. *Neural Computation* **21**, 397–423 (2008).
- [11] Bernardi, D. & Lindner, B. A frequency-resolved mutual information rate and its application to neural systems. *Journal of Neurophysiology* **113**, 1342–1357 (2015).
- [12] Monteforte, M. & Wolf, F. Dynamical Entropy Production in Spiking Neuron Networks in the Balanced State. *Phys. Rev. Lett.* **105**, 268104 (2010).
- [13] Gao, P. & Ganguli, S. On simplicity and complexity in the brave new world of large-scale neuroscience. *Current Opinion in Neurobiology* **32**, 148–155 (2015).
- [14] Richardson, M. J. E. Firing-rate response of linear and nonlinear integrate-and-fire neurons to modulated current-based and conductance-based synaptic drive. *Phys. Rev. E* **76**, 021919 (2007).
- [15] Richardson, M. J. E. & Swarbrick, R. Firing-Rate Response of a Neuron Receiving Excitatory and Inhibitory Synaptic Shot Noise. *Phys. Rev. Lett.* **105**, 178102 (2010).
- [16] Fourcaud-Trocmé, N., Hansel, D., van Vreeswijk, C. & Brunel, N. How Spike Generation Mechanisms Determine the Neuronal Response to Fluctuating Inputs. *J. Neurosci.* **23**, 11628–11640 (2003).
- [17] Fourcaud-Trocmé, N. & Brunel, N. Dynamics of the Instantaneous Firing Rate in Response to Changes in Input Statistics. *J Comput Neurosci* **18**, 311–321 (2005).
- [18] Naundorf, B., Geisel, T. & Wolf, F. Action Potential Onset Dynamics and the Response Speed of Neuronal Populations. *J Comput Neurosci* **18**, 297–309 (2005).
- [19] Naundorf, B., Wolf, F. & Volgushev, M. Unique features of action potential initiation in cortical neurons. *Nature* **440**, 1060–1063 (2006).
- [20] Wei, W. & Wolf, F. Spike Onset Dynamics and Response Speed in Neuronal Populations. *Phys. Rev. Lett.* **106**, 088102 (2011).

- [21] Lapique, L. Recherches quantitatives sur l'excitation électrique des nerfs traitée comme une polarisation. *J Physiol Pathol Gen* **9**, 620–635 (1907).
- [22] Lindner, B. & Schimansky-Geier, L. Transmission of Noise Coded versus Additive Signals through a Neuronal Ensemble. *Phys. Rev. Lett.* **86**, 2934–2937 (2001).
- [23] Strong, S. P., Koberle, R., de Ruyter van Steveninck, R. R. & Bialek, W. Entropy and Information in Neural Spike Trains. *Phys. Rev. Lett.* **80**, 197–200 (1998).
- [24] Lindner, B. Superposition of many independent spike trains is generally not a Poisson process. *Phys. Rev. E* **73**, 022901 (2006).
- [25] Câteau, H. & Reyes, A. D. Relation between Single Neuron and Population Spiking Statistics and Effects on Network Activity. *Phys. Rev. Lett.* **96**, 058101 (2006).
- [26] Ricciardi, L. M. & Sacerdote, L. The Ornstein-Uhlenbeck process as a model for neuronal activity. *Biol. Cybern.* **35**, 1–9 (1979).
- [27] Lánský, P. & Lánská, V. Diffusion approximation of the neuronal model with synaptic reversal potentials. *Biol. Cybernetics* **56**, 19–26 (1987).
- [28] Bialek, W., Rieke, F., Steveninck, R. de R. van & Warland, D. Reading a neural code. *Science* **252**, 1854–1857 (1991).
- [29] Rieke, F., Warland, D., Steveninck, R. de R. van & Bialek, W. *Spikes: Exploring the Neural Code.* (A Bradford Book, 1999).
- [30] Monteforte, M. & Wolf, F. Dynamic Flux Tubes Form Reservoirs of Stability in Neuronal Circuits. *Phys. Rev. X* **2**, 041007 (2012).
- [31] Burns, B. D. & Webb, A. C. The Spontaneous Activity of Neurones in the Cat's Cerebral Cortex. *Proceedings of the Royal Society of London B: Biological Sciences* **194**, 211–223 (1976); *J. Neurosci.* **13**, 334–350 (1993), 334 (1993); Kara, P., Reinagel, P. & Reid, R. C. Low Response Variability in Simultaneously Recorded Retinal, Thalamic, and Cortical Neurons. *Neuron* **27**, 635–646 (2000).
- [32] Mainen, Z. F. & Sejnowski, T. J. Reliability of spike timing in neocortical neurons. *Science* **268**, 1503–1506 (1995).
- [33] Rosenbaum, R. & Doiron, B. Balanced Networks of Spiking Neurons with Spatially Dependent Recurrent Connections. *Phys. Rev. X* **4**, 021039 (2014).
- [34] Wolf, A., Swift, J. B., Swinney, H. L. & Vastano, J. A. Determining Lyapunov exponents from a time series. *Physica D: Nonlinear Phenomena* **16**, 285–317 (1985).
- [35] Shadlen, M. N. & Newsome, W. T. Noise, neural codes and cortical organization. *Current Opinion in Neurobiology* **4**, 569–579 (1994).
- [36] Shadlen, M. N. & Newsome, W. T. The Variable Discharge of Cortical Neurons: Implications for Connectivity, Computation, and Information Coding. *J. Neurosci.* **18**, 3870–3896 (1998).
- [37] Softky, W. R. & Koch, C. Cortical Cells Should Fire Regularly, But Do Not. *Neural Computation* **4**, 643–646 (1992).
- [38] Softky, W. R. & Koch, C. The highly irregular firing of cortical cells is inconsistent with temporal integration of random EPSPs. *J. Neurosci.* **13**, 334–350 (1993).
- [39] Cross, M. C. & Hohenberg, P. C. Pattern formation outside of equilibrium. *Rev. Mod. Phys.* **65**, 851–1112 (1993).
- [40] Wegner, F. Inverse participation ratio in $2+\epsilon$ dimensions. *Z Physik B* **36**, 209–214 (1980).
- [41] Kaneko, K. Lyapunov analysis and information flow in coupled map lattices. *Physica D: Nonlinear Phenomena* **23**, 436–447 (1986).
- [42] Polavieja, G. G. de, Harsch, A., Kleppe, I., Robinson, H. P. C. & Juusola, M. Stimulus History Reliably Shapes Action Potential Waveforms of Cortical Neurons. *J. Neurosci.* **25**, 5657–5665 (2005).
- [43] Köndgen, H. et al. The Dynamical Response Properties of Neocortical Neurons to Temporally Modulated Noisy Inputs In Vitro. *Cereb. Cortex* **18**, 2086–2097 (2008).
- [44] Boucsein, C., Tetzlaff, T., Meier, R., Aertsen, A. & Naundorf, B. Dynamical Response Properties of Neocortical Neuron Ensembles: Multiplicative versus Additive Noise. *J. Neurosci.* **29**, 1006–1010 (2009).
- [45] Silberberg, G., Bethge, M., Markram, H., Pawelzik, K. & Tsodyks, M. Dynamics of Population Rate Codes in Ensembles of Neocortical Neurons. *Journal of Neurophysiology* **91**, 704–709 (2004).
- [46] Higgs, M. H. & Spain, W. J. Conditional Bursting Enhances Resonant Firing in Neocortical Layer 2–3 Pyramidal Neurons. *J. Neurosci.* **29**, 1285–1299 (2009).
- [47] Tchumatchenko, T., Malyshev, A., Wolf, F. & Volgushev, M. Ultrafast Population Encoding by Cortical Neurons. *The Journal of Neuroscience* **31**, 12171–12179 (2011).
- [48] Ilin, V., Malyshev, A., Wolf, F. & Volgushev, M. Fast Computations in Cortical Ensembles Require Rapid Initiation of Action Potentials. *J. Neurosci.* **33**, 2281–2292 (2013).
- [49] Brunel, N. & Hakim, V. Fast Global Oscillations in Networks of Integrate-and-Fire Neurons with Low Firing Rates. *Neural Computation* **11**, 1621–1671 (1999).
- [50] Badel, L. et al. Dynamic I-V Curves Are Reliable Predictors of Naturalistic Pyramidal-Neuron Voltage Traces. *Journal of Neurophysiology* **99**, 656–666 (2008).
- [51] Badel, L. et al. Extracting non-linear integrate-and-fire models from experimental data using dynamic I–V curves. *Biol Cybern* **99**, 361 (2008).
- [52] Harrison, P. M., Badel, L., Wall, M. J. & Richardson, M. J. E. Experimentally Verified Parameter Sets for Modelling Heterogeneous Neocortical Pyramidal-Cell Populations. *PLOS Computational Biology* **11**, e1004165 (2015).
- [53] Kaufmann, T. J., Harrison, P. M., Richardson, M. J. E., Pinheiro, T. J. T. & Wall, M. J. Intracellular soluble α -synuclein oligomers reduce pyramidal cell excitability. *The Journal of Physiology* **2751–2772** (2016). doi:10.1113/JP271968@10.1111/(ISSN)1469-7793.ECRPrize

- [54] Doose, J., Doron, G., Brecht, M. & Lindner, B. Noisy Juxtacellular Stimulation In Vivo Leads to Reliable Spiking and Reveals High-Frequency Coding in Single Neurons. *J. Neurosci.* **36**, 11120–11132 (2016).
- [55] Pozzorini, C. et al. Automated High-Throughput Characterization of Single Neurons by Means of Simplified Spiking Models. *PLOS Computational Biology* **11**, e1004275 (2015).
- [56] Hertäg, L., Hass, J., Golovko, T. & Durstewitz, D. An Approximation to the Adaptive Exponential Integrate-and-Fire Neuron Model Allows Fast and Predictive Fitting to Physiological Data. *Front. Comput. Neurosci.* **6**, (2012).
- [57] Puelma Touzel, M. & Wolf, F. Statistical mechanics of spike events underlying phase space partitioning and sequence codes in large-scale models of neural circuits. *Phys. Rev. E* **99**, 052402 (2019).
- [58] Clark, D. G., Abbott, L. F. & Litwin-Kumar, A. Dimension of Activity in Random Neural Networks. *Phys. Rev. Lett.* **131**, 118401 (2023).
- [59] Hu, Y. & Sompolinsky, H. The spectrum of covariance matrices of randomly connected recurrent neuronal networks with linear dynamics. *PLOS Comput. Biol.* **18**, 1–27 (2022).
- [60] Softky, W. R. & Koch, C. The highly irregular firing of cortical cells is inconsistent with temporal integration of random EPSPs. *J. Neurosci.* **13**, 334–350 (1993).
- [61] Gütig, R. & Sompolinsky, H. The tempotron: a neuron that learns spike timing–based decisions. *Nat. Neurosci.* **9**, 420–428 (2006).
- [62] Gütig, R. Spiking neurons can discover predictive features by aggregate-label learning. *Science* **351**, aab4113 (2016).
- [63] Tsodyks, M. V. & Sejnowski, T. Rapid state switching in balanced cortical network models. *Network Comput. Neural Syst.* **6**, 111–124 (1995).
- [64] Brunel, N. Dynamics of sparsely connected networks of excitatory and inhibitory spiking neurons. *J. Comput. Neurosci.* **8**, 183–208 (2000).
- [65] Gerstner, W., Kistler, W. M., Naud, R. & Paninski, L. *Neuronal Dynamics: From Single Neurons to Networks and Models of Cognition*. Cambridge University Press, Cambridge (2014).
- [66] Mirollo, R. E. & Strogatz, S. H. Synchronization of pulse-coupled biological oscillators. *SIAM J. Appl. Math.* **50**, 1645–1662 (1990).
- [67] Tsodyks, M., Mitkov, I. & Sompolinsky, H. Pattern of synchrony in inhomogeneous networks of oscillators with pulse interactions. *Phys. Rev. Lett.* **71**, 1280–1283 (1993).
- [68] Ernst, U., Pawelzik, K. & Geisel, T. Synchronization induced by temporal delays in pulse-coupled oscillators. *Phys. Rev. Lett.* **74**, 1570–1573 (1995).
- [69] Timme, M., Wolf, F. & Geisel, T. Unstable attractors induce perpetual synchronization and desynchronization. *Chaos* **13**, 377–387 (2003).
- [70] Monteforte, M. *Chaotic Dynamics in Networks of Spiking Neurons in the Balanced State*. PhD thesis, Georg-August-University, Göttingen (2011).
- [71] Schmidt, A. Characterization of the phase space structure in driven neural networks in the balanced state. Master’s thesis, Georg-August-University, Göttingen (2016).
- [72] Festa, D. Chaos characterization of pulse-coupled neural networks in balanced state. Master’s thesis, MPI DS / Università di Pisa, Göttingen/Pisa (2011).
- [73] Puelma Touzel, M. *Cellular Dynamics and Stable Chaos in Balanced Networks*. PhD thesis, Georg-August-University Göttingen (2016).
- [74] Ermentrout, G. & Kopell, N. Parabolic bursting in an excitable system coupled with a slow oscillation. *SIAM J. Appl. Math.* **46**, 233–253 (1986).
- [75] Ermentrout, B. Type I membranes, phase resetting curves, and synchrony. *Neural Comput.* **8**, 979–1001 (1996).
- [76] Gutkin, B. S. & Ermentrout, G. B. Dynamics of membrane excitability determine interspike interval variability: A link between spike generation mechanisms and cortical spike train statistics. *Neural Comput.* **10**, 1047–1065 (1998).
- [77] Izhikevich, E. M. *Dynamical Systems in Neuroscience*. MIT Press (2007).
- [78] Hansel, D. & Mato, G. Asynchronous states and the emergence of synchrony in large networks of interacting excitatory and inhibitory neurons. *Neural Comput.* **15**, 1–56 (2003).
- [79] Latham, P. E., Richmond, B. J., Nirenberg, S. & Nelson, P. G. Intrinsic dynamics in neuronal networks. II. Experiment. *J. Neurophysiol.* **83**, 828–835 (2000).
- [80] Jahnke, S., Memmesheimer, R.-M. & Timme, M. Stable irregular dynamics in complex neural networks. *Phys. Rev. Lett.* **100**, 048102 (2008).
- [81] Jahnke, S., Memmesheimer, R.-M. & Timme, M. How chaotic is the balanced state? *Front. Comput. Neurosci.* **3**, 13 (2009).
- [82] Zillmer, R., Brunel, N. & Hansel, D. Very long transients, irregular firing, and chaotic dynamics in networks of randomly connected inhibitory integrate-and-fire neurons. *Phys. Rev. E* **79**, 031909 (2009).
- [83] Tonnelier, A., Belmabrouk, H. & Martinez, D. Event-driven simulations of nonlinear integrate-and-fire neurons. *Neural Comput.* **19**, 3226–3238 (2007).
- [84] Manz, P., Goedeke, S. & Memmesheimer, R.-M. Dynamics and computation in mixed networks containing neurons that accelerate towards spiking. *Phys. Rev. E* **100**, 042404 (2019).
- [85] Shadlen, M. N. & Newsome, W. T. Noise, neural codes and cortical organization. *Curr. Opin. Neurobiol.* **4**, 569–579 (1994).
- [86] van Vreeswijk, C. & Sompolinsky, H. Chaos in neuronal networks with balanced excitatory and inhibitory activity. *Science* **274**, 1724–1726 (1996).
- [87] Tetzlaff, T., Helias, M., Einevoll, G. T. & Diesmann, M. Decorrelation of neural-network activity by inhibitory feedback. *PLoS Comput. Biol.* **8**, e1002596 (2012).

- [88] Luccioli, S., Olmi, S., Politi, A. & Torcini, A. Collective Dynamics in Sparse Networks. *Phys. Rev. Lett.* **109**, 138103 (2012).
- [89] Kadmon, J. & Sompolinsky, H. Transition to Chaos in Random Neuronal Networks. *Phys. Rev. X* **5**, 041030 (2015).
- [90] Harish, O. & Hansel, D. Asynchronous Rate Chaos in Spiking Neuronal Circuits. *PLOS Comput. Biol.* **11**, 1–38 (2015).
- [91] Angulo-Garcia, D. & Torcini, A. Stable chaos in fluctuation-driven neural circuits. *Chaos, Solitons & Fractals* **69**, 233–245 (2014).
- [92] Engelken, R., Wolf, F. & Abbott, L. F. Lyapunov spectra of chaotic recurrent neural networks. *Phys. Rev. Res.* **5**, 043044 (2023).
- [93] Palmigiano, A., Engelken, R. & Wolf, F. Boosting of neural circuit chaos at the onset of collective oscillations. *eLife* **12**, e90378 (2023).
- [94] Dahmen, D., Recanatani, S., Jia, X., Ocker, G. K., Campagnola, L., Seeman, S., Jarsky, T., Helias, M. & Shea-Brown, E. Strong and localized recurrence controls dimensionality of neural activity across brain areas. *bioRxiv* **2020.11.02.365072**, (2023).
- [95] Richardson, M. J. E. Spike shape and synaptic-amplitude distribution interact to set the high-frequency firing-rate response of neuronal populations. *Phys. Rev. E* **98**, 042405 (2018).
- [96] Goldobin, D. S., di Volo, M. & Torcini, A. Discrete synaptic events induce global oscillations in balanced neural networks. *Phys. Rev. Lett.* **133**, 238401 (2024).
- [97] Richardson, M. J. E. Linear and nonlinear integrate-and-fire neurons driven by synaptic shot noise with reversal potentials. *Phys. Rev. E* **109**, 024407 (2024).